

A variational investigation of the $SU(N)$ Heisenberg model in antisymmetric irreducible representations

THÈSE N° 7309 (2016)

PRÉSENTÉE LE 21 OCTOBRE 2016
À LA FACULTÉ DES SCIENCES DE BASE
CHAIRE DE THÉORIE DE LA MATIÈRE CONDENSÉE
PROGRAMME DOCTORAL EN PHYSIQUE

ÉCOLE POLYTECHNIQUE FÉDÉRALE DE LAUSANNE

POUR L'OBTENTION DU GRADE DE DOCTEUR ÈS SCIENCES

PAR

Jérôme DUFOUR

acceptée sur proposition du jury:

Prof. H. M. Rønnow, président du jury
Prof. F. Mila, directeur de thèse
Prof. Ph. Lecheminant, rapporteur
Dr F. Becca, rapporteur
Prof. S. Vincenzo, rapporteur



ÉCOLE POLYTECHNIQUE
FÉDÉRALE DE LAUSANNE

Suisse
2016

I have not failed.
I've just found 10,000 ways that won't work
— Thomas A. Edison

To Joy and her furry friends...

Remerciements

Après neuf belles années à l'EPFL, dont quatre en doctorat, il est temps pour moi de clore ce chapitre de ma vie. Il m'est impossible d'exprimer correctement ma reconnaissance envers toutes les personnes qui m'ont entourées mais je souhaite néanmoins remercier explicitement les plus importantes pour moi.

Je commence par exprimer ma gratitude envers mon directeur de thèse, Frédéric, sans qui cette thèse n'aurait pas vu le jour. Un gros merci à tous mes collègues de labeur qui ont eu la bienveillance de m'aider et de me soutenir à travers mes doutes. Merci aussi à tous les gens rencontrés au détour des conférences auxquelles j'ai eu la chance de participer. Grâce à toutes ces personnes, j'ai eu l'opportunité de découvrir le monde académique dans une excellente ambiance de travail.

Hors du cadre professionnel, ma famille fut essentielle. Maman, Papa, je vous aime. Dès mon premier hiver dans une chambre non chauffée du Locle, en passant par un début de vie en camping en Valais, j'ai toujours reçu le nécessaire pour grandir. Vous m'avez offert l'amour, l'éducation et le temps pour me permettre de construire mes outils pour mener ma vie. Grand-maman, merci pour ton soutien car sans cela, mes années d'études auraient été bien plus difficiles. Grand Frère, en étant un modèle pour moi, tu m'as transmis une partie de la sagesse et de la sérénité que tu nieras certainement avoir en toi. Bisous à vous tous !

Hormis ma famille, de nombreux amis m'ont soutenus durant mes études. Notamment ceux de très longue date et meilleurs ex-colocs : Géraldine, Jacqueline et spécialement Guillaume. Grâce à vous j'ai quitté le Valais sans jamais vraiment quitter le Valais... À travers l'EPFL, j'ai aussi rencontré des personnes extraordinaires et vécu avec elles des moments fantastiques. Je fais un clin de d'œil particulier à Sascha, Clément et Sébastien. J'espère que les autres se reconnaîtront et ne seront pas jaloux. Un grand merci aussi à tous ceux présents à ma défense.

Je n'oublie pas Anika, la personne la plus importante pour moi ces dernières années. Je ne saurais te remercier assez pour ton soutien durant les moments sombres de ma thèse mais surtout sache que je t'aime aussi et surtout pour tout le reste.

Lausanne, 1 octobre 2016

Jérôme Dufour

Abstract

Motivated by recent experimental progress in the context of ultra-cold multi-colour fermionic atoms in optical lattices, this thesis investigates the properties of the antiferromagnetic $SU(N)$ Heisenberg models with fully antisymmetric irreducible representations labelled by a Young tableau with m boxes on each site of various lattices. Thanks to an intensive use of variational Monte Carlo method based on Gutzwiller projected fermionic wave functions, we aim to determine the ground state and its related properties of systems which are beyond the capabilities of other numerical methods. This typically means that we will study large lattices with many particles per site for $N > 2$.

The first part of this thesis will introduce the basic theoretical tools connected to the $SU(N)$ Heisenberg model. A very short review of group theory introducing Young tableaux, will clarify the concept of fully antisymmetric irreducible representation of the $SU(N)$ Lie algebra. Some properties of the Heisenberg model will be discussed and a mean-field solution will be given. The numerical methods used during this thesis and their limitations will also be introduced.

We will investigate the properties of 1-dimensional systems in the second part of this work. In particular, the chains have been studied for arbitrary N and m with non-abelian bosonisation leading to predictions about the nature of the ground state (gapped or critical) in most but not all cases. We have been able to verify these predictions for a representative number of cases with $N \leq 10$ and $m \leq N/2$, and we have shown that the opening of a gap is associated with a spontaneous dimerisation or trimerisation depending on the value of m and N . We have also investigated the marginal cases, where non-abelian bosonisation did not lead to any prediction. In these cases, variational Monte Carlo predicts that the ground state is critical with exponents that are consistent with conformal field theory. The other 1-dimensional system that has been studied is the ladder for which field-theory gives some predictions. For instance, the ground state of the $SU(4)$ case in the fundamental irreducible representation is believed to consist of a 4-site plaquette state for any non-zero inter-leg coupling. We have confirmed the presence of this state, even if in the weak coupling regime, the optimal variational state is gapless. The study has been extended to various N and m values providing interesting results. The last part will present the results for 2-dimensional lattices. The square lattice will first be investigated. A mean-field analysis predicts a plaquette ground state for $3 \leq N/m < 5$ and of a chiral ground state for $N/m \geq 5$. By systematically studying the $SU(3m)$ and $SU(6m)$ Heisenberg model, we determined that the mean-field solution is valid even at small m ($m > 1$ for $SU(3m)$ and $m > 2$ for $SU(6m)$). Then, for the $SU(6m)$ Heisenberg model with m particles per site on a honeycomb lattice, we make the connection between the $m = 1$ case, for which

Remerciements

the ground state has recently been shown to be in a plaquette singlet state, and the $m \rightarrow \infty$ limit, where a mean-field approach has established that the ground state has chiral order. We were able to show that this system has a clear tendency toward the chiral order as soon as $m \geq 2$. This demonstrates that the chiral phase can be stabilised for not too large values of m , opening the way to its experimental realisations in other lattices. We will finally present results for the $SU(3m)$ on the triangular lattice for which we find a plaquette state, when $m > 1$.

Keywords: *Heisenberg model, $SU(N)$ Lie algebra, Mean-field theory, Variational Monte Carlo, Particle swarm optimisation, One- and two-dimensional lattices, Chiral state, Plaquette state*

Résumé

Motivée par les récents progrès expérimentaux dans le contexte des atomes fermioniques ultra froids à multiples couleurs piégés dans des réseaux optiques, cette thèse s'intéresse aux propriétés des modèles de Heisenberg $SU(N)$ antiferromagnétiques dans des représentations irréductibles totalement antisymétriques indexées par un tableau de Young avec m boîtes sur chacun des sites de divers réseau. Grâce à une utilisation intensive d'une méthode variationnelle de Monte Carlo basée sur des fonctions d'ondes fermioniques Gutzwiller projetées, nous tentons de déterminer l'état fondamental et ses propriétés de systèmes qui sont au-delà des capacités des autres méthodes numériques. Cela signifie que nous allons étudier de grands réseaux avec plusieurs particules par site pour $N > 2$.

La première partie de cette thèse va introduire les outils théoriques élémentaires liés au modèle de Heisenberg $SU(N)$. Une brève révision de théorie des groupes introduisant les tableaux de Young, clarifiera le concept de représentation irréductible totalement antisymétrique de l'algèbre de Lie $SU(N)$. Quelques propriétés du modèle de Heisenberg vont être discutées et une solution champ moyen sera proposée. Les méthodes numériques utilisées durant cette thèse et leur limitations seront aussi présentées.

Nous allons examiner les propriétés de systèmes unidimensionnels dans la deuxième partie de ce travail. En particuliers, les chaînes ont été étudiées pour des N et m arbitraires à l'aide de bosonisation non-abélienne menant dans la majorité des cas à des prédictions sur la nature de l'état fondamental (gapé ou critique). Nous avons été en mesure de vérifier ces prédictions pour un nombre représentatif de cas ayant $N \leq 10$ et $m \leq N/2$ et nous avons montré que la présence d'un gap est associée à une dimérisation ou trimérisation spontanée en fonction de m et N . Nous avons aussi étudié les cas marginaux où la bosonisation non-abélienne ne donne aucune prédiction. Dans ces cas, le Monte Carlo variationnel prédit que l'état fondamental est critique avec des exposants qui sont en accord avec la théorie de champ conforme. L'autre système unidimensionnel qui a été étudié est l'échelle pour lequel la théorie des champs donne quelques prédictions. Par exemple, l'état fondamental du cas $SU(4)$ dans la représentation irréductible fondamentale est certainement composé d'un état plaquette à 4 sites pour toute valeur non-nulle du couplage entre chaînes. Nous avons confirmé la présence de cet état, même si, dans le régime de couplage faible, l'état variationnel optimal ne présente pas de gap. L'étude a été étendue à diverses valeurs de N et m et fournit des résultats intéressants.

La dernière partie présentera les résultats pour des réseaux bidimensionnels. Le réseau carré sera examiné en premier. Une analyse en champ moyen prédit un état plaquette pour $3 \leq$

Remerciements

$N/m < 5$ et d'un état chirale pour $N/m \geq 5$. En étudiant systématiquement le modèle de Heisenberg $SU(3m)$ et $SU(6m)$, nous avons déterminé que la solution champ moyen est valable même pour de petites valeurs de m ($m > 1$ pour $SU(3m)$ et $m > 2$ pour $SU(6m)$). Ensuite, pour le modèle de Heisenberg $SU(6m)$ avec m particules par site sur un réseau en nid d'abeille, nous faisons le lien entre le cas $m = 1$, pour lequel l'état fondamental a récemment été démontré être un état plaquette singulet, et la limite $m \rightarrow \infty$, où une approche champ moyen a établi que l'état fondamental est chirale. Nous avons été en mesure de montrer que ce système a une nette tendance vers un ordre chirale dès que $m \geq 2$. Cela montre que la phase chirale peut être stabilisée pour des valeurs de m pas trop élevées, ouvrant la voie à une réalisation expérimentale dans d'autres réseaux. Nous allons finalement présenter les résultats pour le réseau triangulaire avec $SU(3m)$ pour lequel nous trouvons un état plaquette lorsque $m > 1$.

Mots clefs : *Modèle de Heisenberg, Algèbre de Lie $SU(N)$, Théorie de champ moyen, Monte Carlo Variationnel, Optimisation par essais particuliers, Réseaux uni- et bidimensionnels, État Chiral, État Plaquette*

Contents

Remerciements	i
Abstract / Résumé	iii
Introduction	1
I Theoretical and numerical tools	5
1 The $SU(N)$ Heisenberg model	7
1.1 Basics of the $SU(N)$ Lie algebra	7
1.1.1 Symmetric or permutation group	8
1.1.2 Young tableau, Young operator	10
1.1.3 Basis states of $SU(N)$	11
1.1.4 Dimension of an irrep of $SU(N)$	12
1.2 $SU(N)$ Heisenberg model	14
1.2.1 The Hamiltonian	14
1.2.2 Mean-field Hamiltonian	16
2 Numerical Methods	23
2.1 Variational Monte Carlo	24
2.1.1 Gutzwiller projected variational wave functions	25
2.1.2 VMC with fermionic Gutzwiller projected wave function	27
2.2 Particle Swarm Optimisation	28
II One dimensional systems	35
3 Chain	37
3.1 Variational wave functions	38
3.2 Correlation function and structure factor	40
3.3 Results	40
3.3.1 $SU(N)$ with $m = 1$	40
3.3.2 $SU(N)$ with $m = N/2$	42
3.3.3 Relevant case: $SU(6)$ with $m = 2$	44

Contents

3.3.4	Marginal cases: SU(8) with $m = 2$ and SU(9) with $m = 3$	46
3.3.5	Irrelevant case: SU(10) with $m = 2$	49
3.3.6	Critical exponents	49
3.4	Chapter summary	51
4	Ladder	53
4.1	Variational wave functions	54
4.2	Correlation functions and structure factors	55
4.3	Results	56
4.3.1	$k = 2$	56
4.3.2	$k = 3$	59
4.3.3	$k = 4$	63
4.4	Chapter summary	65
III	Two dimensional systems	67
5	Square lattice	69
5.1	Mean-field approach	69
5.1.1	Chiral State	70
5.1.2	Valence Cluster State	75
5.1.3	Mean-field energies	76
5.2	Variational wave functions and PSO	76
5.3	Results	78
5.3.1	$k = 3$	78
5.3.2	$k = 6$	82
5.4	Additional results for $k = 3, 4, 5$	85
5.4.1	$k = 3$ and $k = 5$	85
5.4.2	$k = 4$	88
5.5	Chapter summary	91
6	Honeycomb lattice	93
6.1	Variational wave functions	94
6.2	Results	95
6.3	Chapter summary	99
7	Triangular lattice	101
7.1	Individual wave function analysis	101
7.1.1	Chiral wave function	102
7.1.2	Three sublattice colour-ordered wave function	103
7.1.3	Plaquette wave function	106
7.2	Chapter summary	108
	General conclusions	111

Back Matter	113
A Coherent states	115
B Complements about the VMC	117
B.1 Variational wave function expressed with determinants	117
B.2 Useful matrix formula	119
B.2.1 General Formula	119
B.2.2 Formula in practice	119
B.3 Issue with initialisation	121
C VMC and fully symmetric irreps	123
C.1 Effective model	123
C.2 Toy model	124
C.2.1 Applying perturbation theory	124
C.2.2 VMC fails	125
C.3 Additional comments	128
Bibliography	129
Curriculum Vitae	137

Introduction

One of the many motivations to study strongly interacting cold atomic gas is their ability to serve as quantum simulators. It is for instance experimentally possible to simulate solid state Hamiltonians by tuning the properties of lasers trapping ultracold atoms in optical lattices with a high degree of precision [1, 2, 3, 4]. Thanks to modern cooling methods (such as evaporative or sympathetic cooling), very low temperatures can be reached, typically a few orders below the Fermi temperature. For an ultracold dilute gas the interactions are expected to be weak when the scattering length is much smaller than the inter-atom spacing. Fortunately, the required strong interaction regime can be reached thanks to Feshbach resonance which increases the scattering length well beyond the inter-atom spacing. The ultracold gas can be loaded into optical periodic lattices created by superimposing orthogonal lasers. This enhances even further the interactions and allow fine tuning of the lattice parameters [5].

Recently, progress in cold atoms experiments has opened the door to new and exciting physics. When fermionic ultracold alkaline-earth atoms with nuclear spin I are trapped in optical lattices, the physics is governed by a generalised Hubbard model with $N = 2I + 1$ colours (or flavours) of fermionic particles [6, 7, 8, 9]:

$$\hat{H}_{\text{Hub}} = -t \sum_{i,j} \sum_{\alpha=1}^N \left(\hat{c}_{i\alpha}^\dagger \hat{c}_{j\alpha} + \text{h.c.} \right) + \frac{U}{2} \sum_i \left(\sum_{\alpha} \hat{n}_{i\alpha} \right)^2 \quad (1)$$

where $\hat{c}_{i\alpha}^\dagger$ and $\hat{c}_{i\alpha}$ are creation and annihilation fermionic operators, $\hat{n}_{i\alpha} = \hat{c}_{i\alpha}^\dagger \hat{c}_{i\alpha}$, t is the hopping integral between the sites i, j , and U is the on-site repulsion. When the average number of atoms per site m is an integer, and for large enough U/t , the system is expected to be in a Mott insulating phase [10]. Fluctuations induced by the hopping term in the manifold of states with m fermions per site start at second order in t/U , and the processes that appear at this order consist in exchanging particles between pairs of neighbouring sites, leading to the effective Hamiltonian:

$$\hat{H}_{\text{eff}} = J \sum_{i,j} \sum_{\alpha\beta} \hat{S}_i^{\alpha\beta} \hat{S}_j^{\beta\alpha} \quad (2)$$

with:

$$J = \frac{4t^2}{U} \quad \hat{S}_{\alpha\beta} = \hat{c}_{\alpha}^{\dagger} \hat{c}_{\beta} - \frac{m}{N} \delta_{\alpha\beta} \quad (3)$$

This effective model is $SU(N)$ symmetric and captures the low-energy physics of multi-colour ultracold atoms in optical lattices. For fermions, the case of m atoms per well corresponds to the fully antisymmetric irreducible representation of $SU(N)$ labelled by a Young tableau consisting of a single column with m boxes. For these systems, remarkable progress has recently been achieved on the experimental side. For instance, the $SU(N)$ symmetry has been observed in ultracold quantum gas of fermionic ^{173}Yb [11] or ^{87}Sr [12]. Another example is the realisation of 1-dimensional quantum wires of repulsive fermions with a tunable number of components [13]. Even more recently, a transition to a Mott insulating phase was directly probed in ^{173}Yb [14].

The antiferromagnetic Hamiltonian is known to exhibit various ground states depending not only on the lattice or the dimensionality but also on N , on the number of colours, and m , the number of particles per site.

Many studies have been done for the fundamental representation, where there is $m = 1$ particle per site. In one dimension, there is a Bethe ansatz solution for all values of N [15], and Quantum Monte Carlo simulations free of the minus sign problem have given access to the temperature dependence of correlation functions [16, 17]. For ladders, the ground state of $SU(4)$ is known to consist of 4-site plaquettes [18] and some general field theory results exist for $SU(2N)$ [19]. In two dimensions, a number of simple lattices have been investigated for a few values of N with a combination of semiclassical, variational and numerical approaches, leading to a number of interesting predictions at zero temperature [20, 21, 22, 23, 24]. In particular, for the honeycomb lattice various studies have found evidence of a plaquette state for $SU(3)$ [25] or $SU(6)$ [26], and of an algebraic spin liquid state for $SU(4)$ [27]. On the triangular lattice, the ground state changes from a three-sublattice ordered state [28] to a chiral one when a ring-exchange term is added to the Hamiltonian [29]. On the square lattice, studies for various $SU(N)$ have been conducted using LFWT, iPEPS or ED. While a colour ordered state is predicted for $SU(3)$ and $SU(5)$, a Néel-like state of dimers is likely for $SU(4)$, and spontaneous dimerisation seems to take place for $SU(8)$ [30, 31, 32].

In comparison, the case of higher antisymmetric irreducible representations ($m > 1$) has been little investigated. Thanks to field-theory and abelian bosonisation, general results exist for 1-dimensional systems [33, 34]. In two dimensions, some cases of self-conjugate irreducible representation have been investigated on various lattices with Quantum Monte Carlo simulations [35, 36, 37, 38, 39] and variational Monte Carlo [40]. The only general results available are based on mean-field theories [41, 42]. For instance, on the square lattice a plaquette and a chiral state are expected to appear for respectively $3 \leq N/m < 5$ and $N/m \geq 5$ [43, 44]. The eventuality to observe chiral phases is particularly interesting since the search for experimental realisations in lattice models involving only nearest-neighbour Heisenberg

interactions is still on-going.

This thesis aims at addressing the lack of predictions for the $SU(N)$ Heisenberg model in general irreducible representations. In particular, the fully antisymmetric ones are very interesting because they correspond to different experimentally achievable Mott insulating phases. Moreover, by studying large values of N and m , we might enter in the domain of validity of mean-field theories and hopefully discover systems which stabilise a chiral phase and are experimentally realisable.

Theoretical and numerical tools **Part I**

1 The $SU(N)$ Heisenberg model

This first chapter is dedicated to introduce some concepts of group theory to be able to construct basis of any irreducible representation of a $SU(N)$ Lie algebra labelled by Young tableaux with m boxes. The $SU(N)$ Heisenberg model will then be introduced and solved in the mean-field limit where N and m are sent to infinity keeping the ratio $k \equiv N/m$ fixed.

1.1 Basics of the $SU(N)$ Lie algebra

The objective of this section is to introduce the minimal tools and concepts required to understand the basics properties of the $SU(N)$ algebra. The interested reader should refer to Giorgi [45], Cornwell [46] or Hamermesh [47] for a more complete overview of group theory. An essential comment on the notation has to be made first. By abuse of notation, $SU(N)$ does not refer to the Lie group but to the Lie algebra. A Lie algebra is a vectorial space equipped with a non-associative multiplication called Lie brackets. The $SU(N)$ Lie algebra can be generated by N^2 operators O_{ij} with $i, j = 1, \dots, N$ obeying the following commutation relation:

$$\left[\hat{O}^{\alpha\beta}, \hat{O}^{\mu\nu} \right] = \delta_{\mu\beta} \hat{O}^{\alpha\nu} - \delta_{\alpha\nu} \hat{O}^{\mu\beta} \quad (1.1)$$

As the operator:

$$\hat{N} = \sum_{\alpha=1}^N \hat{O}^{\alpha\alpha} \quad (1.2)$$

commutes with all operators $\hat{O}^{\alpha\beta}$, the number of independent generators is $N^2 - 1$. We will use the physicist conventions, where the $N^2 - 1$ generators are traceless hermitian matrices noted T^a and the Lie brackets are given by $-i$ times the commutator. Given a set of structure constants f^{abc} and generators, the structure of the Lie algebra can be defined by the Lie brackets:

$$\left[T^a, T^b \right] = i f^{abc} T^c \quad (1.3)$$

Chapter 1. The $SU(N)$ Heisenberg model

The generators build a vectorial space whose dimension defines the dimension of the algebra. An irreducible representation (irrep) is such that there is no invariant subspace. In other words, a reducible representation can be written in a different basis as a direct sum of irreps.

The most common example of $SU(N)$ Lie algebra is the $SU(2)$ for which the structure constant is the Levi-Civita symbol $f^{abc} = \epsilon^{abc}$ and the generators are given by:

$$T^a = \frac{1}{2} \sigma^a \quad (1.4)$$

with σ^a are the Pauli matrices ($a = x, y, z$):

$$\sigma^x = \begin{pmatrix} 0 & 1 \\ 1 & 0 \end{pmatrix} \quad \sigma^y = \begin{pmatrix} 0 & i \\ -i & 0 \end{pmatrix} \quad \sigma^z = \begin{pmatrix} 1 & 0 \\ 0 & -1 \end{pmatrix} \quad (1.5)$$

This choice of generators corresponds to a 2-dimensional particular representation, *i.e.* the defining representation. More generally for $SU(N)$, the generators of the defining representation are $N \times N$ hermitian matrices that obey the relation (1.3). Using another set of generators defines a different representation. For instance, if the generators are given by $(T^a)_{bc} = -i f^{abc}$, the representation is called adjoint representation and has dimension $N^2 - 1$.

For the particular $SU(N)$, $SO(N)$, and $SP(N)$ Lie algebras the fundamental representation corresponds to the defining one and often the terminology “fundamental representation” actually means “defining representation”. Without entering into details, one of the root of a fundamental representation has highest weight and is irreducible. The number of fundamental representations defines the rank of the algebra.

We can also build an arbitrary irrep. To achieve this, consider the defining irrep of $SU(N)$ which acts on the N -dimensional space generated by the set of basis vectors ϕ_1, \dots, ϕ_N . Using tensor products between these basis vectors, other spaces with different dimensions can be generated. For instance:

$$\theta_{ij}^S = \phi_i \otimes \phi_j + \phi_j \otimes \phi_i \quad i, j = 1, \dots, N \text{ and } i \leq j \quad (1.6)$$

$$\theta_{ij}^A = \phi_i \otimes \phi_j - \phi_j \otimes \phi_i \quad i, j = 1, \dots, N \text{ and } i < j \quad (1.7)$$

respectively form a $N(N+1)/2$ and $N(N-1)/2$ -dimensional space and generate a symmetric and antisymmetric irreps of $SU(N)$. This construction can be generalised and simplified with a formalism introduced by Young [48, 49]. In the following, we will use this formalism to present a systematic way to build every irrep of $SU(N)$ for any $N \geq 2$.

1.1.1 Symmetric or permutation group

Let us define first the symmetric group S_m by the set of all permutations of the integers $\{1, 2, \dots, m\}$, $m \in \mathbb{N}$. The order of the group is obviously $m!$. This definition makes clear why this group is also referred to as the permutation group. Each element of the group is a

rearrangement $\{p(1), p(2), \dots, p(m)\}$ of $\{1, 2, \dots, m\}$. More explicitly, a permutation is written as:

$$\begin{pmatrix} 1 & 2 & 3 & \dots & m \\ p(1) & p(2) & p(3) & \dots & p(m) \end{pmatrix} \quad (1.8)$$

and the product of two permutations is:

$$\begin{pmatrix} 1 & \dots & m \\ p(1) & \dots & p(m) \end{pmatrix} \begin{pmatrix} 1 & \dots & m \\ p'(1) & \dots & p'(m) \end{pmatrix} = \begin{pmatrix} 1 & \dots & m \\ p'(p(1)) & \dots & p'(p(m)) \end{pmatrix} \quad (1.9)$$

The following example illustrates this product:

$$\begin{pmatrix} 1 & 2 & 3 & 4 & 5 \\ 4 & 3 & 1 & 5 & 2 \end{pmatrix} \begin{pmatrix} 1 & 2 & 3 & 4 & 5 \\ 2 & 5 & 1 & 3 & 4 \end{pmatrix} = \begin{pmatrix} 1 & 2 & 3 & 4 & 5 \\ 3 & 1 & 2 & 4 & 5 \end{pmatrix} \quad (1.10)$$

and allows us to make some important remarks. On the right hand side, we can see that the permutation leaves the two last integers unchanged, while the three first ones form a cycle. In this context, a cycle is a set of integers C for which each of its element c is such that $C = \{c, p(c), p(p(c)), p(p(p(c))), \dots\}$. In our previous example, the cycle is:

$$\{1, 2, 3\} = \{1, p(1) = 2, p(p(1)) = 3\} = \{2, p(2) = 1, p(p(2)) = 3\} = \{3, p(3) = 2, p(p(3)) = 1\} \quad (1.11)$$

By definition, the permutation (1.10) is noted $(1, 3, 2)$ and by not mentioning the integers 4 and 5, it is implied that they are left unchanged by the permutation. Thanks to this definition, an important statement can be made: all possible permutations can uniquely be expressed by a product of cycles with no common element. This means that any permutation in S_m that can be decomposed into Q cycles of orders $\lambda_1, \dots, \lambda_Q$. The cycle structure is the set of integers $\lambda = \{\lambda_1, \dots, \lambda_Q\}$ such that $\lambda_i \geq \lambda_j$, $1 \leq i < j \leq Q$ and $\sum_{q=1}^Q \lambda_q = m$. It provides a way to distinguish the different permutations in S_m .

The signature δ_R of a permutation R is defined to be $+1$, when the permutation is even and -1 , when it is odd. We can additionally define an operator P consisting in the sum over all permutations of S_m . Similarly, the operator Q is defined as the sum over all permutations of a permutation times its signature. They are given by:

$$P = \sum_R R \quad \quad Q = \sum_R \delta_R R \quad (1.12)$$

where the sum is taken over the $m!$ permutations of S_m . It is clear that the two following equalities hold for any permutation $R' \in S_m$:

$$PR' = \sum_R RR' = P \quad \Rightarrow \quad P^2 = m!P \quad (1.13)$$

$$QR' = \sum_R \delta_R RR' = \delta_{R'} Q \quad \Rightarrow \quad Q^2 = m!Q \quad (1.14)$$

1.1.2 Young tableau, Young operator

The definitions introduced for the permutation group can now be used to define Young tableaux and Young operators.

Each cycle structure λ can be graphically represented by putting λ_1 boxes in the first line, λ_2 boxes in the second and so on. For instance, a permutation belonging to the cycle structure $\lambda = \{4, 2, 1\}$ corresponds to:

$$\begin{array}{|c|c|c|c|} \hline & & & \\ \hline & & & \\ \hline & & & \\ \hline \end{array} \quad (1.15)$$

Such a graphical representation is known as a Young diagram and its structure is fixed by some simple rules. All boxes must be in contact and left justified, the number of boxes in each row must be smaller than or equal to the number of boxes in the row above.

A Young diagram with m boxes, where the integers associated to each box are sorted in a way that they are strictly increasing along lines (left to right) and columns (top to bottom), is called a standard Young tableau. The following standard Young tableau with the same shape λ is one possible example:

$$\begin{array}{|c|c|c|c|} \hline 1 & 3 & 4 & 7 \\ \hline 2 & 6 & & \\ \hline 5 & & & \\ \hline \end{array} \quad (1.16)$$

For a given standard Young tableau defined by its cycle structure $\{\lambda_1, \dots, \lambda_m\}$ and box numbering, one can construct a Young operator Y defined as the product of operators P_i associated to each row i and operators Q_j associated to each column j , see (1.12). The operator P_i is the sum of all permutations of the integers labelling the boxes of the i -th row. The Q_j operator is the same but for the columns (the numbering is unchanged). The following example best illustrates these definitions for a Young tableau with cycle structure $\lambda = \{2, 2, 1\}$:

$$\begin{array}{|c|c|} \hline 1 & 2 \\ \hline 3 & 4 \\ \hline 5 & \\ \hline \end{array} \longrightarrow \begin{aligned} Q_1 Q_2 &= (e - (1,3) - (1,5) - (3,5) + (1,3,5) + (1,5,3)) (e - (2,4)) \\ P_1 P_2 P_3 &= (e + (1,2)) (e + (3,4)) e \end{aligned} \quad (1.17)$$

The related Young operator is simply given by:

$$Y = Q_1 Q_2 P_1 P_2 P_3 \quad (1.18)$$

$$= (e - (1,3) - (1,5) - (3,5) + (1,3,5) + (1,5,3)) (e - (2,4)) (e + (1,2)) (e + (3,4)) \quad (1.19)$$

1.1.3 Basis states of $SU(N)$

Thanks to the previous sections we have all the tools needed to create a basis of states possessing the symmetries of any arbitrary irreps of $SU(N)$. A simple example will make the Young operator more transparent and allow us to construct a basis for the irrep of the $SU(3)$ Lie algebra with this Young diagram:

$$\begin{array}{|c|c|} \hline & \\ \hline & \\ \hline \end{array} \quad (1.20)$$

A possible standard Young tableau and related Young operator is:

$$\begin{array}{|c|c|} \hline 1 & 2 \\ \hline 3 & \\ \hline \end{array} \longrightarrow Y = (e - (1, 3))(e + (1, 2)) = e - (1, 3) + (1, 2) - (1, 3, 2) \quad (1.21)$$

The states of the defining representation of $SU(N)$ are indexed by $|A\rangle, |B\rangle$ and $|C\rangle$ (these states could be indexed by numbers, but we preferred letters to avoid confusion with the Young operator). We can apply the Young operator on all states build by a tensorial product of any combination of the states of the defining representation. Each of these states can be labelled by a Young tableau, for instance $|ACB\rangle$ is represented by:

$$\begin{array}{|c|c|} \hline A & C \\ \hline B & \\ \hline \end{array} \quad (1.22)$$

The ordering of the letters follows the numbering of the Young tableau (1.21). All the possible states having three different colours are:

$$\begin{array}{|c|c|} \hline A & B \\ \hline C & \\ \hline \end{array} \longrightarrow Y|ABC\rangle = |ABC\rangle - |CBA\rangle + |BAC\rangle - |CAB\rangle \quad \star \quad (1.23)$$

$$\begin{array}{|c|c|} \hline C & B \\ \hline A & \\ \hline \end{array} \longrightarrow Y|CBA\rangle = |CBA\rangle - |ABC\rangle + |BCA\rangle - |ACB\rangle \quad \bullet \quad (1.24)$$

$$\begin{array}{|c|c|} \hline B & C \\ \hline A & \\ \hline \end{array} \longrightarrow Y|BCA\rangle = |BCA\rangle - |ACB\rangle + |CBA\rangle - |ABC\rangle \quad \star \quad (1.25)$$

$$\begin{array}{|c|c|} \hline A & C \\ \hline B & \\ \hline \end{array} \longrightarrow Y|ACB\rangle = |ACB\rangle - |BCA\rangle + |CAB\rangle - |BAC\rangle \quad \bullet \quad (1.26)$$

$$\begin{array}{|c|c|} \hline C & A \\ \hline B & \\ \hline \end{array} \longrightarrow Y|CAB\rangle = |CAB\rangle - |BAC\rangle + |ACB\rangle - |BCA\rangle \quad \star \quad (1.27)$$

$$\begin{array}{|c|c|} \hline B & A \\ \hline C & \\ \hline \end{array} \longrightarrow Y|BAC\rangle = |BAC\rangle - |CAB\rangle + |ABC\rangle - |CBA\rangle \quad \bullet \quad (1.28)$$

All states related by the cyclic permutation indexed by \star or \bullet cancel among each other. Moreover the states, where the indices of the first column are exchanged, have opposite signs. Therefore the five constraints reduce the number of independent states from six to two. We

Chapter 1. The $SU(N)$ Heisenberg model

also have to consider initial states having twice the same letter in a standard Young tableau, like $|AAB\rangle$. Applying the Young operator on this state gives:

$$\begin{array}{|c|c|} \hline A & A \\ \hline B & \\ \hline \end{array} \longrightarrow Y|AAB\rangle = |AAB\rangle - |BAA\rangle + |AAB\rangle - |BAA\rangle \quad (1.29)$$

There are six such states arising from $|AAB\rangle$, $|AAC\rangle$, $|BAA\rangle$, $|BCC\rangle$, $|CCA\rangle$ and $|CCB\rangle$. This Young operator allows the creation of an 8-dimensional irrep of the $SU(N)$ Lie algebra.

If we were to consider initial states like $|ABA\rangle$, we would need to consider another Young operator based on another indexing of the Young tableau. This is due to the fact that this type of state would correspond to the non-standard Young tableau:

$$\begin{array}{|c|c|} \hline A & B \\ \hline A & \\ \hline \end{array} \quad (1.30)$$

The proper Young operator that we would need to use is:

$$\begin{array}{|c|c|} \hline 1 & 3 \\ \hline 2 & \\ \hline \end{array} \longrightarrow \tilde{Y} = (e - (1,2))(e + (1,3)) = e - (1,2) + (1,3) - (1,2,3) \quad (1.31)$$

so the state $|ABA\rangle$ remains connected to a standard Young tableau. The Young operators Y and \tilde{Y} generate different but equivalent 8-dimensional irreps of $SU(3)$ with different basis states. The fact that the Young operators are based on standard Young tableau implies that the state $|ABA\rangle$ cannot be used to construct the irrep of $SU(3)$ with the Young operator Y . This is easily justified because the columns of a Young tableau corresponds to an antisymmetrisation which cannot be performed on identical indices. The direct consequence is that it is not possible to construct an irrep of $SU(N)$ with more than N boxes in one column.

1.1.4 Dimension of an irrep of $SU(N)$

The formula called factors (F) over hook (H) allows to compute the dimension:

$$D = \frac{F}{H} \quad (1.32)$$

of any irrep from the shape of the Young diagram. To compute F , one starts by putting N in the top left box of the Young diagram, the integers entering the other boxes increase by one for every move to the right and decrease by one for every move down. The number F is then simply the product of all these numbers. To compute the hook number, we define a hook for box b . A hook is the starting point of a line going to the right and a line going down the Young diagram. If h_b is the number of boxes that are crossed by those two lines starting in b , then the hook number is given by:

$$H \equiv \prod_b h_b \quad (1.33)$$

For instance, the irrep represented by the following Young diagram:

$$\begin{array}{|c|c|c|} \hline & & \\ \hline & & \\ \hline \end{array} \quad (1.34)$$

has its numbers F and H given by:

$$\begin{array}{|c|c|c|} \hline N & N+1 & N+2 \\ \hline N-1 & N & \\ \hline \end{array} \quad F = (N+2)(N+1)N^2(N-1)$$

and:

$$\begin{array}{|c|c|c|} \hline & & \\ \hline & & \\ \hline \end{array} h_1 = 4 \quad \begin{array}{|c|c|c|} \hline & & \\ \hline & & \\ \hline \end{array} h_2 = 3 \quad \begin{array}{|c|c|c|} \hline & & \\ \hline & & \\ \hline \end{array} h_3 = 1 \quad \begin{array}{|c|c|c|} \hline & & \\ \hline & & \\ \hline \end{array} h_4 = 2 \quad \begin{array}{|c|c|c|} \hline & & \\ \hline & & \\ \hline \end{array} h_5 = 1$$

Therefore the dimension of this irrep is:

$$D = \frac{F}{H} = \frac{(N+2)(N+1)N^2(N-1)}{24} \quad (1.35)$$

Thanks to this formula, the dimension of the irrep of $SU(3)$ presented in the previous part is confirmed to be 8.

Much more could be discussed about the Young formalism, for instance, the character table or the tensorial product of irreps can directly be computed thanks to Young tableaux. Nevertheless, for the purpose of this work, there is no need to investigate further group theory or Young formalism. The interested reader is encouraged to read references [32, 50] for more information on the Young formalism directly related to the $SU(N)$ Heisenberg model that will be introduced in the next section.

1.2 $SU(N)$ Heisenberg model

As we introduced in the previous section, various different irreps of the $SU(N)$ algebra exist. In this work, we will focus only on states with fully antisymmetric irreps on each site and the discussion is now restricted to Young diagrams with m boxes of the following shapes:

$$\begin{array}{c} \square \end{array} \quad \begin{array}{c} \square \\ \square \end{array} \quad \begin{array}{c} \square \\ \square \\ \square \end{array} \quad \dots \quad \begin{array}{c} \square \\ \square \\ \square \\ \vdots \\ \square \end{array} \quad (1.36)$$

For this type of diagram, the generators can be expressed with fermionic operators \hat{c}_α^\dagger and \hat{c}_α :

$$\hat{S}^{\alpha\beta} = \hat{c}_\alpha^\dagger \hat{c}_\beta - \frac{m}{N} \delta_{\alpha\beta} \quad (1.37)$$

where m is the number of particles per site. One can easily check that these operators satisfy the commutation relations (1.1). When $\alpha \neq \beta$, the $\hat{S}^{\alpha\beta}$ are the analog of \hat{S}^\pm of the $SU(2)$ case. The three operators of $SU(2)$ can be expressed with fermionic creation and annihilation operators:

$$\hat{S}^+ = \hat{S}^{\uparrow\downarrow} = \hat{c}_\uparrow^\dagger \hat{c}_\downarrow \quad (1.38)$$

$$\hat{S}^- = \hat{S}^{\downarrow\uparrow} = \hat{c}_\downarrow^\dagger \hat{c}_\uparrow \quad (1.39)$$

$$\hat{S}^z = \frac{1}{2} (\hat{S}^{\uparrow\uparrow} - \hat{S}^{\downarrow\downarrow}) = \frac{1}{2} (\hat{c}_\uparrow^\dagger \hat{c}_\uparrow - \hat{c}_\downarrow^\dagger \hat{c}_\downarrow) \quad (1.40)$$

We can also check that the sum of $\hat{S}^{\alpha\alpha}$ gives an operator that commutes with all other: $\hat{S}^{\uparrow\uparrow} + \hat{S}^{\downarrow\downarrow} = \hat{c}_\uparrow^\dagger \hat{c}_\uparrow + \hat{c}_\downarrow^\dagger \hat{c}_\downarrow - m = 0$. For $N > 2$, the degrees of freedom are thought as N different colours (or flavours) by opposition to the $SU(2)$ spins.

1.2.1 The Hamiltonian

1.2.1.1 Definition

The $SU(N)$ Heisenberg Hamiltonian is given by:

$$\hat{H} = \sum_{i,j} \sum_{\alpha\beta} J_{ij} \hat{S}_i^{\alpha\beta} \hat{S}_j^{\beta\alpha} \quad (1.41)$$

Using the relation (1.37) the Hamiltonian becomes:

$$\sum_{\alpha\beta} \hat{S}_i^{\alpha\beta} \hat{S}_j^{\beta\alpha} = \sum_{\alpha\beta} \left(\hat{c}_{i\alpha}^\dagger \hat{c}_{i\beta} - \frac{m_i}{N} \delta_{\alpha\beta} \right) \left(\hat{c}_{j\beta}^\dagger \hat{c}_{j\alpha} - \frac{m_j}{N} \delta_{\alpha\beta} \right) \quad (1.42)$$

$$= \sum_{\alpha\beta} \hat{c}_{i\alpha}^\dagger \hat{c}_{i\beta} \hat{c}_{j\beta}^\dagger \hat{c}_{j\alpha} - \sum_{\alpha} \left(\frac{m_j}{N} \hat{c}_{i\alpha}^\dagger \hat{c}_{i\alpha} + \frac{m_i}{N} \hat{c}_{j\alpha}^\dagger \hat{c}_{j\alpha} \right) + \frac{m_i m_j}{N} \quad (1.43)$$

$$= \sum_{\alpha\beta} \hat{c}_{i\alpha}^\dagger \hat{c}_{i\beta} \hat{c}_{j\beta}^\dagger \hat{c}_{j\alpha} - \frac{m_i m_j}{N} \quad (1.44)$$

From now on, it will be assumed, if not specified otherwise, that we are interested in the antiferromagnetic Hamiltonian having $m = m_i = m_j$ particles on each site and that the interactions only occur between neighbouring sites $\langle i, j \rangle$ with constant strength, *e.g.* $J_{ij} = J > 0$. Moreover as the constant term m^2/N is discarded, we will be dealing with the following SU(N) Hamiltonian:

$$\hat{H} = J \sum_{\langle i, j \rangle} \sum_{\alpha\beta} \hat{c}_{i\alpha}^\dagger \hat{c}_{i\beta} \hat{c}_{j\beta}^\dagger \hat{c}_{j\alpha} = J \sum_{\langle i, j \rangle} \hat{H}_{ij} \quad (1.45)$$

In situations where $m = 1$, the Hamiltonian only permutes particles and is rewritten as:

$$H = J \sum_{\langle i, j \rangle} P_{ij} \quad (1.46)$$

1.2.1.2 Acting on a state

Consider the simple case, where $m = 1$ and observe how the Hamiltonian \hat{H}_{ij} acts on a state $|\mu_i \nu_j\rangle \equiv \hat{c}_{i\mu}^\dagger \hat{c}_{j\nu}^\dagger |0\rangle$ with μ, ν two of the N possible colour indexes of the fundamental representation:

$$\hat{H}_{ij} |\mu_i \nu_j\rangle = \sum_{\alpha\beta} \hat{c}_{i\alpha}^\dagger \hat{c}_{i\beta} \hat{c}_{j\beta}^\dagger \hat{c}_{j\alpha} \hat{c}_{i\mu}^\dagger \hat{c}_{j\nu}^\dagger |0\rangle \quad (1.47)$$

$$= \sum_{\alpha\beta} \hat{c}_{i\alpha}^\dagger \hat{c}_{j\beta}^\dagger \hat{c}_{i\beta} \hat{c}_{j\alpha} \hat{c}_{i\mu}^\dagger \hat{c}_{j\nu}^\dagger |0\rangle \quad (1.48)$$

$$= \sum_{\alpha\beta} \hat{c}_{i\alpha}^\dagger \hat{c}_{j\beta}^\dagger \delta_{\beta\mu} \delta_{\alpha\nu} |0\rangle \quad (1.49)$$

$$= \hat{c}_{i\nu}^\dagger \hat{c}_{j\mu}^\dagger |0\rangle \quad (1.50)$$

$$= |\nu_i \mu_j\rangle \quad (1.51)$$

We see that this simply permutes the colours μ and ν . We can now see how it acts on basis states of an irrep of SU(N). In particular, the simplest example is for the SU(2) singlet and triplet irreps. The triplets form a basis of a 3-dimensional symmetric irrep while the singlet is

Chapter 1. The $SU(N)$ Heisenberg model

the unique state of a 1-dimensional antisymmetric irrep. The Hamiltonian \hat{H}_{ij} acts as:

$$H_{ij} \frac{|\uparrow\downarrow\rangle - |\downarrow\uparrow\rangle}{\sqrt{2}} = \frac{|\downarrow\uparrow\rangle - |\uparrow\downarrow\rangle}{\sqrt{2}} = -\frac{|\uparrow\downarrow\rangle - |\downarrow\uparrow\rangle}{\sqrt{2}} \quad (1.52)$$

$$H_{ij} \frac{|\uparrow\downarrow\rangle + |\downarrow\uparrow\rangle}{\sqrt{2}} = \frac{|\downarrow\uparrow\rangle + |\uparrow\downarrow\rangle}{\sqrt{2}} \quad (1.53)$$

$$H_{ij} |\uparrow\uparrow\rangle = |\uparrow\uparrow\rangle \quad (1.54)$$

$$H_{ij} |\downarrow\downarrow\rangle = |\downarrow\downarrow\rangle \quad (1.55)$$

This means that the Hamiltonian behaves as expected, as a permutation operator with energy equal to -1 for the singlet and $+1$ for the triplet states.

More generally, as the basis states of a particular irrep are defined by applying the Young operator on a tensor product of states $|\mu\rangle$ of the fundamental irrep, the Hamiltonian can be decomposed as a sum of signed permutation with the additional constraint that the Pauli principle must be respected.

1.2.1.3 Connection between $m = l$ and $m = N - l$

A system with m particles per site can be labelled by a Young tableau with m boxes in one column. This is a completely antisymmetric representation. Due to the fermionic nature of the particles, it is clear that it is impossible to put more than N particles per site, so $m \leq N$. For any allowed m , there is a conjugate equivalent representation. A system with $m = l$ particles per site is equivalent to a system with $m = N - l$ particles per site. The simplest non-trivial example is for $N = 3$ and $l = 1$.

When $m = l = 1$, *i.e.* in the fundamental irrep, the basis states are $|A\rangle \equiv \hat{c}_A^\dagger |0\rangle$, $|B\rangle \equiv \hat{c}_B^\dagger |0\rangle$ and $|C\rangle \equiv \hat{c}_C^\dagger |0\rangle$. The action of the Hamiltonian on the sites i and j on a state like $|A_i B_j\rangle$ is $|B_i A_j\rangle$. As expected the Hamiltonian behaves as a simple permutation operator.

When $m = N - l = 2$, the basis states of the irrep are $|1\rangle \equiv Y|AB\rangle$, $|2\rangle \equiv Y|AC\rangle$ or $|3\rangle \equiv Y|BC\rangle$, where Y is the Young operator that antisymmetrises the states: $Y = (e - 1, 2)$. Note first that like when $m = 1$, the dimension is equal to three, but when $m = 2$, each pair of basis states shares one colour. After some simple computational steps, the effect of the Hamiltonian on $|1_i 2_j\rangle$ is found to be $|1_i 2_j\rangle + |2_i 1_j\rangle$. The Hamiltonian therefore acts like a sum of the identity and permutation operator. The identity arises from the exchange of the shared colour between two states. Therefore, for each link, when $m = N - l = 2$. The Hamiltonian behaves like for the case $m = l = 1$ up to an identity.

1.2.2 Mean-field Hamiltonian

To obtain the $SU(N)$ Heisenberg model in the mean-field limit, one can follow Affleck and Marston [41] and proceed to a Hubbard-Stratonovich transformation. The first step required

to apply this transformation is to write the partition function as a path integral over coherent states. This allows a replacement of the quantum operators by Grassmann variables for which the Hubbard-Stratonovich transformation is possible. Some information on Grassmann variables is given in appendix A.

1.2.2.1 Path integral over coherent states

The partition function is generally given by:

$$Z = \text{Tr} \left(\hat{T}_\tau \left(\exp \left(- \int_0^\beta \hat{H}(\tau) d\tau \right) \right) \right) \quad (1.56)$$

We will now focus on the time ordering operator \hat{T}_τ inside the trace. We can notice that it is possible to split the integral between 0 and β in N_ϵ intervals of width $\epsilon = \beta / N_\epsilon$.

$$\hat{T}_\tau \left(\exp \left(- \int_0^\beta \hat{H}(\tau) d\tau \right) \right) = \prod_{n=0}^{N_\epsilon-1} \hat{T}_n \left(\exp \left(- \int_{n\epsilon}^{(n+1)\epsilon} \hat{H}(\tau) d\tau \right) \right) \quad (1.57)$$

$$= \lim_{\epsilon \rightarrow 0} \prod_{n=0}^{N_\epsilon-1} \hat{T}_n \left(\exp \left(- \hat{H}(n\epsilon) \epsilon \right) \right) \quad (1.58)$$

$$= \lim_{\epsilon \rightarrow 0} \prod_{n=0}^{N_\epsilon-1} \hat{T}_n \left(\mathbb{1} - \hat{H}(n\epsilon) \epsilon \right) \quad (1.59)$$

The time ordering operator \hat{T}_n organises the operators such that n decreases from left to right. We can now introduce Grassmann variables by combining (A.17), (1.56) and (1.59) to get:

$$Z = \lim_{\epsilon \rightarrow 0} \prod_{n=0}^{N_\epsilon-1} \int d^2 \mathbf{z}_0 e^{-\mathbf{z}_0^* \mathbf{z}_0} \langle -\mathbf{z}_0 | \hat{T}_n \left(\mathbb{1} - \hat{H}(n\epsilon) \epsilon \right) | \mathbf{z}_0 \rangle \quad (1.60)$$

After inserting the identity (A.13) at each time slice, the previous equation becomes:

$$\begin{aligned} Z &= \lim_{\epsilon \rightarrow 0} \int d^2 \mathbf{z}_0 d^2 \mathbf{z}_1 \dots d^2 \mathbf{z}_{N_\epsilon-1} d^2 \mathbf{z}_{N_\epsilon} e^{-\mathbf{z}_0^* \mathbf{z}_0} e^{-\mathbf{z}_1^* \mathbf{z}_1} \dots e^{-\mathbf{z}_{N_\epsilon-1}^* \mathbf{z}_{N_\epsilon-1}} \times \\ &\quad \times \langle -\mathbf{z}_0 | \mathbb{1} - \hat{H}((N_\epsilon - 1)\epsilon) \epsilon | \mathbf{z}_{N_\epsilon-1} \rangle \langle \mathbf{z}_{N_\epsilon-1} | \mathbb{1} - \hat{H}((N_\epsilon - 2)\epsilon) \epsilon | \mathbf{z}_{N_\epsilon-2} \rangle \times \dots \times \\ &\quad \times \langle \mathbf{z}_1 | \mathbb{1} - \hat{H}(0) \epsilon | \mathbf{z}_0 \rangle \end{aligned} \quad (1.61)$$

$$\begin{aligned} &= \lim_{\epsilon \rightarrow 0} \int d^2 \mathbf{z}_0 d^2 \mathbf{z}_1 \dots d^2 \mathbf{z}_{N_\epsilon-1} d^2 \mathbf{z}_{N_\epsilon} e^{-\mathbf{z}_0^* \mathbf{z}_0} e^{-\mathbf{z}_1^* \mathbf{z}_1} \dots e^{-\mathbf{z}_{N_\epsilon-1}^* \mathbf{z}_{N_\epsilon-1}} \times \\ &\quad \times e^{-\mathbf{z}_0^* \mathbf{z}_{N_\epsilon-1}} (1 - \epsilon H_{0, N_\epsilon-1}) e^{\mathbf{z}_{N_\epsilon-1}^* \mathbf{z}_{N_\epsilon-2}} (1 - \epsilon H_{N_\epsilon-1, N_\epsilon-2}) \times \dots \times \\ &\quad \times e^{\mathbf{z}_1^* \mathbf{z}_0} (1 - \epsilon H_{1,0}) \end{aligned} \quad (1.62)$$

We used the expression of an operator bracketed between coherent states (A.19):

$$H_{n, n-1} e^{\mathbf{z}_n^* \mathbf{z}_{n-1}} \equiv H(\mathbf{z}_n^*, \mathbf{z}_{n-1}) e^{\mathbf{z}_n^* \mathbf{z}_{n-1}} = \langle \mathbf{z}_n | \hat{H}((n-1)\epsilon) | \mathbf{z}_{n-1} \rangle \quad (1.63)$$

Chapter 1. The $SU(N)$ Heisenberg model

It should be noticed that after this computation, the Hamiltonian is expressed with the Grassmann variables. This means that the following replacements occurs $\hat{c}_i \rightarrow z_i$ and $\hat{c}_i^\dagger \rightarrow z_i^*$. We will also set periodic boundary condition $\mathbf{z}_0 = -\mathbf{z}_{N_\epsilon}$ and make the approximation $1 - \epsilon H \approx e^{-\epsilon H}$ to get:

$$Z = \lim_{\epsilon \rightarrow 0} \int d^2 \mathbf{z}_0 d^2 \mathbf{z}_1 \dots d^2 \mathbf{z}_{N_\epsilon-1} d^2 \mathbf{z}_{N_\epsilon} e^{-\mathbf{z}_0^* \mathbf{z}_0} e^{-\mathbf{z}_1^* \mathbf{z}_1} \dots e^{-\mathbf{z}_{N_\epsilon-1}^* \mathbf{z}_{N_\epsilon-1}} \times \\ \times e^{\mathbf{z}_{N_\epsilon}^* \mathbf{z}_{N_\epsilon-1}} e^{-\epsilon H_{N_\epsilon, N_\epsilon-1}} e^{\mathbf{z}_{N_\epsilon-1}^* \mathbf{z}_{N_\epsilon-2}} e^{-\epsilon H_{N_\epsilon-1, N_\epsilon-2}} \dots e^{\mathbf{z}_1^* \mathbf{z}_0} e^{-\epsilon H_{1,0}} \quad (1.64)$$

$$= \lim_{\epsilon \rightarrow 0} \int \prod_{n=0}^{N_\epsilon} (d^2 \mathbf{z}_n) \exp \left(- \sum_{n=1}^{N_\epsilon} \mathbf{z}_n^* (\mathbf{z}_n - \mathbf{z}_{n-1}) - \epsilon \sum_{n=1}^{N_\epsilon} H_{n, n-1} \right) \quad (1.65)$$

$$= \lim_{\epsilon \rightarrow 0} \int \prod_{n=0}^{N_\epsilon} (d^2 \mathbf{z}_n) \exp \left(- \epsilon \sum_{n=1}^{N_\epsilon} \left(\mathbf{z}_n^* \frac{\mathbf{z}_n - \mathbf{z}_{n-1}}{\epsilon} + H_{n, n-1} \right) \right) \quad (1.66)$$

$$= \int \mathcal{D}^2 \mathbf{z} \exp \left(- \int_0^\beta \mathbf{z}^* \partial_\tau \mathbf{z} + H(\mathbf{z}^*, \mathbf{z}) d\tau \right) \quad (1.67)$$

To write this last equation, one has defined the measure:

$$\mathcal{D}^2 \mathbf{z} \equiv \lim_{\epsilon \rightarrow 0} \prod_{n=0}^{N_\epsilon} (d^2 \mathbf{z}_n) \quad (1.68)$$

and the limit has been taken which introduces the integral and derivative. We have found an expression that connects the partition function to an action depending on \mathbf{z} and \mathbf{z}^* :

$$Z = \int \mathcal{D}^2 \mathbf{z} \exp(-S[\mathbf{z}^*, \mathbf{z}]) \quad (1.69)$$

For cases where the action contains only terms like $G_{ij}^{-1} z_i^* z_j$, the integral can formally be computed. The matrix G^{-1} usually refers to the Green function.

1.2.2.2 Hubbard-Stratonovich transformation

This formalism can be applied to our $SU(N)$ Heisenberg Hamiltonian, where the fermions have N different flavours and live on a lattice with n sites labelled by indices i, j :

$$\hat{H} = J \sum_{\alpha, \beta} \sum_{\langle i, j \rangle} \hat{c}_{i\alpha}^\dagger \hat{c}_{i\beta} \hat{c}_{j\beta}^\dagger \hat{c}_{j\alpha} = J \sum_{\alpha, \beta} \sum_{\langle i, j \rangle} \hat{c}_{i\alpha}^\dagger \hat{c}_{j\beta}^\dagger \hat{c}_{j\alpha} \hat{c}_{i\beta} \quad (1.70)$$

The reordering of the fermionic operators is required because in the path integral formulation, the Hamiltonian has to be given in a normal ordered form to be applied on coherent states. This formulation allows us to rewrite the Hamiltonian with Grassmann variables instead of fermionic operators:

$$H(\mathbf{z}^*, \mathbf{z}) = J \sum_{\alpha, \beta} \sum_{\langle i, j \rangle} z_{i\alpha}^* z_{j\beta}^* z_{j\alpha} z_{i\beta} \quad (1.71)$$

To take into account that in our model, the number of particle per site is fixed, the following constraint has to be enforced:

$$m = \sum_{\alpha} \hat{c}_{i\alpha}^{\dagger} \hat{c}_{i\alpha} \longrightarrow m = \sum_{\alpha} z_{i\alpha}^* z_{i\alpha} \quad (1.72)$$

In the path integral formalism, it takes the form of local Lagrange multipliers $i\lambda_i$. By inserting this constraint and (1.71) in (1.67), we get:

$$Z = \int \mathcal{D}^2 \mathbf{z} \mathcal{D} \lambda \exp \left(- \int_0^{\beta} \sum_{\alpha} \sum_i z_{i\alpha}^* \partial_{\tau} z_{i\alpha} + i \lambda_i (m - z_{i\alpha}^* z_{i\alpha}) + J \sum_{\alpha, \beta} \sum_{\langle i, j \rangle} z_{i\alpha}^* z_{j\beta}^* z_{j\alpha} z_{i\beta} d\tau \right) \quad (1.73)$$

where the measure:

$$\mathcal{D} \lambda = \frac{1}{(2\pi)^n} \prod_{i=1}^n d\lambda_i \quad (1.74)$$

allows for each $i\lambda_i$, an integration over $(-\infty, +\infty)$ that produces a δ -function enforcing (1.72). It should be reminded that in equation (1.73) the variables $z_{i\alpha}$, $z_{i\alpha}^*$ and λ_i depend on τ , even if the explicit notation is absent.

The equation (1.73) is quartic in Grassmann variables. To solve this issue, one can now proceed to a Hubbard-Stratonovich transformation by first introducing $Z_{ij} = z_{i\alpha}^* z_{j\alpha}$ with an implicit summation over the colour index. These new variables are pairs of Grassmann variables that behave as \mathbb{C} -numbers. Due to (A.5), Z_{ij} satisfy the property $Z_{ij}^* = z_{j\alpha}^* z_{i\alpha}$. The quartic term becomes:

$$J \sum_{\alpha, \beta} \sum_{\langle i, j \rangle} z_{i\alpha}^* z_{j\beta}^* z_{j\alpha} z_{i\beta} = -J \sum_{\alpha, \beta} \sum_{\langle i, j \rangle} z_{j\beta}^* z_{i\beta} z_{i\alpha}^* z_{j\alpha} = -J \sum_{\langle i, j \rangle} Z_{ij}^* Z_{ij} = -J \sum_{\langle i, j \rangle} |Z_{ij}|^2 \quad (1.75)$$

For each neighbour $\langle i, j \rangle$, an auxiliary complex field Q_{ij} can be introduced via the identity:

$$\exp(-J|Z_{ij}|^2) = \int \frac{d^2 Q_{ij}}{J} \exp \left(\left| \sqrt{J} Z_{ij} + \frac{Q_{ij}^*}{\sqrt{J}} \right|^2 - J|Z_{ij}|^2 \right) \quad (1.76)$$

$$= \int \frac{d^2 Q_{ij}}{J} \exp \left(Q_{ij} Z_{ij} + Q_{ij}^* Z_{ij}^* + \frac{|Q_{ij}|^2}{J} \right) \quad (1.77)$$

$$= \int \frac{d^2 Q_{ij}}{J} \exp \left(\sum_{\alpha} \left(Q_{ij} z_{i\alpha}^* z_{j\alpha} + Q_{ij}^* z_{j\alpha}^* z_{i\alpha} \right) + \frac{|Q_{ij}|^2}{J} \right) \quad (1.78)$$

We see that thanks to this transformation, the term that mixed fermions of different colour has now disappeared. Gathering (1.73), (1.75) and (1.78), the partition function takes the form:

$$Z = \int \mathcal{D}^2 \mathbf{z} \mathcal{D}^2 \mathbf{Q} \mathcal{D} \lambda \exp(-S[\mathbf{z}^*, \mathbf{z}, \mathbf{Q}, \lambda]) \quad (1.79)$$

Chapter 1. The $SU(N)$ Heisenberg model

where we defined:

$$S[\mathbf{z}^*, \mathbf{z}, Q, \lambda] \equiv \int_0^\beta \left(L[\mathbf{z}^*, \mathbf{z}] + \sum_{\langle i,j \rangle} \frac{|Q_{ij}|^2}{J} - im \sum_i \lambda_i \right) d\tau \quad (1.80)$$

$$L[\mathbf{z}^*, \mathbf{z}] \equiv \sum_\alpha \left(\sum_i z_{i\alpha}^* (\partial_\tau + i\lambda_i) z_{i\alpha} + \sum_{\langle i,j \rangle} \left(Q_{ij} z_{i\alpha}^* z_{j\alpha} + Q_{ij}^* z_{j\alpha}^* z_{i\alpha} \right) \right) \quad (1.81)$$

$$\mathcal{D}^2 Q \equiv \prod_{\langle i,j \rangle} \frac{d^2 Q_{ij}}{J} \quad (1.82)$$

This Lagrangian only involves terms like $G_{ij}^{-1} z_i^* z_j$, therefore the Grassmann fields can formally be integrated out to get $G[Q, \lambda]$. The effective action then depends only on the auxiliary fields Q and λ :

$$Z = \int \mathcal{D}^2 Q \mathcal{D} \lambda \exp(-S_{\text{eff}}[Q, \lambda]) \quad (1.83)$$

with

$$S_{\text{eff}}[Q, \lambda] = N \text{Tr}(\ln(G[Q, \lambda])) + \int_0^\beta \sum_{\langle i,j \rangle} \frac{|Q_{ij}|^2}{J} - im \sum_i \lambda_i d\tau \quad (1.84)$$

Note that an overall N can be factorised in this action. Indeed the first term is related to (1.81) and the factor N is due to the sum over the decoupled colours. In the second term, J can be renormalised by N which amounts to multiply (1.70) by a constant which does not change the physic. The last term depends on m which can be expressed as $m = N/k$ for a fixed value of k . As N does not appear anywhere else, the large N limit provides a way to integrate over Q and λ with a saddle point approximation which will become exact. Therefore integrating (1.79) over Q and λ at the saddle point defined by the two conditions:

$$\left. \frac{\delta S}{\delta Q_{ij}} \right|_{Q_{ij} \rightarrow \chi_{ij}, \lambda_i \rightarrow i\mu_i} = 0 \quad \left. \frac{\delta S}{\delta \lambda_i} \right|_{Q_{ij} \rightarrow \chi_{ij}, \lambda_i \rightarrow i\mu_i} = 0 \quad (1.85)$$

results in the following mean-field Hamiltonian:

$$\hat{H}_{\text{MF}} = \sum_\alpha \sum_{\langle i,j \rangle} \left(\chi_{ij} \hat{c}_{i\alpha}^\dagger \hat{c}_{j\alpha} + \chi_{ij}^* \hat{c}_{j\alpha}^\dagger \hat{c}_{i\alpha} \right) + \sum_i \mu_i \left(m - \sum_\alpha \hat{c}_{i\alpha}^\dagger \hat{c}_{i\alpha} \right) + N\epsilon_0 \quad (1.86)$$

with

$$\epsilon_0 \equiv \sum_{\langle i,j \rangle} \frac{|\chi_{ij}|^2}{J} \quad (1.87)$$

The fermionic operators have been reintroduced in place of the Grassmann variables. At the saddle point, the fields Q and λ are not varying and can be replaced by constants. To avoid confusion between the fluctuating fields and their value at the saddle point, the following

substitutions were introduced:

$$Q_{ij} \rightarrow \chi_{ij} \qquad \lambda_i \rightarrow i\mu_i \qquad (1.88)$$

In the low temperature limit, the saddle point equations can be replaced by an equivalent set of conditions:

$$\chi_{ij} = -J \sum_{\alpha} \langle \hat{c}_{j\alpha}^{\dagger} \hat{c}_{i\alpha} \rangle \qquad m = \sum_{\alpha} \langle \hat{c}_{i\alpha}^{\dagger} \hat{c}_{i\alpha} \rangle \qquad (1.89)$$

These conditions, together with the fact that the Hubbard-Stratonovich transformation has decoupled the different colours, allow us to write a mean-field Hamiltonian at the saddle point:

$$\hat{H}_{\text{MFS}} = \sum_{\alpha} \hat{H}_{\text{MFS}}^{\alpha} = N \hat{H}_{\text{MFS}}^{\alpha} \qquad (1.90)$$

with

$$\hat{H}_{\text{MFS}}^{\alpha} = \sum_{\langle i,j \rangle} \left(\chi_{ij} \hat{c}_i^{\dagger} \hat{c}_j + \chi_{ij}^{*} \hat{c}_j^{\dagger} \hat{c}_i \right) + \epsilon_0 \qquad (1.91)$$

for which the constraints are:

$$\chi_{ij} = -JN \langle \hat{c}_j^{\dagger} \hat{c}_i \rangle \qquad m = N \langle \hat{c}_i^{\dagger} \hat{c}_i \rangle \qquad (1.92)$$

2 Numerical Methods

In the previous part, we introduced the $SU(N)$ Heisenberg model and showed how it can be solved in the mean-field limit. It is also possible to tackle this problem using another analytical approach for systems which present some kind of order, the linear flavour wave theory (LWFT) [30, 31, 28]. But to go beyond these analytical approximations and to make progress on the general problem of the $SU(N)$ Heisenberg model with different irreps than the fundamental one, it would be very useful to have a flexible yet reliable numerical method that would allow to systematic study of this model.

As we want to study one and two-dimensional systems, density matrix renormalisation group (DMRG) is not an adequate solution. Quantum Monte Carlo (QMC) could potentially work for cases such as self-conjugate irreps for which there is no minus-sign problem. For exact diagonalisation methods, on a given cluster, the total Hilbert space grows very fast with N , and the standard approach that only takes advantage of the conservation of the colour number is limited to very small clusters for large N . Quite recently, Nataf and Mila [32] have developed a simple method to work directly in a given irrep for the $SU(N)$ Heisenberg model with the fundamental representation at each site, allowing to reach cluster sizes typical of $SU(2)$ for any N . This method can be extended to the case of more complicated irreps at each site, in particular totally antisymmetric irreps.

In this work, we have decided to test the potential of fermionic Gutzwiller projected wave functions using variational Monte Carlo (VMC). There are few motivations for this choice. This approach can be easily generalised to higher dimensions, as already shown for the fundamental representation in a number of cases [51, 25]. Moreover, it has been used by Paramekanti and Marston [40] for the self-conjugate representation in one and two dimensions. Hence the VMC algorithm has already been proven efficient in studying various irreps for one- and two-dimensional systems. On top of these two qualities, the VMC algorithm is not limited by the system size and recovers mean-field limit when N and m are large.

The first section of this chapter, will introduce the VMC method. As it relies on the optimisation of variational parameters, an optimisation algorithm will be presented in the second section.

Additionally, an attempt to apply the VMC algorithm to fully symmetric irreps will be presented in appendix C. As it will be explained, it turns out to be very problematic to use VMC to study these irreps.

2.1 Variational Monte Carlo

To compute the mean value of an operator on the state $|\Phi\rangle$, namely $\langle\Phi|\hat{O}|\Phi\rangle$, we can express $|\Phi\rangle$ using a general basis:

$$|\Phi\rangle = \sum_i c_i |\phi_i\rangle \quad (2.1)$$

The dimension of the Hilbert space in which this state lives can be very big. For instance, the number of states of the $SU(N)$ Heisenberg model grows with the system size n as:

$$\left(\frac{N!}{(N-m)!m!} \right)^n \quad (2.2)$$

for a fully antisymmetric representation with m particles per site. This number can directly be obtained using the factor over hook rule (1.32). The computation of the mean value then becomes:

$$\langle\Phi|\hat{O}|\Phi\rangle = \sum_{i,j} \langle\Phi|\phi_i\rangle \langle\phi_i|\hat{O}|\phi_j\rangle \langle\phi_j|\Phi\rangle \quad (2.3)$$

$$= \sum_i |\langle\Phi|\phi_i\rangle|^2 \sum_j \langle\phi_i|\hat{O}|\phi_j\rangle \frac{\langle\phi_j|\Phi\rangle}{\langle\phi_i|\Phi\rangle} \quad (2.4)$$

$$= \sum_i P_i O_i \quad (2.5)$$

If the basis $|\phi_i\rangle$ is chosen such that there is a small number of non-vanishing $O_{ij} \equiv \langle\phi_i|\hat{O}|\phi_j\rangle$ matrix elements, then the Monte Carlo algorithm may be an efficient way to compute mean values. The algorithm ALG. 1 gives the recipe to compute any observable \hat{O} on any state $|\Phi\rangle$ expressed in the basis of states $|\phi_i\rangle$.

Algorithm 1 Monte Carlo Metropolis algorithm

- 1: Choose an initial random state $|\phi_i\rangle$
 - 2: **repeat**
 - 3: **repeat**
 - 4: Add O_i to the sampling
 - 5: Choose another state $|\phi_{i'}\rangle$
 - 6: **until** $\frac{P_{i'}}{P_i} > \text{rand}(0, 1)$
 - 7: $|\phi_i\rangle \leftarrow |\phi_{i'}\rangle$
 - 8: **until** Converged
-

We will focus our interest on measuring the energy of the ground state. As for most systems the ground state is unknown, we will use a variational approach which consists of guessing and building a candidate ground state $|\Psi\rangle$. Then the energy $E = \langle \Psi | \hat{H} | \Psi \rangle$ of this candidate state gives an upper bound to the energy E_0 of the real ground state $|\Psi_0\rangle$. Indeed, if one writes $|\Psi_i\rangle$, the eigenstates of the Hamiltonian with eigenvalues E_i such that $E_i < E_{i+1}$, then:

$$E = \sum_i E_i \langle \Psi | \Psi_i \rangle \langle \Psi_i | \Psi \rangle \quad (2.6)$$

$$\geq E_0 \sum_i \langle \Psi | \Psi_i \rangle \langle \Psi_i | \Psi \rangle \quad (2.7)$$

$$\geq E_0 \langle \Psi | \Psi \rangle \quad (2.8)$$

We can construct a wave function $|\Psi\rangle$ that depends on some parameters. By tuning these parameters, it is possible to lower the energy and eventually capture the correct physics of the ground state. In the following, we will demonstrate how to build a specific type of fermionic variational wave functions that we will focus on and how the Monte Carlo Metropolis algorithm can be applied to the $SU(N)$ Heisenberg model.

2.1.1 Gutzwiller projected variational wave functions

In practice, the construction of a Gutzwiller projected wave function starts with the creation of a variational Hamiltonian \hat{T} that acts on n sites and is written with fermionic operators $\hat{c}_{i\alpha}$ and $\hat{c}_{i\alpha}^\dagger$. We want this Hamiltonian to be easily diagonalisable and to depend on some variational parameters, *e.g.* hopping terms, phases, chemical potentials, *etc.* When different colours are involved in \hat{T} , and as long as there is no term mixing different colours, the Hamiltonian can be rewritten as a direct sum:

$$\hat{T} = \bigoplus_{\alpha=1}^N \hat{T}_\alpha \quad (2.9)$$

Each of the \hat{T}_α can be different and along this work we chose to use variational Hamiltonians of the the following form:

$$\hat{T}_\alpha = \sum_{i,j} \left(t_{ij,\alpha} \hat{c}_{i\alpha}^\dagger \hat{c}_{j\alpha} + t_{ij,\alpha}^* \hat{c}_{j\alpha}^\dagger \hat{c}_{i\alpha} \right) + \sum_i \mu_{i\alpha} \hat{c}_{i\alpha}^\dagger \hat{c}_{i\alpha} \quad (2.10)$$

where $t_{ij,\alpha} \in \mathbb{C}$ and $\mu_{i,\alpha} \in \mathbb{R}$ are variational parameters. This choice is motivated by the mean-field Hamiltonian (1.91) which allows hopping between different sites. The on-site chemical potential is also present in the mean-field theory even if it vanishes at the saddle point.

For each colour, there will be one corresponding unitary matrix U^α that diagonalises \hat{T}_α . So the new fermionic operators are given by:

$$\hat{f}_{i\alpha} = \sum_{j=1}^n U_{ij}^{\alpha\dagger} \hat{c}_{j\alpha} \quad \hat{f}_{i\alpha}^\dagger = \sum_{j=1}^n U_{ji}^\alpha \hat{c}_{j\alpha}^\dagger, \quad (2.11)$$

Chapter 2. Numerical Methods

and the variational Hamiltonian can be written in a diagonal basis:

$$\hat{T} = \sum_{\alpha=1}^N \sum_{i=1}^n \omega_{i\alpha} \hat{f}_{i\alpha}^\dagger \hat{f}_{i\alpha} \quad (2.12)$$

with $\omega_{i\alpha} < \omega_{i+1\alpha}$.

By filling the system with the nm/N lowest energy states of each colour, the resulting fermionic wave function contains nm particles:

$$|\Psi\rangle = \prod_{\alpha=1}^N \prod_{i=1}^{nm/N} \hat{f}_{i\alpha}^\dagger |0\rangle = \prod_{\alpha=1}^N \prod_{i=1}^{mn/N} \sum_{j=1}^n U_{ji}^\alpha \hat{c}_{j\alpha}^\dagger |0\rangle \quad (2.13)$$

If the nm/N and $(nm/N) + 1$ lowest eigenvalues are degenerate, the choice of eigenvector is undefined and the variational wave function is not safe to use. This is known as the degeneracy problem at the Fermi level and we will sometimes use different boundary conditions to solve this problem.

These fermionic wave functions contain on average m particles per site. To enforce the constraint of having exactly m particles per site which correspond to a Mott insulating phase, a Gutzwiller projector \hat{P}_G^m is applied on $|\Psi\rangle$. This projector removes all states with a number of particles per site different from m :

$$\hat{P}_G^m = \prod_{i=1}^n \prod_{p \neq m} \frac{\hat{n}_i - p}{m - p} \quad (2.14)$$

where the product over p runs over all values from 0 to N except $p = m$. The relevant resulting wave function is:

$$|\Psi_G\rangle = \hat{P}_G^m |\Psi\rangle. \quad (2.15)$$

The states that satisfy the constraints of having m particles per sites will be noted:

$$|\mathcal{C}\rangle \equiv \bigotimes_{\alpha=1}^N |\mathcal{C}_\alpha\rangle \equiv |\mathcal{C}_A\rangle \otimes |\mathcal{C}_B\rangle \cdots \otimes |\mathcal{C}_N\rangle \quad (2.16)$$

where $|\mathcal{C}_\alpha\rangle$ is a state built only with particles of colour α . The states $|\mathcal{C}\rangle$ are defined such that the following rules are satisfied:

$$\forall i, \quad \sum_{\alpha=1}^N \hat{c}_{i\alpha}^\dagger \hat{c}_{i\alpha} |\mathcal{C}\rangle = m \quad (2.17)$$

$$\forall \alpha, \beta, \quad \sum_{i=1}^n \hat{c}_{i\alpha}^\dagger \hat{c}_{i\alpha} |\mathcal{C}\rangle = \sum_{i=1}^n \hat{c}_{i\beta}^\dagger \hat{c}_{i\beta} |\mathcal{C}\rangle \quad (2.18)$$

Following the definition (2.16), we see that an additional convention has been fixed. A state $|\mathcal{C}\rangle$ is well defined, if the colours are ordered. This means that when $|\mathcal{C}\rangle$ is written in terms of

a product of $\hat{c}_{i\alpha}^\dagger$, the operators are sorted with increasing colour index from left to right. These states are not basis states of the $SU(N)$ irrep because they do not have the proper symmetries. Nevertheless, they generate all possible colour configurations. The variational Gutzwiller wave functions can finally be expressed as:

$$|\Psi_G\rangle = \bigotimes_{\alpha=1}^N \sum_{\mathcal{C}_\alpha} \det(\mathcal{C}_\alpha) |\mathcal{C}_\alpha\rangle = \sum_{\mathcal{C}} \det(\mathcal{C}) |\mathcal{C}\rangle \quad (2.19)$$

The fact that the Gutzwiller projector allows us to rewrite the wave function as a sum over all colour configurations weighted by a determinant is justified by a simple example given in appendix B.1. This formulation simplifies the computation of the projection of $|\Psi_G\rangle$ on any configuration $|\mathcal{C}\rangle$:

$$\langle \mathcal{C} | \Psi_G \rangle = \sum_{\mathcal{C}'} \det(\mathcal{C}') \langle \mathcal{C} | \mathcal{C}' \rangle = \det(\mathcal{C}) \quad (2.20)$$

We have introduced a convenient way of computing the Gutzwiller projected wave functions. In the following, we will see how they can be used in the VMC algorithm.

2.1.2 VMC with fermionic Gutzwiller projected wave function

We presented a way to rewrite the Gutzwiller projected wave functions using determinants of matrices built with components of eigenvectors of a variational Hamiltonian. Let us see now what are the benefices of this formulation for the VMC algorithm.

It is remarkable to note that computing the mean value of \hat{H} with the formula (2.4) amounts to compute ratios of determinants. Indeed, at a given step of the Monte Carlo process, the system will be in a configuration $|\mathcal{C}\rangle$ and one needs to compute:

$$\sum_{\mathcal{C}'} \langle \mathcal{C} | \hat{H} | \mathcal{C}' \rangle \frac{\langle \mathcal{C}' | \Psi_G \rangle}{\langle \mathcal{C} | \Psi_G \rangle} = \sum_{\mathcal{C}'_{\mathcal{C}}} \text{sgn}(\mathcal{C}'_{\mathcal{C}}) \frac{\det(\mathcal{C}')}{\det(\mathcal{C})} \quad (2.21)$$

where $\mathcal{C}'_{\mathcal{C}}$ means that the sum is taken over all configurations $|\mathcal{C}'\rangle$ that are connected to $|\mathcal{C}\rangle$. The sign function $\text{sgn}(\mathcal{C}'_{\mathcal{C}})$ is negative when the permutation involves two fermions of different colours because the operators must be reordered. If $\alpha = \beta$, then no reordering is required and the positive sign is chosen. More precisely, as the Hamiltonian consists of a sum of $\hat{c}_{i\alpha}^\dagger \hat{c}_{i\beta} \hat{c}_{j\beta}^\dagger \hat{c}_{j\alpha}$, two configurations are connected if $\langle \mathcal{C} | \hat{c}_{i\alpha}^\dagger \hat{c}_{i\beta} \hat{c}_{j\beta}^\dagger \hat{c}_{j\alpha} | \mathcal{C}' \rangle = \text{sgn}(\mathcal{C}'_{\mathcal{C}})$.

The algorithm ALG. 1 presented in the previous section can now be applied to our particular problem. The algorithm given in ALG. 2 illustrates the main steps written in pseudocode language. As this algorithm requires the computation of many determinants (steps ALG. 2₅ and ALG. 2₇), appendix B.2 proposes some useful tricks to speed up these time consuming operations.

Algorithm 2 Variational Monte Carlo algorithm

- 1: Choose an initial random configuration \mathcal{C}
 - 2: Thermalisation
 - 3: **repeat**
 - 4: **repeat**
 - 5: Add $\left(\sum_{\mathcal{C}' \in \mathcal{C}} \text{sgn}(\mathcal{C}' \mathcal{C}) \frac{\det(\mathcal{C}')}{\det(\mathcal{C})} \right)$ to the sampling
 - 6: Randomly choose another configuration \mathcal{C}'
 - 7: **until** $\left| \frac{\det(\mathcal{C}')}{\det(\mathcal{C})} \right|^2 > \text{rand}(0, 1)$
 - 8: $\mathcal{C} \leftarrow \mathcal{C}'$
 - 9: **until** Converged
 - 10: Finalise the simulation
-

ALG. 2₁ We start by randomly choosing a configuration for which the determinant is not zero. In theory this corresponds to any state satisfying the Pauli principle but in practice, the weight of the state, *i.e.* the determinant, cannot be too small otherwise the simulation does not converge.

ALG. 2₂ As the initial state may have a very peculiar weight, a thermalisation phase is required.

ALG. 2₅ At each step of the Monte Carlo process, the current configuration is measured. This is where code computes different observables like the energy, the bond energies, the correlations, the colour occupation, *etc.*

ALG. 2₈ Test the new configuration and decide whether it is kept or discarded.

ALG. 2₁₀ At the end of the simulation, the statistical errors on the observables are computed. This is done thanks to a binning analysis well explained in reference [52].

2.2 Particle Swarm Optimisation

In this section, we will present the algorithm that attempts to find the variational set of parameters that minimises the energy. Let us first make some remarks on the kind of properties required by the algorithm. As the Monte Carlo algorithm measures the variational energies with some uncertainty, a difficulty arises. Indeed, assume we were to use some kind of gradient's method to perform the minimisation of $f(x)$. As we do not know the form of the function to minimise, the derivatives must be approximated by:

$$f'(x) = \frac{f(x + \delta) - f(x)}{\delta} \quad (2.22)$$

Measuring f at the points x_1 and x_2 with Monte Carlo would give $f_e(x_1) \pm \Delta_1$ and $f_e(x_2) \pm \Delta_2$, where $f_e(x)$ is the exact value of f at the point x and Δ is the error made by the sampling. The

gradient method would select the next point x_3 according to:

$$x_3 = x_2 + \lambda \frac{f_e(x_1) - f_e(x_2) \pm (\Delta_1 - \Delta_2)}{x_1 - x_2}, \quad \lambda \in \mathbb{R} \quad (2.23)$$

When $|f_e(x_1) - f_e(x_2)| < |\Delta_1 - \Delta_2|$, the uncertainties Δ_1 and Δ_2 might lead to an approximation of the derivative having the wrong sign and the algorithm would never converge. To solve this problem, we would need to reduce the uncertainties as much as possible by increasing the simulation time. However this would not be efficient and it would not be possible to minimise a problem with more than a couple of free variational parameters. Therefore more sophisticated methods should be used.

Instead of using a deterministic method, one can choose a stochastic algorithm. The Particle Swarm Optimisation (PSO) algorithm figures among many options. This algorithm has been introduced by Kennedy, Eberhart and Shi [53, 54] and, as its name indicates, this algorithm aims to describe the social behaviour of a swarm of particles, *e.g.* bees, birds, fish *etc.* It is most easily understood by using the example of a swarm of bees that wants to optimise the collect of pollen extracted from flowers spread in a field. Even if their behaviour looks erratic, a very simple model that efficiently describes their location and motion in space can be summed up with two basic rules. A bee (p) is attracted towards the location of the most resourceful flower (l_p) that it has discovered, and towards the location of the most resourceful flower known to the swarm (l). The interesting point is that, beside providing a qualitatively good description of a swarm, this algorithm happens to perform optimisation [55].

There are many variants of the PSO algorithm. After having tried some of them, a rather simple one has been selected [56, 57] and is given in the pseudocode of ALG. 3. Some of the key steps will be described in the following.

ALG. 3₁ Initialisation and Topology choice: The topology of the swarm describes how the particles are connected. There are many possible topologies. One could imagine to split the swarm into sub-swarms, each of them being independent, or each particle p could solely be connected to the particles $p \pm 1$, or to their closest neighbours in the parameter space *etc.*

The choice made here was to use the trivial topology, where each particle is equally connected to all other particles. Therefore, at the beginning of the simulation, each particle p is randomly set at a given location in the parameter space x^p and best known locations are set: $l^p = f(x^p)$ and $l = \min_p l^p$.

ALG. 3₅ Velocity update: During the minimisation process, each particle moves at a non-zero velocity. This mean that when a particle finds an optimal location x^p , the terms $(l_k^p - x_k^p)$ and $(l_k - x_k^p)$ in ALG. 3₅ will vanish. But as we want to continue exploring the parameter space, we give inertia to the particles. The way the velocity is updated is extremely important, we introduce additional parameters.

Algorithm 3 Particle Swarm Optimisation algorithm for a swarm of P particles living in a D -dimensional space, where the dimension k is bounded by $[L_k, R_k]$. A particle p , located at x^p with velocity v^p , is aware of the swarm's best location l and its own best known location l^p .

```

1: Initialise a swarm of  $n$  particles in a given topology
2: repeat
3:   for  $p \leftarrow 1, P$  do
4:     for  $k \leftarrow 1, D$  do
5:        $v_k^p \leftarrow \chi (v_k^p + \phi_1 r_1 (l_k^p - x_k^p) + \phi_2 r_2 (l_k - x_k^p))$ 
6:        $x_k^p \leftarrow x_k^p + v_k^p$ 
7:       if  $x_k^p \notin [L_k, R_k]$  then
8:         Reset  $(x_k^p, v_k^p)$ 
9:       end if
10:    end for
11:    if  $f(l^p) > f(x^p)$  then
12:       $l^p \leftarrow x^p$ 
13:    end if
14:  end for
15:  for  $p \leftarrow 1, n$  do
16:    if  $f(l) > f(l^p)$  then
17:       $l \leftarrow l^p$ 
18:    end if
19:  end for
20: until Stopping criterion met

```

Constriction factor (χ): Introduced by Clerc [57], this parameter prevents the possible explosion of the velocities and increases the convergence speed. It is defined as follows [56]:

$$\chi = \frac{2}{-2 + (\phi_1 + \phi_2) + \sqrt{(\phi_1 + \phi_2)^2 - 4(\phi_1 + \phi_2)}} \quad \text{for } \phi_1 + \phi_2 > 4 \quad (2.24)$$

with some constants ϕ_1 and ϕ_2 .

Independance (ϕ_1) and social (ϕ_2) weights: These parameters set the maximal tendency that a particle has to move towards its best known location l^p or the swarm's best known location l [54]. If $\phi_1 \gg \phi_2$, then the particles are independent, they are mostly attracted towards their own best known location, while if $\phi_1 \ll \phi_2$, all particles are attracted towards the swarm's best known location.

For our purpose, these weights are set to be equal to $\phi_2 = \phi_1 = 2.1$ so that the condition (2.24) is satisfied.

Uniform random number (r_1 and r_2): At each step new random numbers are generated in the interval $[0, 1]$.

ALG. 3₇₋₉ Boundary condition: The PSO algorithm is usually defined for an open parameter space, but if the parameter space has some boundaries, there are different strategies to

handle a situation where the position of a particle is updated such that $x_k^p \notin [L_k, R_k]$ [58]. The strategy chosen here is known as the exponential distribution strategy and is defined as follows. For each dimension, consider a particle originally at location x_a in an allowed interval $[L, R]$ as depicted in FIG. 2.1.

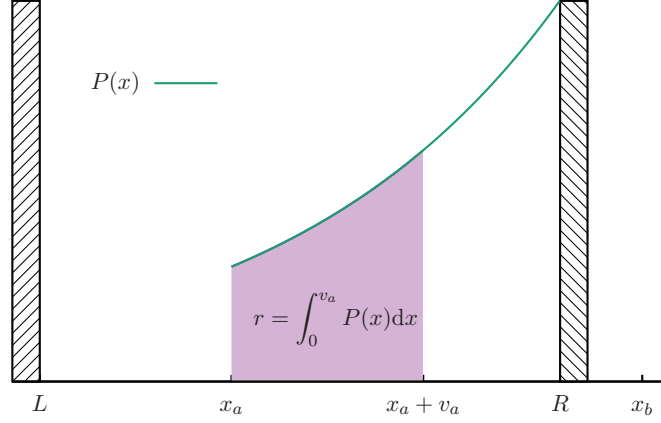


Figure 2.1 – Schematic view of a particle in a one-dimensional space with boundary condition. The curve represents the probability $P(x)$ while the surface of the coloured region is r .

The particle is then supposed to move to the location x_b , but as it is outside the sampling range, $x_b > R$, it is reset at location $x = x_a + v \in [L, R]$ following the exponential distribution $P(x)$ defined as:

$$P(x) = A e^x \quad \text{with } A \text{ such that} \quad \int_0^{R-x_a} P(x) dx = 1 \quad (2.25)$$

In practice, a uniformly distributed random number r is chosen in the interval $[0, 1]$, v_a is then obtained by inverting the equation:

$$r = \int_0^{v_a} P(x) dx \Rightarrow v_a = \ln(1 + r/A) \quad (2.26)$$

Note that v_a plays the role of the velocity v in the algorithm and hence, this strategy also redefines the velocity as $v = v_a$. An equivalent condition exists when $x_b < L$, but this time $v = -v_a$ and $x = x_a + v$.

ALG. 3₁₁₋₁₃: This block corresponds to the update of the particle best known location.

ALG. 3₁₅₋₁₉: The swarm's best known location is updated.

In the context of the $SU(N)$ Heisenberg model studied with VMC, the location of a particle corresponds to a given set of variational parameters with corresponding variational energy. When a particle moves in the parameter space, the related variational energy will change. The lowest variational energy reached by a particle p corresponds to the best set of variational parameters

or location l_p . The optimal location l is simply the best set of variational parameters found by any particle. The figure FIG. 2.2 represents the update of the position of three particles in a two-dimensional parameter space and should clarify the rules obeyed by the particles.

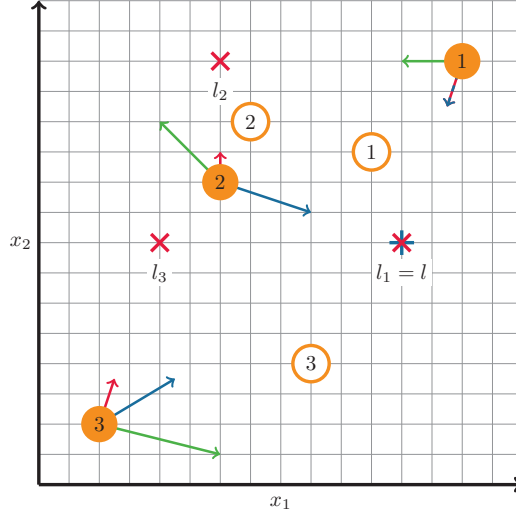


Figure 2.2 – Schematic representation of the PSO algorithm. Three particles are moving in a two-dimensional space (x_1, x_2) . At a given step, the particles (filled circles) have a given velocity (green arrow) and are attracted towards l_p , their best known location (red cross), and towards l , the best known location of the swarm (blue cross). For each particle, the next location (empty circles) is determined by the velocity and relative position from l_p and l .

Now that the general features of the PSO algorithm have been defined and explained, it is time to see why and how it can be applied to find a set of optimal variational parameters. As it was explained earlier, the VMC algorithm measures energies with some uncertainty. This has some consequences in the way this PSO algorithm is implemented. At each step a particle has to decide, whether the current location \mathbf{x} in the parameter space parameter with energy $E_{\mathbf{x}} \pm \Delta_{\mathbf{x}}$ has to replace the best known location \mathbf{x}_0 with energy $E_0 \pm \Delta_0$. The two possible decisions are:

1. $E_{\mathbf{x}} < E_0$: The best set of parameters is replaced by the current one ($\mathbf{x}_0 \leftarrow \mathbf{x}$).
2. $E_{\mathbf{x}} > E_0$: The best set of parameters is left unchanged.

The uncertainties on the measure may be problematic if $|E - E_0| \lesssim \Delta_{\mathbf{x}} + \Delta_0$. Indeed, when the energy difference is of the order of magnitude of the uncertainties, the decision made can be wrong. When this happens, the PSO minimisation might fail. Imagine a situation, where at a given step, the parameter set \mathbf{x}_0 with measured energy $E_0 \pm \Delta_0$ is optimal. All particles will be attracted towards \mathbf{x}_0 , and we may believe that the simulation has converged. But if the uncertainty Δ_0 is large, it is possible that a more accurate measure would give a bigger, non optimal E_0 . In order to avoid this problem, the measure of E_0 should be improved during the optimisation process. As most of the parameter sets have a non competitive energy, the

improvement on the measure should only occur when needed. A simple and efficient solution is to give the chance to each particle to improve the energy of an already measured parameter set. Unfortunately, with a continuous parameter space, the probability to measure again the energy for a particular parameter set is zero. The solution to this issue is simply to discretise the parameter space by only allowing parameter sets of the form $\mathbf{x} = \delta_k n_k \hat{e}_k$ where $\delta_k \in \mathbb{R}$, $n_k \in \mathbb{Z}$ and \hat{e}_k is a unit vector pointing of the direction k (the k -th degree of freedom) of the D -dimensional parameter space. Now, if the same scenario happens, there is a good probability to measure again the parameter set \mathbf{x}_0 and increase the precision on its related variational energy. When a parameter set is measured again, another issue arises. Consider a situation, where current optimal parameter set \mathbf{x}_0 is measured again and has a higher energy. It will certainly not be the optimal parameter set anymore. Therefore, a new optimal parameter set has to be selected. A reliable way to do that is to give memory to the particles. If a particle remembers all its previous locations and measures, it will be able to define its new optimal location and will be attracted towards it. To explain this paragraph in a more pictorial way, let us come back to our bees and flowers. If a bee finds a nice flower, the swarm will be attracted to that flower. Another bee might fly to that flower, and if it turns out that the previous bee has over-estimated the quantity of pollen, it will warn the swarm and fly back to another more resourceful flower. Note that it also works the other way. If a bee neglects a flower, another one might try the same flower and realise its potential.

When an already measured set of parameters is measured again, it is not efficient to recreate the wave function (requires time-consuming steps like diagonalisation), find an initial state (takes time due to the explicit computation of many determinants) and thermalise the Monte Carlo sampling again. Thus the solution is to keep in memory some key variables (eigenvectors, last configuration sampled, *etc.*) allowing a fast re-initialisation of the Monte Carlo algorithm. The drawback of keeping in memory the history of all particle is that it may overload the memory of the computer.

Even if this method does not guarantee that the solution found is the optimal solution, it fulfills all requirements. Additionally, one of the strengths of this algorithm is that it can be parallelised. Indeed, each particle is independent and can sample a different set of parameters.

One dimensional systems **Part II**

3 Chain

The aim of this chapter is to study the $SU(N)$ Heisenberg model on a chain for various fully antisymmetric irreps. For the 1-dimensional systems, apart from a few specific cases [59, 60, 40, 61, 62, 63, 64, 65, 66, 67], including more general irreps than simply the totally antisymmetric ones, the most general results have been obtained by Affleck quite some time ago [33, 34]. Applying non-abelian bosonisation to the weak coupling limit of the $SU(N)$ Hubbard model, he identified two types of operators that could open a gap: Umklapp terms if $N > 2$ and $N/m = 2$, and higher-order operators with scaling dimension $\chi = N(m-1)m^{-2}$ allowed by the $\mathbb{Z}_{N/m}$ symmetry if N/m is an integer strictly larger than 2. This allowed him to make predictions in four cases: i) N/m is not an integer: the system should be gapless because there is no relevant operator that could open a gap; ii) $N > 2$ and $N/m = 2$: the system should be gapped because Umklapp terms are always relevant; iii) N/m is an integer strictly larger than 2 and $\chi < 2$: the system should be gapped because there is a relevant operator allowed by symmetry. This case is only realised for $SU(6)$ with $m = 2$; iv) N/m is an integer strictly larger than 2 and $\chi > 2$: the system should be gapless because there is no relevant operator allowed by symmetry. The only case, where the renormalisation group argument based on the scaling dimension of the operator does not lead to any prediction is the marginal case $\chi = 2$, which is realised for two pairs of parameters: $(SU(8) \ m = 2)$ and $(SU(9) \ m = 3)$. These predictions are summarised in TAB. 3.1. Finally, in all gapless cases, the system is expected to be in the $SU(N)_{k=1}$ Wess-Zumino-Witten universality class [68, 33], with algebraic correlations that decay at long distance with a critical exponent $\eta = 2 - 2/N$.

To systematically investigate the predictions discussed by Affleck, we will use two numerical methods. The first one is the VMC with simple fermionic wave functions that, before projection, correspond to the ground state of variational Hamiltonians that contain only hopping terms. For $SU(2)$, the inclusion of pairing terms have been shown to lead to significant improvements [69], but the generalisation to $SU(N)$ is not obvious because one cannot make an $SU(N)$ singlet with two sites as soon as $N > 2$. In addition, in the case of the fundamental representation, where Bethe ansatz results are available for comparison, these simple wave functions turn out to lead to extremely precise results as soon as $N > 2$. This choice of wave

$N =$	3	4	5	6	7	8	9	10	$N/m \notin \mathbb{N}$	
$m = 1$									$m = 1$	} Gapless
$m = 2$									$\chi > 2$	
$m = 3$									$\chi = 2$	} ?
$m = 4$									$\chi < 2$	
$m = 5$									$N/m = 2$	} Gapped

Table 3.1 – Summary of the predictions of Refs. [33, 34] for a representative range of $SU(N)$ with m particles per site. Note that models with $m = l$ and $m = N - l$ are equivalent up to a constant. Therefore the light gray shaded region can be deduced from the other cases and does not need to be studied.

functions have been shown to be remarkably accurate in the case of the $SU(4)$ Heisenberg chain with the fundamental representation by Wang and Viswanath [23], who have in particular shown that they lead to the exact critical exponent in that case. The second numerical method used in this chapter is ED based on the extension of a recent formulation by Nataf and Mila [32]. This method will be used whenever possible to benchmark the VMC approach on small clusters and, in some cases, to actually confirm the physics on the basis of a finite-size analysis. As we shall see, the combination of these approaches leads to results that agree with Affleck's predictions whenever available, and to the identification of the symmetry breaking pattern in the gapped phases. In addition, it predicts that the marginal cases are gapless with algebraic correlations.

The chapter is organised as follows. The first section describes the variational wave functions that will be used throughout. The next section is devoted to a comparison of the results obtained using the simplest wave functions (with no symmetry breaking) with those of the Bethe ansatz solution for the $m = 1$ case, with the conclusion that the agreement is truly remarkable. The third section deals with the cases, where Umklapp processes are present ($N > 2$, $N/m = 2$), while the fourth one deals with the case where there is no Umklapp process but a relevant operator ($SU(6)$ $m = 2$). The marginal cases are dealt with in the fifth section, and the case where N/m is an integer without relevant nor Umklapp operators in the sixth section. Finally, the critical exponents are computed and compared to theoretical values for all gapless systems in the last section.

3.1 Variational wave functions

Since the Heisenberg model exchanges particles on neighboring sites, the simplest variational Hamiltonian that allows the hopping of particles and its corresponding Gutzwiller projected wave function are:

$$\hat{T}^{\text{Fermi}} = \sum_{i=1}^n \left(\hat{c}_i^\dagger \hat{c}_{i+1} + \text{h.c.} \right) \rightarrow |\Psi_G^{\text{Fermi}}\rangle. \quad (3.1)$$

In cases where a relevant or Umklapp operator is present, the ground state is expected to be a singlet separated from the first excited state by a gap, and to undergo a symmetry breaking that leads to a unit cell that can accommodate a singlet. In practice, this means unit cells with $d = N/m$ sites. To test for possible instabilities, we have thus used wave functions that are ground states of Hamiltonians that creates d -merisation:

$$\hat{T}^{t_i} = \sum_{i=1}^n \left(t_i \hat{c}_i^\dagger \hat{c}_{i+1} + \text{h.c.} \right) \rightarrow \left| \Psi_G^d(\delta) \right\rangle. \quad (3.2)$$

Assuming that the mirror symmetry is preserved, the wave functions $\left| \Psi_G^d(\delta) \right\rangle$ for dimerisation ($d = 2$) and trimerisation ($d = 3$) have only one allowed free parameter δ , and the hopping amplitudes in a unit cell are given by:

$$\begin{cases} t_i = 1 - \delta & \text{if } i = d \\ t_i = 1 & \text{otherwise.} \end{cases} \quad (3.3)$$

To test for a possible tetramerisation for SU(8) $m = 2$, since the unit cell contains four sites, one additional free parameter is allowed (still assuming that the mirror symmetry is preserved in the ground state). Therefore, we have used the wavefunction $\left| \Psi_G^4(\delta_1, \delta_2) \right\rangle$ with hopping amplitudes defined by:

$$\begin{cases} t_i = 1 - \delta_1 & \text{if } i = 2 \\ t_i = 1 - \delta_2 & \text{if } i = 4 \\ t_i = 1 & \text{otherwise.} \end{cases} \quad (3.4)$$

This method is always well defined for periodic boundary conditions when N/m is even. But when N/m is odd, the ground state is degenerate for periodic boundary conditions if the translation symmetry is not explicitly broken, and one has to use antiperiodic boundary conditions for $\left| \Psi_G^{\text{Fermi}} \right\rangle$, $\left| \Psi_G^d(0) \right\rangle$ ($d = 2, 3$) and $\left| \Psi_G^4(0, 0) \right\rangle$.

The hope is that if \hat{T} is wisely chosen, then $\left| \Psi_G \right\rangle$ captures correctly the physics of the ground state, i.e. with a good variational wave function, $E_G \equiv \langle \Psi_G | \hat{H} | \Psi_G \rangle \approx E_0$, the exact ground state energy. To check the pertinence of this statement, we have compared the energies and nearest-neighbor correlations with those computed with ED on small systems with open boundary conditions. In the table TAB. 3.2, one can see, for some systems, the comparison between ED and VMC results for the ground state energy. The nearest-neighbor correlations will be compared in the next sections. Considering the excellent agreement between the two methods for the cluster sizes available to ED, there are good reasons to hope that these Gutzwiller projected wave functions can quantitatively describe the properties of the ground state.

N	m	n	ED	VMC	error [%]
4	2	16	-1.6971	-1.6916	-0.33
4	2	18	-1.6925	-1.6866	-0.35
6	2	15	-2.7351	-2.7287	-0.23
6	3	12	-4.0295	-4.0261	-0.08
6	3	14	-4.0162	-4.0123	-0.10
8	2	12	-3.1609	-3.1587	-0.07
8	2	16	-3.1857	-3.1828	-0.09
9	3	9	-6.0960	-6.0810	-0.25
9	3	12	-6.1162	-6.0980	-0.30
10	2	15	-3.3992	-3.3919	-0.21

Table 3.2 – Comparison between the ED and VMC energies per site. The incertitudes on the VMC data are smaller than 10^{-4} . The relative error is always smaller than 0.35%.

3.2 Correlation function and structure factor

To characterise the ground state, it will prove useful to study the diagonal correlation defined by:

$$C(x) = \sum_{\alpha} \langle \hat{S}_{\alpha\alpha}^0 \hat{S}_{\alpha\alpha}^x \rangle = \sum_{\alpha} \langle \hat{c}_{0\alpha}^{\dagger} \hat{c}_{0\alpha} \hat{c}_{x\alpha}^{\dagger} \hat{c}_{x\alpha} \rangle - \frac{m^2}{N}. \quad (3.5)$$

The structure factor is then given by the Fourier transform of this function:

$$\tilde{C}(k_x) = \frac{1}{2\pi} \frac{N}{m(N-m)} \sum_x C(x) e^{ik_x x} \quad (3.6)$$

where the prefactor has been chosen such that:

$$\sum_{k_x} \tilde{C}(k_x) = \frac{n}{2\pi}. \quad (3.7)$$

3.3 Results

3.3.1 $SU(N)$ with $m = 1$

In this section, we extend the $SU(4)$ results of Wang and Vishwanath [23] to arbitrary N for $m = 1$ (fundamental representation), and we perform a systematic comparison with Bethe ansatz and QMC results. Since these systems are known to be gapless, $|\Psi_G^{\text{Fermi}}\rangle$ is the only relevant wave function to study.

Let us start with the ground state energy. Using Bethe ansatz, Sutherland [15] derived an exact formula for the ground state energy per site $e_0(N)$ of the Hamiltonian (1.45) that can be written

as a series in powers of $1/N$:

$$e_0(N) = -1 + 2 \sum_{k=2}^{\infty} \frac{(-1)^k \zeta(k)}{N^k} \quad (3.8)$$

where

$$\zeta(k) = \sum_{n=1}^{\infty} \frac{1}{n^k} \quad (3.9)$$

is Riemann's zeta function. $e_0(N)$ is depicted in FIG. 3.1 as a continuous line. The dashed lines are approximations obtained by truncating the exact solution at order $N^{-\lambda}$, $\lambda \geq 2$. For comparison, the variational energies obtained in the thermodynamic limit after extrapolation from finite size systems are shown as dots in FIG. 3.1. The agreement with the exact solution is excellent for all values of N , and it improves when N increases (see table TAB. 3.3). Quite remarkably, the variational estimate is better than the N^{-4} estimate even for SU(3).

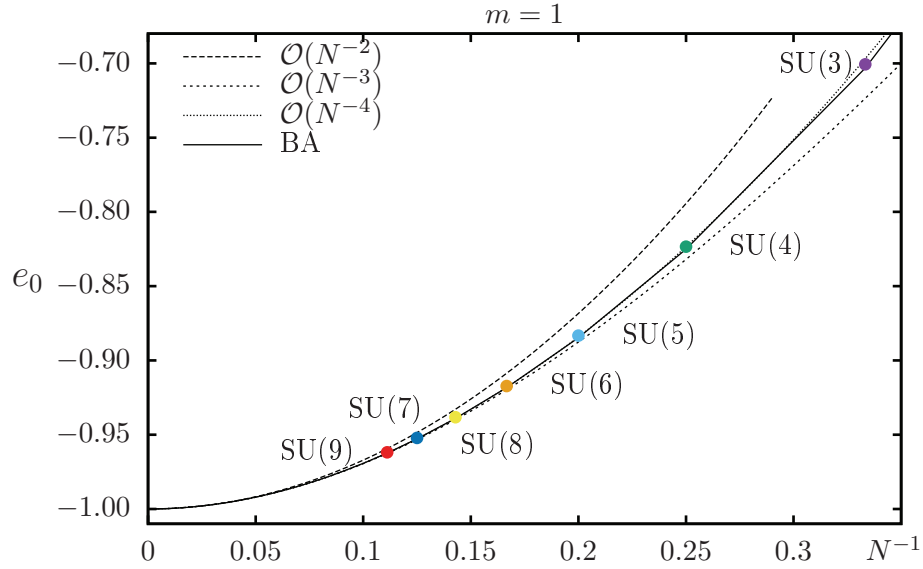


Figure 3.1 – Variational energy per site of SU(N) chains with the fundamental irrep at each site (dots) compared to Bethe ansatz exact results (solid line) and polynomial approximations in $1/N$ (dashed lines).

We now turn to the diagonal correlations and its associated structure factor defined by (3.5) and (3.6). At very low temperature, QMC has been used by Frischmuth, Mila, and Troyer [16] for SU(4) and by Messio and Mila [17] for various values of N to compute this structure factor. The QMC data [17] and the results obtained with VMC for $n = 60$ sites are shown in FIG. 3.2. Qualitatively, the agreement is perfect: VMC reproduces the singularities typical of algebraically decaying long-range correlations. But even quantitatively the agreement is truly remarkable, and, as for the ground state energy, it improves when N increases. Clearly, Gutzwiller projected wave functions capture the physics of the $m = 1$ case very well.

N	BA	VMC	error [%]
3	-0.7032	-0.7007	-0.36
4	-0.8251	-0.8234	-0.21
5	-0.8847	-0.8833	-0.16
6	-0.9183	-0.9173	-0.11
7	-0.9391	-0.9383	-0.09
8	-0.9528	-0.9522	-0.06
9	-0.9624	-0.9620	-0.05

Table 3.3 – Comparison of the variational energies for $m = 1$ systems obtained for infinite chains with exact Bethe ansatz. The incertitudes on the VMC data are smaller than 10^{-4} .

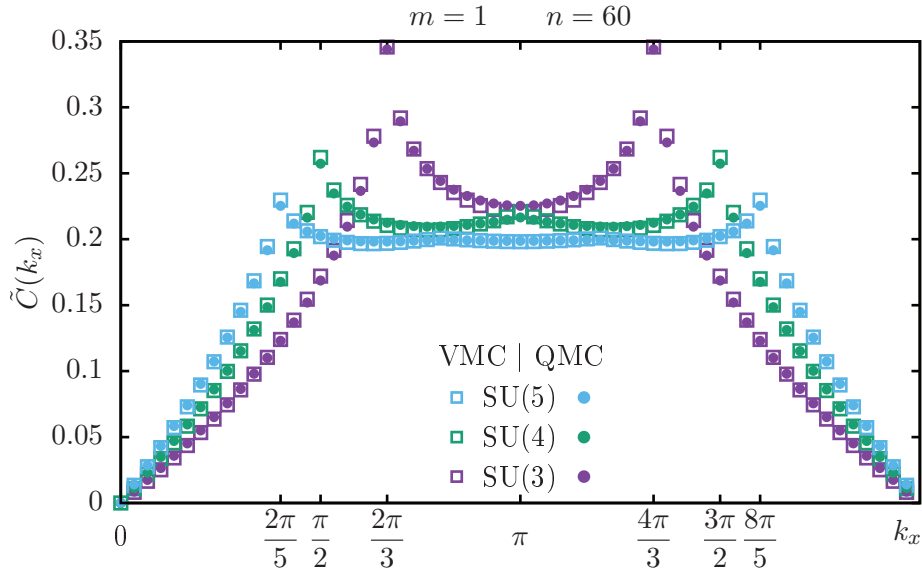


Figure 3.2 – Comparison of the structure factors calculated with VMC (empty squares) and QMC (filled circles) for various $SU(N)$ systems. In the VMC calculations, antiperiodic boundary conditions have been used for $SU(3)$ and $SU(5)$, and periodic ones for $SU(4)$.

3.3.2 $SU(N)$ with $m = N/2$

For these systems, there is a self-conjugate antisymmetric representation of $SU(N)$ at each site. The ground states of such systems, referred to as extended valence bound solids [70], are predicted to break the translational symmetry, to be two-fold degenerate and to exhibit dimerisation since only two sites are needed to create a singlet, and the spectrum is expected to be gapped.

We have investigated two representative cases, ($SU(4)$ $m = 2$) and ($SU(6)$ $m = 3$), with ED up to 18 and 14 sites respectively, and the cases $N = 4$ to 10 with VMC. The main results are summarised in FIG. 3.3. Let us start by discussing the ED results. Clusters with open boundary conditions have been used because they are technically simpler to handle with the method of Ref. [32], and because, in the case of spontaneous dimerisation, they give directly access to

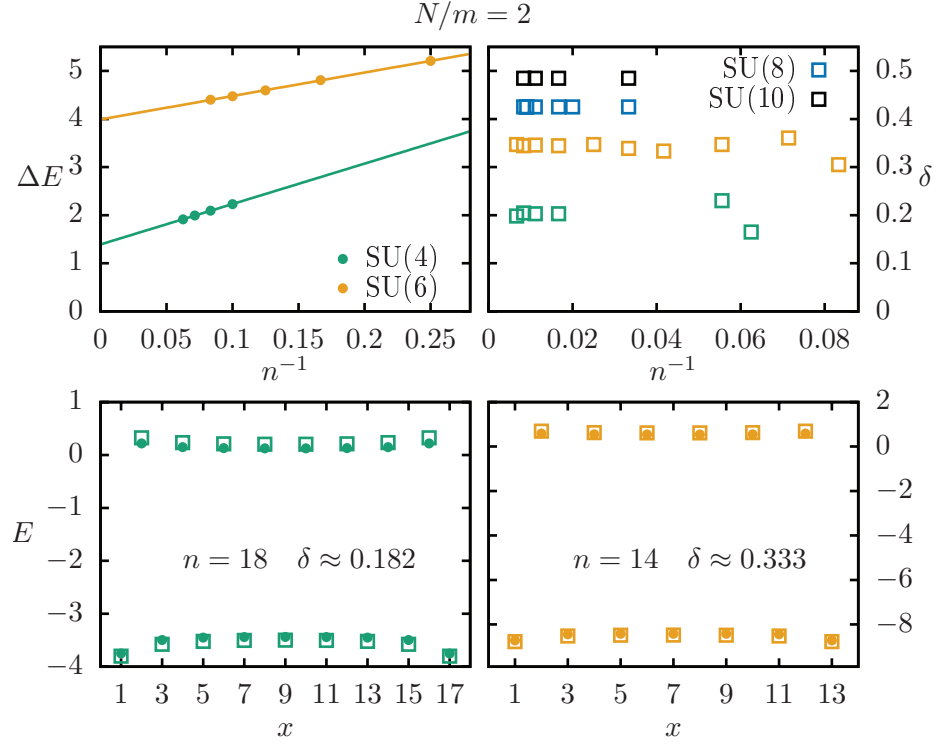


Figure 3.3 – ED and VMC results for various $SU(N)$ models with $m = N/2$. Upper left panel: size dependence of the energy gap for $SU(4)$ and $SU(6)$. Upper right panel: optimal variational parameter δ for periodic boundary conditions for $SU(4)$, $SU(6)$, $SU(8)$, and $SU(10)$. Lower panels: energy per bond for $SU(4)$ (left) and $SU(6)$ (right) calculated with ED (circles) and VMC (squares) for open boundary conditions. Note that the optimal variational parameters δ_{opt} are different in the upper right panel and in the lower panels because they correspond to different boundary conditions (periodic and open).

one of the broken symmetry ground states if the number of sites is even. The gap as a function of the inverse size is plotted in the upper left panel of FIG. 3.3 for $SU(4)$ and $SU(6)$. In both cases, the results scale very smoothly, and a linear fit is consistent with a finite and large value of the gap in the thermodynamic limit. In the lower panels of FIG. 3.3, the bond energy is plotted as a function of the bond position for the largest available clusters (18 sites for $SU(4)$, 14 sites for $SU(6)$) with solid symbols. A very strong alternation between a strongly negative value and an almost vanishing (slightly positive) value with very little dependence on the bond position clearly demonstrates that the systems are indeed spontaneously dimerised.

Let us now turn to the VMC results. Since the relevant instability is a spontaneous dimerisation, it is expected that the dimerised $|\Psi_G^2(\delta)\rangle$ wave function allows one to reach lower energy than the $|\Psi_G^{\text{Fermi}}\rangle$ one. This is indeed true for all cases we have investigated (up to $N = 10$ and to $n \gtrsim 100$), and the optimal value of the dimerisation parameter $\delta_{\text{opt}} > 0$ is nearly size independent and increases with N (see upper right panel of FIG. 3.3), in qualitative agreement with the gap increase between $SU(4)$ and $SU(6)$ observed in ED. To further benchmark the

Gutzwiller projected wave functions for these cases, we have calculated the bond energy using the optimal value of δ (open symbols in the lower panel of FIG. 3.3) for the same clusters as those used for ED with open boundary conditions. The results agree quantitatively very well.

With the large sizes accessible with VMC, it is also interesting to calculate the diagonal structure factor defined in (3.6). All the structure factors peak at $k_x = \pi$, but, unlike in the case of the fundamental representation, there is no singularity but a smooth maximum (see FIG. 3.4). This shows that the antiferromagnetic correlations revealed by the peak at $k_x = \pi$ are only short ranged, and that the correlations decay exponentially at long distance, in agreement with the presence of a gap, and with the spontaneous dimerisation.

To summarise, ED and VMC results clearly support Affleck's predictions that the $N/m = 2$ systems are gapped and point to a very strong spontaneous dimerisation in agreement with previous results by Paramakanti and Marston [40].

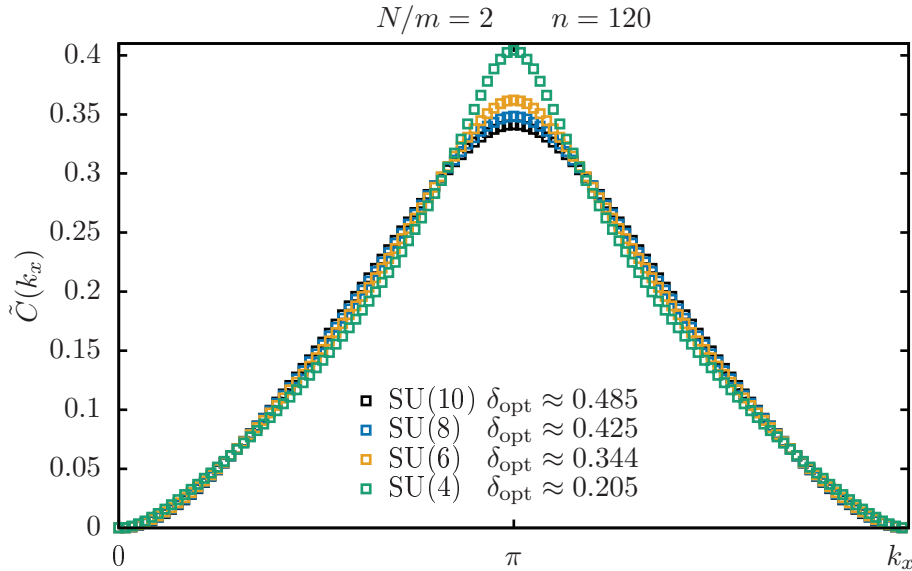


Figure 3.4 – Structure factor of various $SU(N)$ models with $m = N/2$ calculated with VMC with the optimal variational parameter δ_{opt} .

3.3.3 Relevant case: $SU(6)$ with $m = 2$

This case is a priori more challenging to study because the relevant operator that is generated in the renormalisation group theory appears at higher order than the one-loop approximation. Therefore, the gap can be expected to be significantly smaller than in the previous case. This trend is definitely confirmed by ED performed on clusters with up to 15 sites: the gap decreases quite steeply with the system size (see upper left panel of FIG. 3.5). It scales smoothly however, and a linear extrapolation points to a gap of the order $\Delta E \approx 0.2$, much smaller than in the $SU(6)$ case with $m = 3$ ($\Delta E \approx 4$), but finite. On the largest available cluster, the bond energy has a significant dependence on the bond position, with an alternation of two very negative bonds with a less negative one.

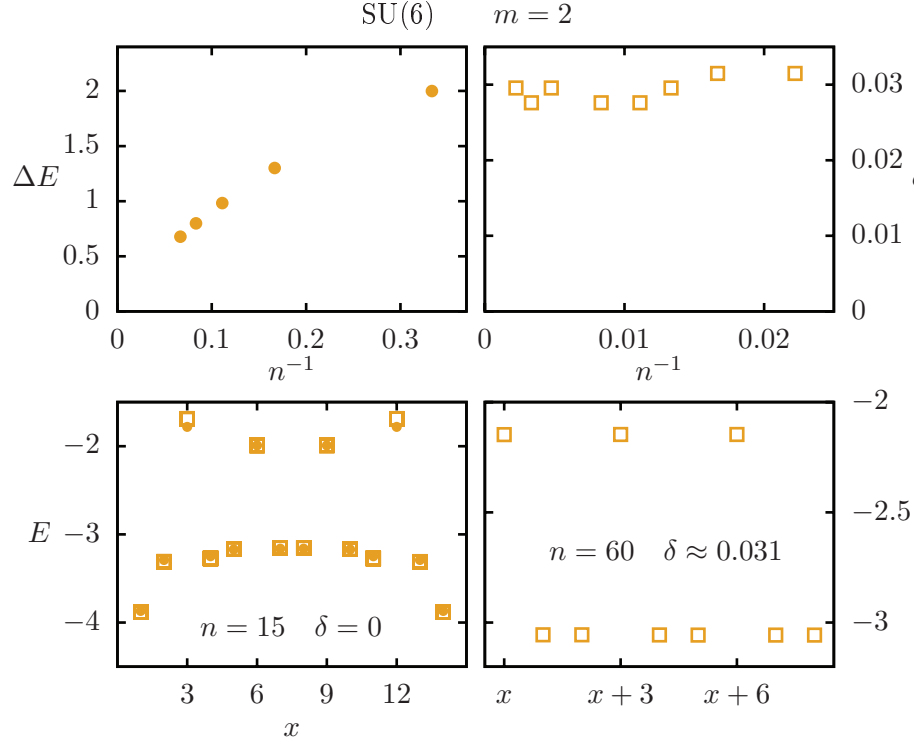


Figure 3.5 – ED and VMC results for the SU(6) model with $m = 2$. Upper left panel: size dependence of the energy gap. Upper right panel: optimal variational parameter δ for periodic boundary conditions. Lower left panel: energy per bond calculated with ED (circles) and VMC (squares) on 15 sites with open boundary conditions. Note that the optimal variational parameter $\delta = 0$ in that case. Lower right panel: energy per bond calculated with VMC with periodic boundary conditions.

These trends are confirmed and amplified by VMC. Indeed, the trimerised wave function $|\Psi_G^3(\delta)\rangle$ leads to a better energy for all sizes, and the optimal value scales very smoothly to a small but finite value $\delta_{\text{opt}} \approx 0.03$. This value is about an order of magnitude smaller than in the SU(6) case with $m = 3$, but the fact that it does not change with the size beyond 60 sites is a very strong indication that the system trimerises (by contrast to the marginal case shown in FIG. 3.9). The trimerisation is confirmed by the lower plots. For $n = 15$, the VMC results are again in nearly perfect agreement with ED, and for $n = 60$, the bond energy shows a very clear trimerisation.

To test the nature of the long-range correlations is of course more challenging than in the previous case since a small gap implies a long correlation length. And indeed, on small to intermediate sizes, the structure factor has a sharp peak at $k_x = 2\pi/3$ very similar to the SU(3), $m = 1$ case. However, going to very large system sizes (up to $n = 450$ sites), it is clear that the concavity changes sign upon approaching $k_x = 2\pi/3$ (see upper right panel of FIG. 3.6), consistent with a smooth peak, hence with exponentially decaying correlation functions (see also lower panel of FIG. 3.6).

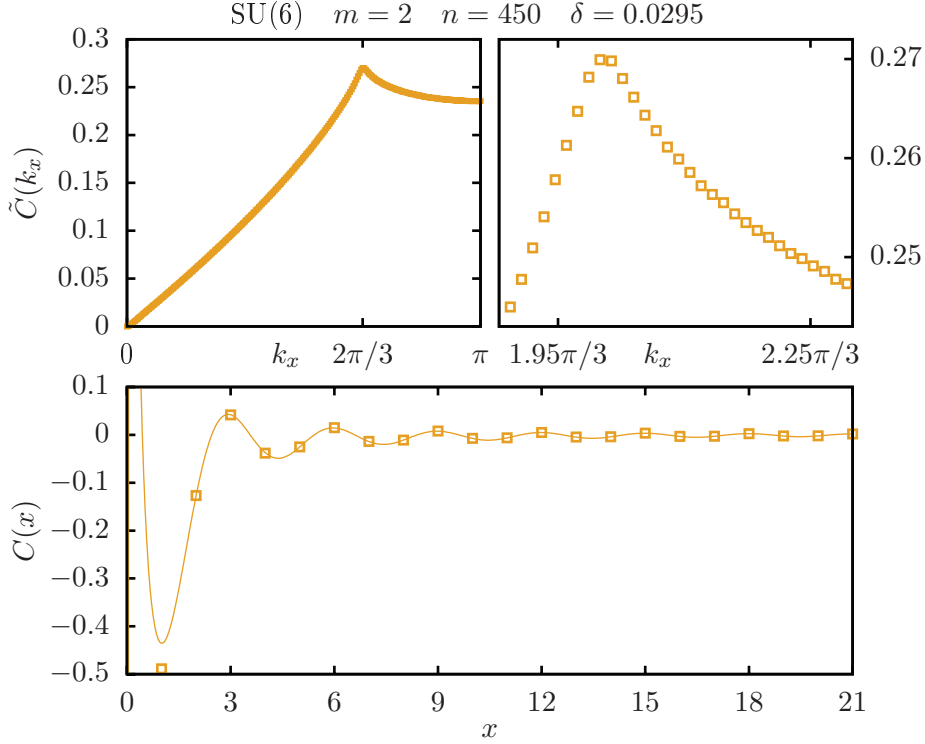


Figure 3.6 – Upper left panel: Structure factor of the SU(6) model with $m = 2$ calculated with VMC using a trimerised wave function with the optimal variational parameter. Upper right panel: zoom on the region near $k_x = 2\pi/3$. It clearly shows that the structure factor is smooth. Lower panel: real-space diagonal correlations for 60 sites.

In that case, in view of the small magnitude of the gap, hence of the very large value of the correlation length, it would be difficult to conclude that the system is definitely trimerised on the basis of ED only. In that respect, the VMC results are very useful. On small clusters, the Gutzwiller projected wave function with trimerisation is nearly exact, and VMC simulations on very large systems strongly support the presence of a trimerisation and of exponentially decaying correlations [71].

3.3.4 Marginal cases: SU(8) with $m = 2$ and SU(9) with $m = 3$

These two systems are the only ones which possess operators with scaling dimension $\chi = 2$. They are therefore the only cases where it is impossible to predict whether the system is algebraic or gapped on the basis of Affleck's analysis. As far as numerics is concerned, these cases can again be expected to require large system sizes to conclude.

The ED results are quite similar to the previous case. The scaling of the gap is less conclusive because the last three points build a curve that is still concave and not linear like in the previous case (see the upper right panel of FIG. 3.7). So one can only conclude that if there

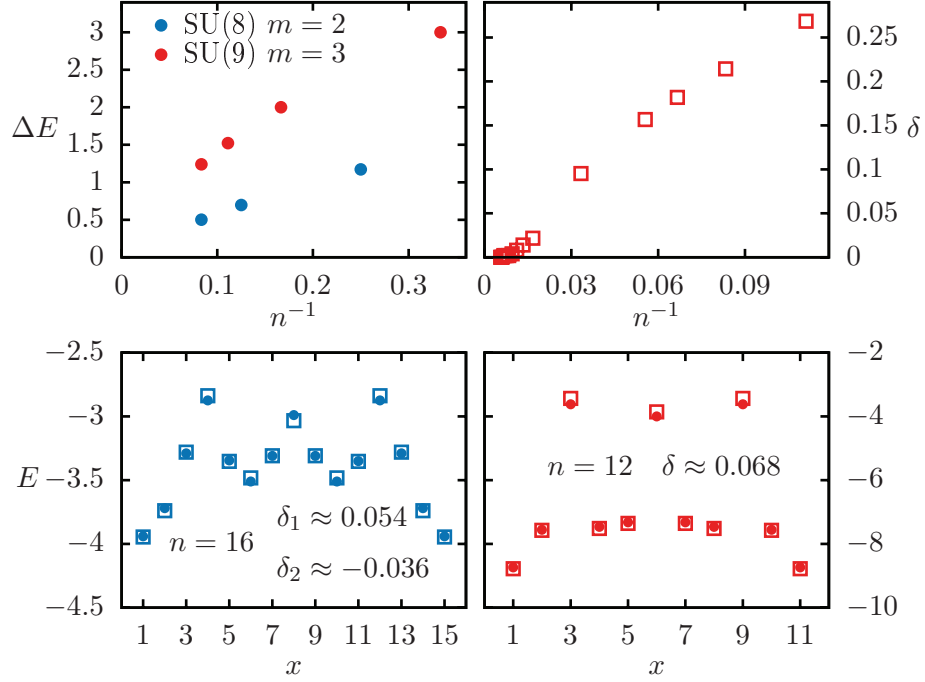


Figure 3.7 – ED and VMC results for the marginal cases SU(8) with $m = 2$ and SU(9) with $m = 3$. Upper left panel: size dependence of the energy gap for both cases. Upper right panel: optimal variational parameter δ for the SU(9) case with periodic boundary conditions. The results for SU(8) are not shown because they identically vanish for periodic boundary conditions. Lower left panel: energy per bond for SU(8) calculated with ED (circles) and VMC (squares) for open boundary conditions. Note that the optimal variational parameters δ_{opt} are different from zero with open boundary conditions. Lower right panel: energy per bond for SU(9) calculated with ED (circles) and VMC (squares) for open boundary conditions.

is a gap, it is very small, especially for SU(8) with $m = 2$. The bond energies build a pattern which is consistent with a weak tetramerisation for SU(8) with $m = 2$, and with a significant trimerisation comparable to the SU(6), $m = 2$ case for SU(9) $m = 3$.

The VMC method turns out to give a rather different picture however. For SU(8) with $m = 2$, two variational wave functions ($|\Psi_G^{\text{Fermi}}\rangle, |\Psi_G^4(\delta_1, \delta_2)\rangle$) can be tested. Interestingly, for $n = 16$ with open boundary conditions, $|\Psi_G^{\text{Fermi}}\rangle$ fails to reproduce the bound energies pattern observed with ED but $|\Psi_G^4(0.054, -0.036)\rangle$ is successful (see lower left panel of FIG. 3.7). This pattern, which could be interpreted as a weak tetramerisation, is in fact probably just a consequence of the four-fold periodicity of algebraic correlations in the presence of open boundary conditions. Indeed, it turns out that, for any system size with periodic boundary conditions, the minimisation of the energy using $|\Psi_G^4(\delta_1, \delta_2)\rangle$ failed to find a solution for any $|\delta_{1,2}| > 0.002$. Therefore $|\Psi_G^{\text{Fermi}}\rangle$ is believed to be the best variational wavefunction. The conclusion is that there is no tetramerisation, and that the correlations must be algebraic. This is also supported by the structure factor, which seems to have a singularity at $k_x = \pi/2$ (see FIG. 3.8).

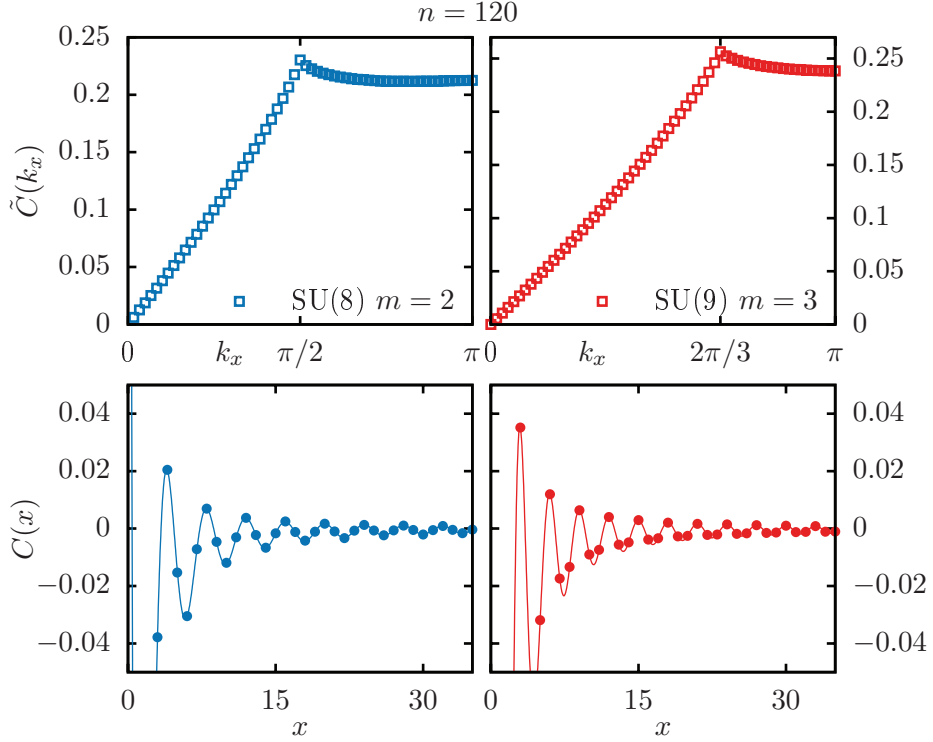


Figure 3.8 – Upper panels: Structure factor of the SU(8) model with $m = 2$ (left) and of the SU(9) model with $m = 3$ (right) calculated with VMC with periodic boundary conditions. Lower panels: real space correlations. The four plots represents results obtained with $|\Psi_G^{\text{Fermi}}\rangle$.

Let us now turn to SU(9) with $m = 3$. This system could in principle be trimerised, and therefore $|\Psi_G^{\text{Fermi}}\rangle$ and $|\Psi_G^3(\delta)\rangle$ have been compared. For small clusters, there is a large optimal value of δ , actually much larger than for SU(6) with $m = 2$, and the bond energies are typical of a strongly trimerised system, in agreement with ED. However, δ_{opt} decreases very fast with n until it vanishes for $n \gtrsim 100$ whereas, for SU(6) with $m = 2$, δ_{opt} levels off at a finite value beyond $n = 60$ (see FIG. 3.9). We interpret this behaviour as indicating the presence of a cross-over: on small length scales, the system is effectively trimerised, but this is only a short-range effect, and the system is in fact gapless with, at long-length scale, algebraic correlations.

One can again calculate the structure factor using the best variational wave function (in both cases $|\Psi_G^{\text{Fermi}}\rangle$ for big enough systems) to check if a discontinuity exists. The results displayed in the upper plots of FIG. 3.8 clearly show a discontinuity at $k_x = \pi/2$ for the SU(8) and at $k_x = 2\pi/3$ for SU(9). These discontinuities indicate an algebraic decay of the long-range correlations. The lower plot shows that even if these systems are gapless, there is a maxima of the correlation every N/m sites.

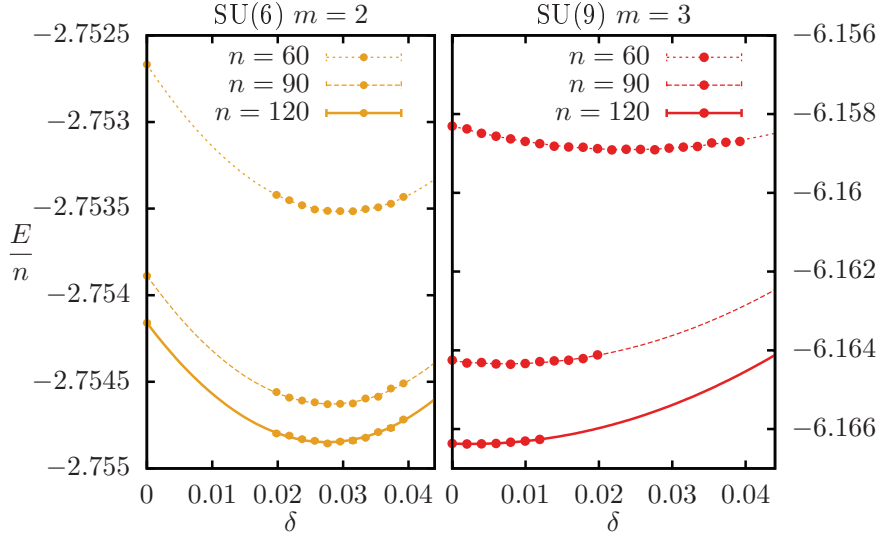


Figure 3.9 – Energy per site as a function of the variational parameter δ for the SU(6) with $m = 2$ (left) and SU(9) with $m = 3$ (right).

3.3.5 Irrelevant case: SU(10) with $m = 2$

For completeness, we have also looked at a case where there is an irrelevant operator of scaling dimension larger than 2, namely SU(10) with $m = 2$. As expected, the best variational wave function is $|\Psi_G^{\text{Fermi}}\rangle$ for all sizes, and the structure factor exhibits discontinuities at $k_x = 2\pi/5$, consistent with a gapless spectrum and algebraic correlations.

3.3.6 Critical exponents

Motivated by the remarkably accurate results obtained in previous works for the case the fundamental representation [23, 40], we have tried to use the VMC results to determine the critical exponent that controls the decay of the correlation function at long distance, (3.6). For the particular case of gapless systems, conformal field theory predicts an algebraic decay of the long-range correlations function according to:

$$C(x) = \frac{c_0}{x^2} + \frac{c_k \cos(2\pi x m / N)}{x^\eta} \quad (3.10)$$

where $\eta = 2 - 2/N$ is the critical exponent.

For systems with periodic boundary conditions, one can define two distances between two points, which naturally leads to the following fitting function [16]:

$$c_0 (x^{-\nu} + (n-x)^{-\nu}) + c_k \cos(2\pi x m / N) (x^{-\eta} + (n-x)^{-\eta}) \quad (3.11)$$

with four free parameters: c_0 , ν and c_k , η , the amplitudes and critical exponents of the components at $k_x = 0$ and $k_x = 2\pi m / N$ respectively.

There is a large degree of freedom in the choice of the fitting range. One could in principle select any arbitrary range of sites $[x_i, x_f]$, $0 \leq x_i < x_f \leq n-1$. The problem is that each range will give different critical exponents. In order to obtain some meaningful results the following method has been chosen. Using the periodicity of the systems, only the ranges with $x_i = a$ and $x_f = n - a - 1$, $1 \leq a \leq n/2$, have been considered. For each value of a , the coefficient of determination of the fit has been computed and if its value is higher than 0.999 then the range $[a, n - a - 1]$ is selected to perform the extrapolation of the critical exponents. If the value is too low, the fit is considered to be bad and the range with $a \leftarrow a + 1$ is tested. If no good range can be found with this criterion, the condition over the coefficient of determination is relaxed to be higher than 0.995 and the first fit with a residual sum of squares divided by n that is smaller than 10^{-7} is selected.

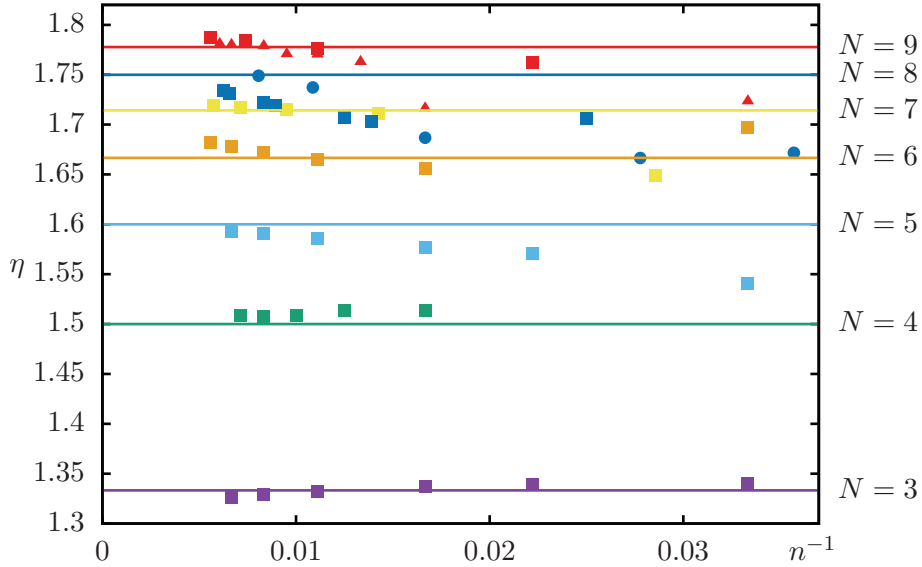


Figure 3.10 – Critical exponents η of the gapless systems as a function of the system size. The squares, circles and triangles correspond respectively to $m = 1, 2$, and 3 particles per site. All values given here have been calculated with $|\Psi_G^{\text{Fermi}}\rangle$.

The critical exponents η obtained in this way are shown in FIG. 3.10. The theoretical values of the critical exponents $\eta = 2 - 2/N$ are shown as straight lines. In all cases, the extracted exponents agree quite well with the theoretical predictions when n is large enough. In particular, for a given N , the exponent η does not depend on m , as predicted by non-abelian bosonisation. The critical exponents ν has also been extracted but, as already observed [16], a precise estimate is difficult to get. Nevertheless, for $N = 3, 4$, $\nu \in [1.8, 2.25]$ and for $N \geq 5$, $\nu \in [1.95, 2.05]$ for the largest systems.

3.4 Chapter summary

Using variational Monte Carlo based on Gutzwiller projected wave functions, we have explored the properties of $SU(N)$ Heisenberg chains with various totally antisymmetric irreps at each site. In the case of the fundamental representation, which is completely understood thanks to Bethe ansatz and to QMC simulations, these wave functions are remarkably accurate both regarding the energy and the long-range correlations. In the case of higher antisymmetric irreps, where field theory arguments are in most cases able to predict that the system should be gapless or gapped, allowing for a symmetry breaking term in the tight binding Hamiltonian used to define the unprojected wave function leads to results in perfect agreement with these predictions, and the ground state is found to be spontaneously dimerised or trimerised. Finally, in the two cases where the operator that could open a gap is marginal, $SU(8)$ with $m = 2$ and $SU(9)$ with $m = 3$, this variational approach predicts that there is no spontaneous symmetry breaking, and that correlations decay algebraically. These results suggest that the operators are marginally irrelevant in both cases. It would be interesting to test these predictions either analytically by pushing the renormalisation group calculations to higher order, or numerically with alternative approaches such as DMRG or QMC.

In any case, these results prove that Gutzwiller projected fermionic wave functions do a remarkably good job at capturing quantum fluctuations in one-dimensional $SU(N)$ Heisenberg models with totally antisymmetric irreps.

4 Ladder

In the previous chapter, we obtained very good results for a 1-dimensional system. We were able to confirm the nature of the ground state of the $SU(N)$ Heisenberg model on a chain for any fully antisymmetric irrep. The only gapped cases are for $k \equiv N/m = 2$ or $SU(6)$ $m = 2$. All other values of N and m lead to a critical ground state. It is therefore natural to wonder what will happen to those critical ground states when they undergo a small perturbation. This motivated us to study the behaviour of two chains coupled together forming a ladder. The following $SU(N)$ Heisenberg Hamiltonian describes this model and consists of two terms:

$$\hat{H} = \cos(\theta) \sum_{l=1}^2 \sum_i \hat{H}_{ii+1}^{ll} + \sin(\theta) \sum_i \hat{H}_{ii}^{12} \quad (4.1)$$

with

$$\hat{H}_{ij}^{ll'} = \sum_{\alpha\beta} \hat{c}_{(li)\alpha}^\dagger \hat{c}_{(li)\beta} \hat{c}_{(l'j)\beta}^\dagger \hat{c}_{(l'j)\alpha} \quad (4.2)$$

where the indices $l, l' = 1, 2$ stand for the legs of the ladder and $i, j = 1, \dots, n/2$ stand for the sites on each leg. The value of θ interpolates between the limit of decoupled chains, when $\theta = 0$, and decoupled rungs, when $\theta = \pi/2$. We will only study the values of θ within the range $\theta \in [0, \pi/2]$ because we want to keep the coupling terms positive.

The other motivation to study the $SU(N)$ ladder comes from a result on the $SU(4)$ case in the fundamental irrep. In reference [18], van den Bossche et al. have shown that for the isotropic coupling $\theta = \pi/4$, the ground state consists of 4-site plaquettes. A plaquette contains the smallest number of sites that is required to build a $SU(4)$ singlet. The authors have then proved in the strong coupling limit, $\theta \lesssim \pi/2$, that the ground state can be seen as the 6-dimensional irrep of $SU(4)$ on each rung. This state corresponds to a chain with two particles per site in the antisymmetric irrep. As we confirmed in section 3.3.2, this is a gapped state for which we observed dimerisation. In the other limit, $\theta \gtrsim 0$, they obtained the low-energy effective Hamiltonian starting from the fixed point Hamiltonian of two decoupled Wess-Zumino-Novikov-Witten (WZNW) $SU(1)_{k=1}$ models with central charge $c = 6$. They found two

operators, one of them being marginal and the other relevant. Moreover, the authors showed, thanks to abelian bosonisation, that all degrees of freedom are massive. This strongly suggests that the system is gapped in the weak coupling limit. Additionally, no phase transition is expected between the weak and strong coupling. These arguments have been generalised in a recent field theory study by Lecheminant and Tsvelik [19].

A generalisation of the Lieb-Schultz-Mattis (LSM) states that if m , the number of boxes contained in a Young tableau labelling an irrep of $SU(N)$, does not divide N , then the ground state is either gapless and non-degenerate or gapped and degenerate [72, 73]. In the strong coupling limit, the effective model of a $SU(N)$ ladder with $N = km$ and m particles per site is given by a chain for which each of the $n/2$ sites is in an irrep of $SU(N)$ labelled by a Young tableau with $\tilde{m} \equiv 2m$ boxes. When \tilde{m} does not divide N the LSM hypothesis are satisfied. As $\tilde{m}/N = 2m/km = 2/k$, we directly see that this theorem will be satisfied for $k > 2$.

The following section will present the variational wave functions used during this study of the $SU(N)$ Heisenberg model on the ladder. Then we will present our numerical results, starting with the case $k = 2$ and $m > 1$, where VMC results will show that the dimerised state, already known to be the ground state for $\theta = 0$, will survive in a large portion of the weak coupling regime. For the strong coupling regime, the ground state will also consist of dimers but instead of living on the legs, they are on the rungs and it is gapless. The case $k = 3$ will be investigated in the next section. When θ goes from 0 to $\pi/2$, the VMC optimal solution will select various states that will be introduced later. The last case of interest will be $k = 4$ for which we expect a plaquette ground state, when $m = 1$ and $\theta > 0$. We will see that the VMC confirms the presence of this ground state over a large range of θ and extends this result to $m = 2$.

4.1 Variational wave functions

As we are willing to study a large variety of $SU(N)$ models in various irreps, we need a variational wave function that can capture different states. The easiest way to achieve this is to use the PSO algorithm to proceed to a numerical optimisation of the general variational Hamiltonian (2.10). As we do not expect any kind of colour order, we can get rid of the on-site chemical potential, use the same variational Hamiltonian for all colours and drop the colour index. Moreover t_{ij} can be chosen real because having a flux per plaquette different than 0 or π would break the time reversal symmetry. With those assumptions the most general variational Hamiltonian, for a ladder with n sites divided into n/M rectangular unit cells containing M sites and indexed by their positions \mathbf{m} , is:

$$\hat{T} = \sum_{\mathbf{m}} \sum_{s=1}^{n/2M} \left(t_{vs} \hat{c}_{\mathbf{m}1s}^\dagger \hat{c}_{\mathbf{m}2s} + \sum_{l=1}^2 t_{ls} \hat{c}_{\mathbf{m}ls}^\dagger \hat{c}_{\mathbf{m}l{s+1}} + \text{h.c.} \right) \quad (4.3)$$

where $t_{vs}, t_{ls} \in \mathbb{R}$ are the variational parameters. In practice, one parameter is fixed to $t = 1$ to set a reference. Therefore, there are $3M/2 - 1$ free variational parameters for a given unit cell with M sites. To make sure that we have a representative set of variational wave functions

able to capture various types of symmetry breaking, we run the PSO algorithm for $M = 2, 4, 6, 8$ when $k = 2$, for $M = 6$ when $k = 3$ and $M = 4, 8$ when $k = 4$. All results that will be shown were obtained for a 72-site ladder with PBC, but simulations for $n = 24, 48$ produced similar results. On average more than 20000 different variational parameters have been measured during each simulation.

4.2 Correlation functions and structure factors

To better analyse the variational solutions, the long range correlations and structure factors have been computed. For a ladder, the relevant long range correlations are defined by:

$$C^\pm(x) \equiv \sum_a \langle (\hat{S}_{a\alpha}^{10} \pm \hat{S}_{a\alpha}^{20}) (\hat{S}_{a\alpha}^{1x} \pm \hat{S}_{a\alpha}^{2x}) \rangle \quad (4.4)$$

$$= \sum_a \langle \hat{S}_{a\alpha}^{10} \hat{S}_{a\alpha}^{1x} \rangle + \langle \hat{S}_{a\alpha}^{20} \hat{S}_{a\alpha}^{2x} \rangle \pm \langle \hat{S}_{a\alpha}^{10} \hat{S}_{a\alpha}^{2x} \rangle \pm \langle \hat{S}_{a\alpha}^{20} \hat{S}_{a\alpha}^{1x} \rangle \quad (4.5)$$

$$\equiv C^{ll}(x) \pm C^{ll'}(x) \quad (4.6)$$

where in the second line each term is given by (3.5). In the last equation, no sum over l or l' is required because those two terms simply refer to the intra- and inter-leg long range correlations. These definitions induce the following structure factors:

$$\tilde{C}^\pm(k_x) = c_\pm \sum_x C^\pm(x) e^{ik_x x} \quad (4.7)$$

$$\tilde{C}^{ll'}(k_x) = c_{ll'} \sum_x C^{ll'}(x) e^{ik_x x} \quad (4.8)$$

$$\tilde{C}^{ll}(k_x) = \frac{1}{2\pi} \frac{N}{m(N-m)} \sum_x C^{ll}(x) e^{ik_x x} \quad (4.9)$$

where the normalisation constants $c_\pm, c_{ll'}$ depend on the system and are fixed to agree with the normalisation of the intra-leg structure factor (4.9):

$$\sum_{k_x} \tilde{C}^\pm(k_x) = \sum_{k_x} \tilde{C}^{ll'}(k_x) = \sum_{k_x} \tilde{C}^{ll}(k_x) = \frac{n}{2\pi} \quad (4.10)$$

One should keep in mind that the normalisation enforces $\sum_{k_x} \tilde{C}^\pm(k_x) > 0$ and $\sum_{k_x} \tilde{C}^{ll'}(k_x) > 0$. Therefore, for all the results that will be presented, the constants are such that $c_\pm > 0$ and $c_{ll'} < 0$.

In the following, we will use the four structure factors to describe the variational solutions. To make sense of the results, it is important to introduce the ratio:

$$r = \frac{C^{ll}(0)}{C^{ll'}(0)} = \frac{2m(N-m)}{NC^{ll'}(0)} \quad (4.11)$$

which gives the proportionality factor entering:

$$\tilde{C}^{\pm}(k_x) \propto r \tilde{C}^{ll}(k_x) \pm \tilde{C}^{ll'}(k_x) \quad (4.12)$$

Typically, when the legs are decoupled, we expect r to be very large so that the contribution of $\tilde{C}^{ll'}(k_x)$ is irrelevant. Finally, the structure factors (4.7) can also be understood as $\tilde{C}(k_x, k_y)$ for $k_y = 0$ or $k_y = \pi$, more precisely:

$$\tilde{C}(k_x, 0) = \tilde{C}^{+}(k_x) \quad \tilde{C}(k_x, \pi) = \tilde{C}^{-}(k_x) \quad (4.13)$$

4.3 Results

We will use the wave functions introduced in the previous section to first study the $k = 2$ case. The second part will tackle the $k = 3$ case, while the last will concern $k = 4$.

4.3.1 $k = 2$

This case is certainly the easiest to start with because the ground state can be predicted in both the weak and strong coupling limits. Indeed, from the previous chapter, it is known that the chains are gapped if they are independent and $N > 2$. The focus will therefore only be put on $m = 2, 3, 4$. In the other limit, the system will consist of a singlet on each rung because the effective model can be described by a chain with $\tilde{m} = 2m = N$ particles per site in the antisymmetric irrep. As the number of boxes \tilde{m} on each site can be divided by N , this case does not enter the generalised LSM theorem and a non-degenerate gapped ground state is allowed.

The figure FIG. 4.1 summarises the essential results. We can see on the left that the bond energy patterns of the optimal solutions for $\theta = 0.1$ consists in facing strong negative bonds on each chain. As all other bonds are weaker, this state is built of dimers. Moreover the inter-leg bond energy is weaker than the one between dimers along each chain. It is also relevant to notice that the larger m is, the smaller the energy of the inter-leg bonds becomes. Despite being substantially different, the optimal variational parameters create the same bond energy pattern for all m . The solutions shown here are the optimal ones for each m , but the PSO algorithm found many other solutions with competitive energy. Interestingly, all of them create the same type of bond energy pattern. This state remains the optimal solution over a large range of θ . For instance, as shown on the right of FIG. 4.1, this type of solution is optimal for $\theta \in [0.1, 0.6]$ for all m . It may even extend further than $\theta = 0.7$ for $m = 3, 4$ but as other types of solutions start to have competing energies, it would not be safe to assume anything on the nature of the ground state based on these variational wave functions. We are indeed close to the point, where the inter- and intra-leg couplings become equal. This is certainly why for $m = 2$ and $\theta = 0.7$, the bond energy pattern of the optimal solution is relatively homogeneous, as shown in the central left picture of FIG. 4.1. The small difference in the energy of the bonds

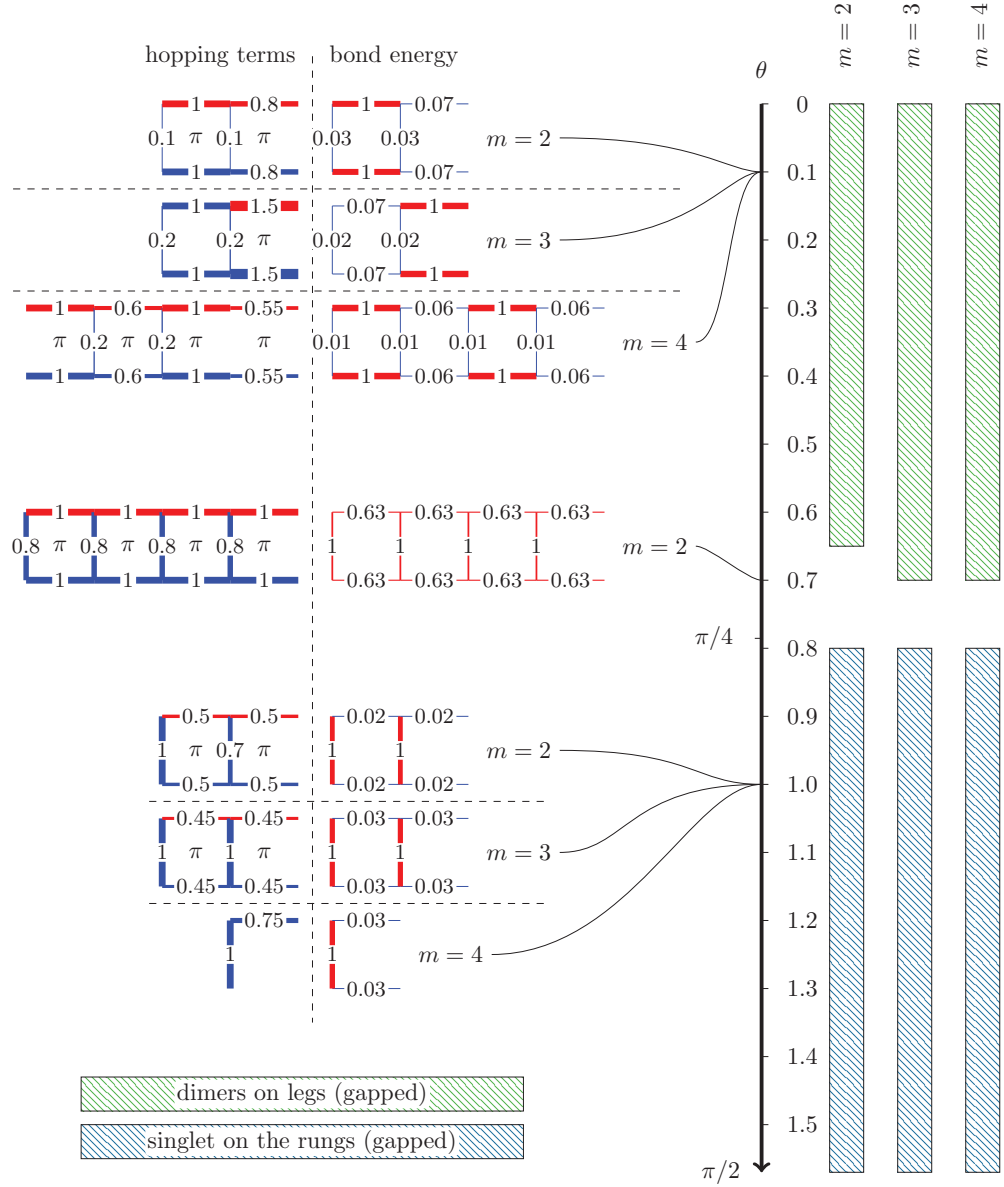


Figure 4.1 – Variational results obtained on a 72-site ladder with periodic boundary condition for $k = 2$ and $m = 2, 3, 4$. The vertical axis shows the different values of θ , going from decoupled chain, $\theta = 0$, to decoupled rungs, $\theta = \pi/2$. The isotropic coupling point is shown at $\theta = \pi/4$. The optimal solutions are displayed on the left of this axis at particular θ and m . For each solution, the left unit cell represents the optimal variational parameters (with the eventual π -flux), while the right one shows the measured bond energies. The width of each link and its associated number represent the absolute value of the hopping term or bond energy. It is coloured in red if its value is negative and in blue if positive. The right part of the plot qualitatively represents the type of ground state as a function of the coupling strength θ .

suggests that, at this point, the system already favours a dimerisation on the rungs, but the VMC is inconclusive.

For larger values of the coupling, $\theta \geq 0.8$, the optimal solutions create a bond energy pattern with stronger bond on the rungs. This agrees very well with the strong coupling picture of interacting singlets present on each rung. As the lower pictures of FIG. 4.1 shows, solutions of completely different nature produce a very competitive variational energy because the expected bond energy pattern is very easy to achieve and can be realised in many ways.

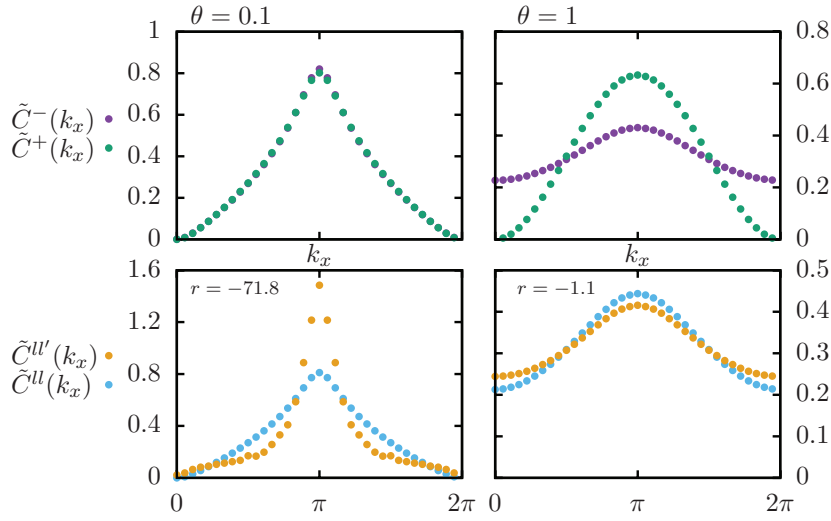


Figure 4.2 – Structure factor for SU(4) $m = 2$ obtained for a ladder with 72-sites and periodic boundary condition. The results for $\theta = 0.1$ and $\theta = 1$ are shown respectively on the left and the right. The upper panels displays $\tilde{C}^{\pm}(k_x)$ while the lower ones illustrate $\tilde{C}^{ll}(k_x)$ and $\tilde{C}^{ll'}(k_x)$. The indicated value r corresponds to the ratio (4.11). The upper plots can be obtained by summing the data of the lower plots according to (4.12).

To have a better understanding of the properties of these variational states, the structure factors have been computed for the two types of solutions found in this analysis. We show in FIG. 4.2 what the structure factors (4.7), (4.8) and (4.9) look like for the $m = 2$ case because they present the same features for any m . The upper panels display the structure factors $\tilde{C}^{\pm}(k_x)$. The left one agrees with a gapped and dimerised state because the structure factors are smooth and present a maxima at π , while the right one present an interesting feature for $\tilde{C}^{-}(0) = \tilde{C}^{-}(0, \pi) \neq 0$. This indicates that two opposite sites on the ladder will not share the same colour. This is most easily explained by explicitly computing this term in the strong coupling limit, where the system is effectively described by $n/2$ independent sites in the fully antisymmetric irrep of SU(4). Which means that the correlations can be computed only by considering the sites (l s) and (l' s). If the site (l s) is occupied by the state $|AB\rangle - |BA\rangle$, on the opposite site of the ladder, *i.e.* (l' s), the state will be $|CD\rangle - |DC\rangle$. This implies that the

correlations at distance $x = 0$ will be given by:

$$C^{ll}(0) = \sum_{\alpha} \langle \hat{S}_{\alpha\alpha}^{10} \hat{S}_{\alpha\alpha}^{10} \rangle + \langle \hat{S}_{\alpha\alpha}^{20} \hat{S}_{\alpha\alpha}^{20} \rangle = 2 \frac{m(N-m)}{N} = 2 \quad (4.14)$$

$$C^{ll'}(0) = \sum_{\alpha} \langle \hat{S}_{\alpha\alpha}^{10} \hat{S}_{\alpha\alpha}^{20} \rangle + \langle \hat{S}_{\alpha\alpha}^{20} \hat{S}_{\alpha\alpha}^{10} \rangle = -2 \frac{m^2}{N} = -2 \quad (4.15)$$

which gives $r = -1$. As all other correlations will be zero, because in this strong coupling limit the $n/2$ sites are independent, these long range correlations behave like $\delta(x)$ for which we have that $\tilde{C}^{ll}(k_x) = \tilde{C}^{ll'}(k_x) = 1/\pi$. Thanks to (4.12) the following relation is obtained:

$$\tilde{C}^{\pm}(k_x) \propto \frac{r}{\pi} \pm \frac{1}{\pi} = \frac{1}{\pi} (1 \mp 1) \quad (4.16)$$

This shows that in the strong coupling limit, $\tilde{C}^{+}(k_x) = 0$ and $\tilde{C}^{-}(k_x) = 1/\pi$. Of course any coupling between the rungs will influence these results. This is why the upper right plot of FIG. 4.2 is not trivial. Indeed, as $r = -1.1$, the small differences between $\tilde{C}^{ll}(k_x)$ and $\tilde{C}^{ll'}(k_x)$ shown in the lower right plot, have a large impact. As a counter example, one can look at the lower left plot, where the large difference between $\tilde{C}^{ll}(k_x)$ and $\tilde{C}^{ll'}(k_x)$ around $k_x = \pi$ does not affect $\tilde{C}^{\pm}(k_x)$ much because r is large. Overall, all structure factors shown in FIG. 4.2 agree with gapped phases which correspond to a doubly degenerate dimerised state in the weak coupling limit and to a gapped singlet state in the strong coupling limit.

We have shown that for $k = 2$, the PSO algorithm finds two types of solutions, both of them agreeing with theoretical predictions on the nature of the ground state. The transition between the weak coupling solution (dimerisation on the legs) to the large coupling solution (singlet on the rungs) seems to occur at the isotropic coupling. We did not attempt to precisely locate this transition because the goal of the minimisation was to find different variational solutions. As two ground states and related variational wave functions have been identified, it would be possible to measure with more accuracy the transition by simply comparing their variational optimal energies for more values of θ .

4.3.2 $k = 3$

We will now analyse the results obtained by the PSO algorithm for the $k = 3$ case for $m = 1, 2, 3$. As opposed to the $k = 2$ case, a different behaviour is expected for each different m . Indeed, the legs already behave differently for $m = 1, 2, 3$, when they are decoupled. As shown in the previous chapter the chain is critical for SU(3) $m = 1$, gapped due to a relevant operator for SU(6) $m = 2$ and critical even in the presence of a marginal operator for SU(9) $m = 3$. The weak coupling regime might therefore exhibit different properties as a function of m for $k = 3$. The weak and strong coupling regimes should give similar results because they are connected by the relations discussed in 1.2.1.3:

$$m = l \quad \tilde{m} = N - l = 3m - l = 2m \quad (4.17)$$

Indeed, a ladder for $SU(3m)$ with m particles per site in the strong coupling regime corresponds to a chain for $SU(3m)$ with $\tilde{m} \equiv 2m$ particles per site.

For clarity, we will first present the four different types of optimal solutions found by the PSO algorithm, then discuss the variational results for each m independently. The simplest type of solution that will appear is non-degenerate, gapless and consists of two critical chains coupled together by weak links. The other gapless state consists of translationally invariant strong dimers on the rungs. The PSO algorithm has also found three gapped solutions. The first solution is a 6-site rectangular plaquette state with a $0\pi\pi$ flux pattern and is three times degenerate. The other two create a trimerisation on each chain with a π -flux in each square plaquette. For one solution, the trimerisation occurs on facing sites preserving the mirror symmetry perpendicular to the rungs, while for the other, the trimerisation on one leg is shifted by one site with respect to the other leg and breaks the mirror symmetry. Note that as the plaquette solution preserves the same symmetry as the mirror symmetric trimerised one, they produce the same physical state.

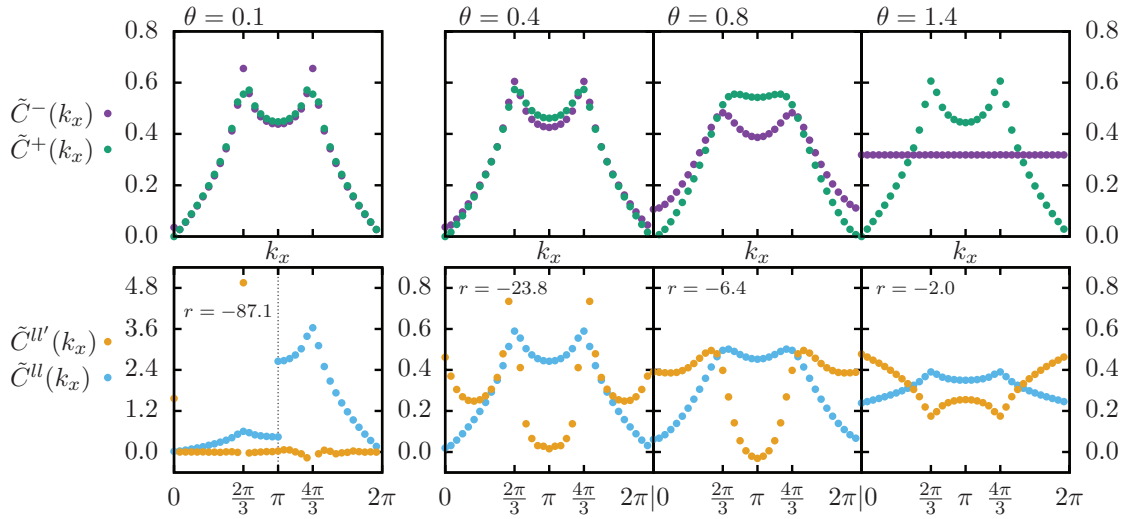


Figure 4.3 – Structure factor for $SU(3)$ $m = 1$ obtained for a 72-site ladder with periodic boundary condition. Each column represents a different value of θ , the upper plots display $\tilde{C}^{\pm}(k_x)$, while the lower ones display $\tilde{C}^{ll}(k_x)$ and $\tilde{C}^{ll'}(k_x)$. The relation (4.12) connects the upper and lower plots.

The plots on FIG. 4.3 display the structure factors for the four typical variational solutions, when $m = 1$. They help to characterise more precisely the different solutions. The structure factors for the gapless wave function, when $\theta = 0.1$, are shown on the left. The term $\tilde{C}^{+}(k_x)$ is clearly discontinuous at $k_x = \pi \pm \pi/3$. As for this solution, the legs are almost decoupled, the term $\tilde{C}^{ll'}(k_x)$ is peculiar. To better see its behaviour, it is plotted on two different scales in the lower left graph. It is almost vanishing for all k_x but not for $k_x = 0, \pi \pm \pi/3$. Even if the two legs are almost independent, they share the same long range correlation pattern, $C^{ll}(x)$. Its related structure factor is also shown on the same plot and exhibits a peak at $k_x = \pi \pm \pi/3$. Due to the small inter-leg coupling, the probability that two sites on different legs separated by $x = 3$ share

the same colour is higher which explains the singularities of $\tilde{C}^{II'}(k_x)$. Nevertheless, as r is large, the contribution of this term in $\tilde{C}^\pm(k_x)$ is small. For $\theta = 0.4$, *i.e.* for the second column in FIG. 4.3, one might wonder whether the structure factors $\tilde{C}^\pm(k_x)$ for $\theta = 0.4$ have a singularity or not. Running simulations for the same variational parameters on larger systems confirms that it is smooth. The maxima at $k_x = \pi \pm \pi/3$ agrees well with a trimerised state. For $\theta = 0.8$, the structure factors of the 6-site plaquette solution shown on the top of the third column of FIG. 4.3 are smooth. Note that the structure factors for the different optimal solutions at $\theta = 0.4$ and $\theta = 0.8$ present the same features. This indicates that there is a crossover between two variational solutions creating the same physical state. Finally, the right plot of FIG. 4.3 represents the results for $\theta = 1.4$. As expected, $\tilde{C}^+(k_x)$ has singularities at $k_x = \pi \pm \pi/3$ which is the correct behaviour of SU(3) chains with $\tilde{m} = 2$ particles per site.

The right part of FIG. 4.4 shows type of ground states in function of θ and m . For SU(3) $m = 1$, in the weak coupling regime, the best variational solution is the one with independent critical chains. By increasing the coupling, the translational symmetry is broken and gap opens in the spectrum. The optimal variational solution is first the trimerised state, then the plaquette one. In the strong coupling limit, the other gapless state, *i.e.* with a dimerisation on the rungs, becomes optimal. The VMC successfully recovers analogue states in the two opposite limits.

The optimisation algorithm gives interesting results for SU(6) $m = 2$. In the absence of inter-leg coupling, each chain is gapped. By weakly coupling the chains together, the nature of the ground state should not change. This is what confirms the PSO algorithm. For small values of θ , the optimal solution is trimerised. This state is robust and a transition to the other variational solution, *i.e.* the plaquette one, appears before the isotropic coupling point. This crossover from one type of variational wave function to the other can be seen on the left part of FIG. 4.4. In the strong coupling limit, the optimal solution is the gapless state with a dimerisation on the rungs. We see that in that case, the two limits do not agree. In the weak coupling limit the ground state is gapped, while in the strong coupling limit, it is gapless. This problem is certainly due to the difficulty already present for the SU(6) $m = 2$ chain. Indeed, very large systems and very weak trimerisation parameter were required to confirm the presence of a gap. The PSO algorithm is expected to be able to find this gapped state with longer and more precise simulations on bigger ladders.

For SU(9) $m = 3$, the ground state consists of two decoupled critical chains when $\theta = 0$ because the marginal operators do not open a gap. Nevertheless, for weak coupling the optimal variational wave function is trimerised. This is a realistic possibility because a gap may only open for finite θ . Note that the symmetry breaking induced by this trimerisation is not equivalent to the symmetry breaking induced by the plaquette wave function because the trimerisation pattern does not preserve the mirror symmetry. Then, the right part of FIG. 4.4 shows that the optimal solution becomes gapless when θ increases. A gapped plaquette state is favoured around the isotropic coupling point. Finally the other gapless solution consisting of dimers on the rungs is present for a large coupling. This large coupling solution agrees with the case of decoupled chains, as it should.

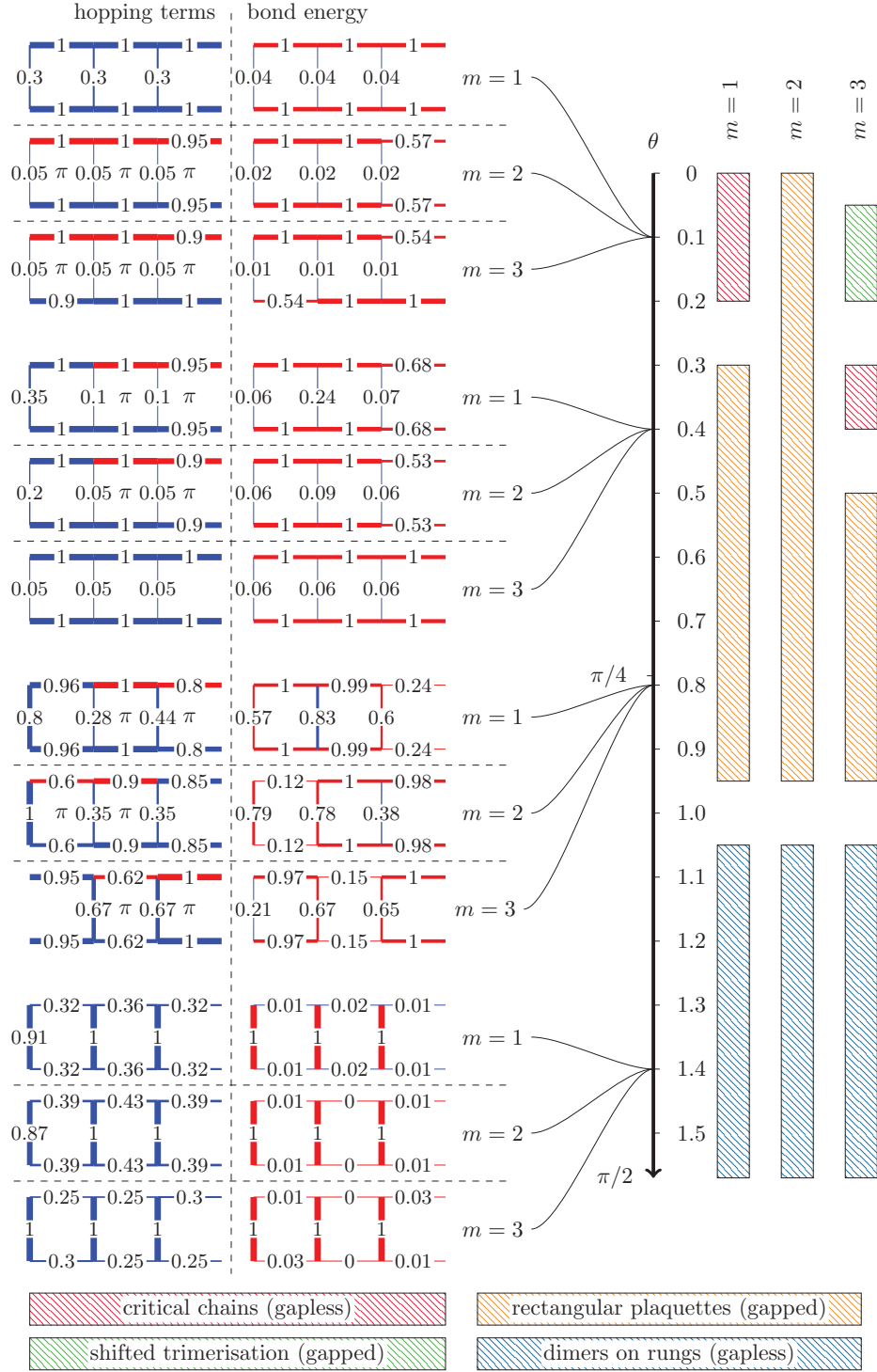


Figure 4.4 – Variational results obtained on a 72-site ladder with periodic boundary condition for $k = 3$ and $m = 1, 2, 3$. The conventions are identical to FIG. 4.1. As it can be seen on the left pictures, the optimal variational solution for $\theta = 0.1$ is different for $m = 1$ than for $m = 2, 3$, likewise for $\theta = 0.4$ the optimal solution for $m = 3$ is different than for $m = 1, 2$. All solutions for $\theta = 0.8$ are similar even if the unit cells are horizontally shifted.

Overall, as before, now that the optimal variational wave functions have been found, it would be possible to determine the value of θ for which the transitions between the optimal solutions occur. Nevertheless, as the PSO failed to find a gapped solution for SU(6) $m = 2$ in the large coupling limit, we may wonder whether the measured gapless regime for $\theta > 1$ and any m should not be smaller. The obvious idea to check this would be to run longer and more precise simulations. But it is difficult to find good variational wave functions when a strong dimerisation is expected because the VMC fails to initialise, especially for large m (see appendix B.3). Finally, it seems that for an equal coupling along the legs and rungs, the optimal solution consists in a 6-site plaquette phase for all m .

4.3.3 $k = 4$

When the chains are decoupled, Affleck's predictions and VMC results on the chain demonstrate that the ground state is critical. The nature of the ground state when $\theta \neq 0$ is difficult to determine, but some theoretical studies predict a plaquette phase for SU(4) $m = 1$ [18]. This instability is in competition with a possible tetramerisation on each chain [19].

We present in FIG. 4.5 a summary of the results obtained on a 72-site ladder with periodic boundary condition. In the weak coupling limit, the optimal variational wave function generates a gapless state. For a slightly larger coupling, the optimal variational solution creates the expected 4-site plaquette state. Interestingly, this solution has a π -flux between the plaquettes. At very large coupling, the optimal variational wave function does not involve any flux but a strong dimerisation on the rungs is present. One should not be confused, this variational solution is very different than the one observed at large coupling for $k = 2, 3$. Indeed, this state breaks the translational symmetry by weakly coupling two dimers together and is two times degenerate. It produces the same type of state as the plaquette variational solution. The identical symmetry breaking of these two variational wave functions can be confirmed by looking at the bond energy pattern of the solutions at $\theta = 0.8$ and $\theta = 1.4$ shown on the left of FIG. 4.5.

The structure factors displayed in FIG. 4.6 prove that two but not three distinct physical states were actually found. The first one, for small coupling, does not break any symmetry and is gapless, as indicated by the discontinuity at $k_x = \pi/2, \pi, 3\pi/2$ in the upper left plot. The other state breaks the translational symmetry by building 4-site plaquettes and even if the variational wave functions for $\theta = 0.8$ and $\theta = 1.4$ are different, they generate the same physical state. Indeed, the structure factors present the same features and no discontinuity in $\tilde{C}^\pm(k_x)$ which confirms that the two cases are gapped. As before, the lower plots show the individual contributions of $\tilde{C}^{II}(k_x)$ and $\tilde{C}^{II'}(k_x)$.

In summary, the PSO algorithm has found two distinct solutions for the SU(4 m) ladder. One gapless state in the weak coupling regime and a 4-site plaquette state in the strong coupling regime. A crossover between two different gapped variational solutions is observed, both of them producing the same physical state. In particular, the SU(4) $m = 1$ results partially agree

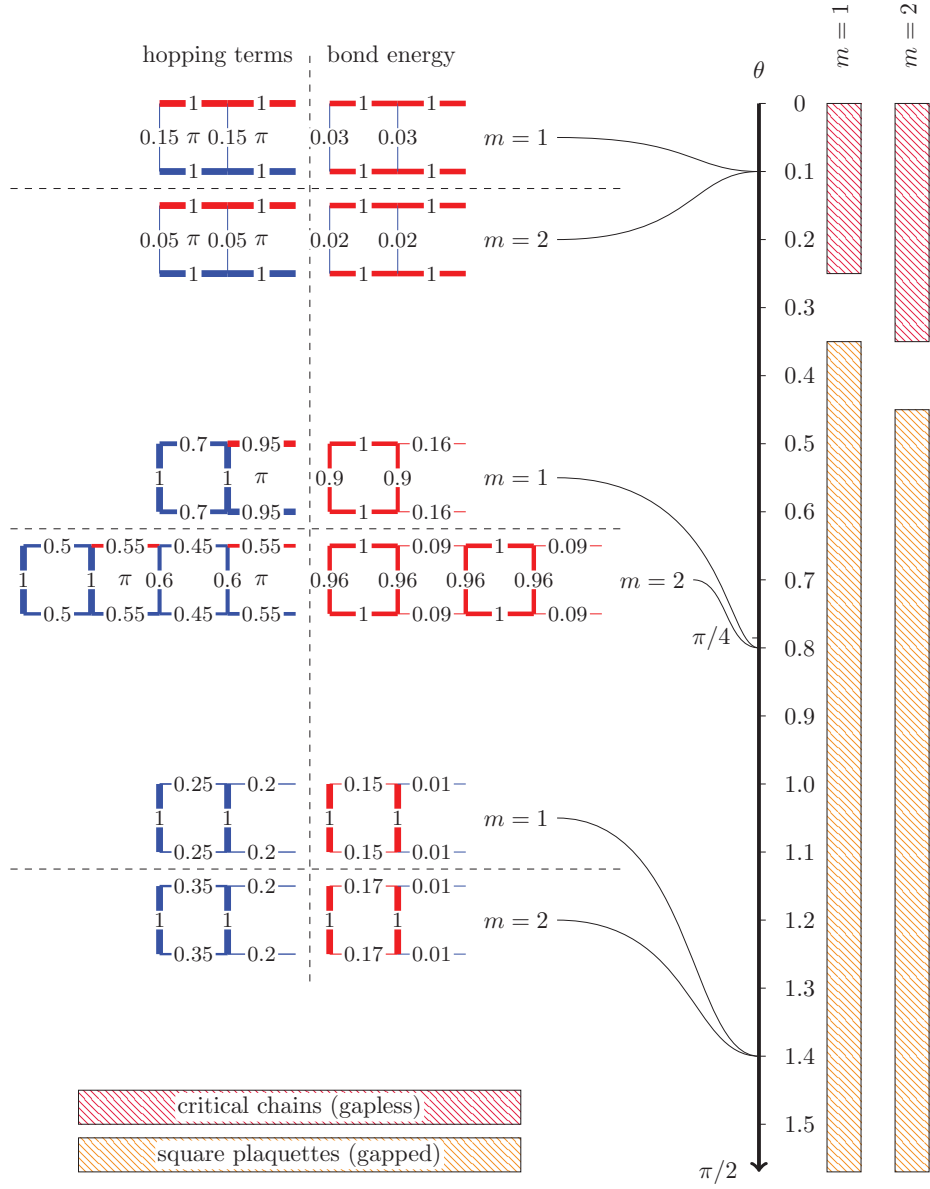


Figure 4.5 – Variational results obtained on a 72-site ladder with periodic boundary condition for $k = 4$ and $m = 1, 2$. The conventions are identical to FIG. 4.1. Note that the bond energy patterns of the solutions shown at $\theta = 1.4$ agree with the 4-site plaquette state displayed at $\theta = 0.8$.

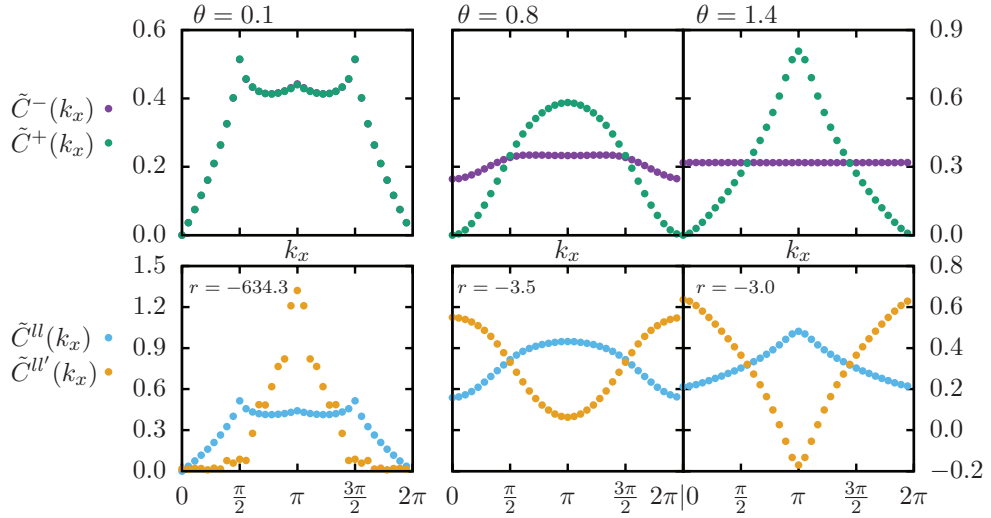


Figure 4.6 – Structure factor for SU(4) $m = 1$. The different values of θ are given in different columns. The upper and lower plots respectively show the structure factor for $\tilde{C}^{\pm}(k_x)$ and for $\tilde{C}^{ll}(k_x)$, $\tilde{C}^{ll'}(k_x)$.

with theory even if unpublished results by Weichselbaum show that the plaquette phase is stabilised as soon as $\theta > 0$. We have put a lot of effort to find a gapped state at $\theta = 0.1$. More than 160 000 different variational parameter sets have been tested on a single system, but no variational wave function was able to detect a gap. Even by diagonalising the overlap matrix and Hamiltonian in a variational subspace built by a set of variational wave functions [74, 75, 26], no significant energy gain was observed for the gapped wave functions.

4.4 Chapter summary

In this chapter, many results obtained using the VMC algorithm in conjunction with the PSO algorithm have been presented. The solutions found for the weak and strong coupling limits agree with theory for the $k = 2$ case. For the more complicated $k = 3$ case, four different types of variational wave functions were identified. For these systems, the weak and strong coupling limits should be equivalent because the fully antisymmetric irrep of SU($3m$) with m boxes is the conjugate equivalent of the irrep with $2m$ boxes in one column. In the strong coupling limit, even if the gapless state expected for $m = 1, 3$ was found, the results for the $m = 2$ case do not reproduce the expected gapped state due to the limitation of the VMC. For $k = 4$, despite extensive efforts, the presence of the 4-site square plaquette state could not be observed with VMC for $\theta < 0.4$. Nevertheless, it provides another confirmation that this is the ground state of the SU(4) $m = 1$ isotropic ladder and suggest that this remains true for SU(8) $m = 2$.

Two dimensional systems **Part III**

5 Square lattice

We will now focus our interest on the $SU(N)$ Heisenberg model on the square lattice. Studies for the fundamental irrep have been performed using for instance LFWT, iPEPS or ED [30, 31, 32] and a more general approach to study this model in various irreps is to use a mean-field theory [41, 42] like to one presented in 1.2.2. In this limit, a full analysis of the phase diagram of the $SU(N)$ Heisenberg model for fully antisymmetric irreps has been performed [43, 44] and two types of ground states have been predicted. The first type of ground state consists of plaquettes and hence breaks the lattice symmetry. This state, named valence cluster state for reasons that will become clear later, is the ground state of the mean-field model for $3 \leq k < 5$ with $k \equiv N/m$. The other state does not break any lattice symmetry but breaks the time reversal symmetry, it is a chiral state, and it is the mean-field ground state for $k \geq 5$.

As this mean-field study constitutes the starting point for our numerical simulations, the first part of this chapter will be dedicated to present and compute the mean-field energy of the ground states for $3 \leq k \leq 6$. We will then present the variational wave functions expected to reproduce those states in the mean-field limit.

An extensive use of VMC will provide new and interesting results. In particular the $SU(3m)$ and $SU(6m)$ cases have thoroughly been studied. We will provide strong indications that the mean-field solution is essentially correct for all $m \neq 1$. Additional attention will be given to the $SU(3)$, $SU(4)$ and $SU(5)$ for $m = 1$ because the ground state should exhibit some kind of order.

5.1 Mean-field approach

Hermele, Gurarie, and Rey [43] showed that on the square lattice the mean-field ground state is a valence cluster state (VCS) for $3 \leq k < 5$ and is a chiral state with a flux of $2\pi/k$ per square plaquette for $k \geq 5$. In this introductory part, the goal is to present those two states and compare their energies at the mean-field level for $3 \leq k \leq 6$.

Thanks to a Hubbard-Stratonovich transformation the $SU(N)$ Heisenberg Hamiltonian (1.45), which is quartic in fermionic operators, can be transformed into the quadratic mean-field

Hamiltonian with decoupled colours (1.91):

$$\hat{H}_{\text{MFS}}^\alpha = \sum_{\langle i,j \rangle} \left(\chi_{ij} \hat{c}_i^\dagger \hat{c}_j + \chi_{ij}^* \hat{c}_j^\dagger \hat{c}_i \right) + \epsilon_0 \quad (5.1)$$

with:

$$\epsilon_0 = \sum_{\langle i,j \rangle} \frac{|\chi_{ij}|^2}{JN} \quad (5.2)$$

This Hamiltonian is valid in the large- N limit, where the saddle point approximation becomes exact and for which the following constraints are satisfied:

$$\chi_{ij} = -JN \langle \hat{c}_i^\dagger \hat{c}_j \rangle \quad m = N \langle \hat{c}_i^\dagger \hat{c}_i \rangle \quad (5.3)$$

5.1.1 Chiral State

We will use some properties of the chiral states to find a set of χ_{ij} that creates an appropriate homogeneous flux per square plaquette. This will allow us to compute the energy of a simple state built with that particular choice of χ_{ij} .

5.1.1.1 Optimal flux

One of the many properties of a chiral state [76] is that for each colour the bands are either fully filled or fully empty. As we are dealing with N colours and m particles per site, the filling for each colour is given by $1/k = m/N$. We could in principle imagine a chiral state with arbitrary flux. But as it has been empirically observed that we should be looking for a flux configuration for which the band structure presents a large gap. To systematically study the gap as a function of the flux ϕ , we present in FIG. 5.1 a Hofstadter butterfly. For example, let us consider the case $k = 6$ and try to find a flux for which a sixth of the bands are filled and presenting a large gap. For the flux $\pi/6$, there are 12 bands thus we need to fill the two lowest bands and for the flux $\pi/3$, only the first band needs to be filled. The size of the gap for the $\pi/3$ is of the order of twice the size of the one for $\pi/6$. There are actually no flux for which the flux is larger than the one for $\pi/3$. This indicates that we should be expecting optimal flux for $\phi = 2\pi/k$ therefore having only the first band filled.

As we want to study the chiral wave function with $\phi = 2\pi/k$ flux per square plaquette, we need to define a unit cell that accommodates such a flux. A convenient way to achieve that is to define a rectangular unit cell with basis vector $\mathbf{a} = (k, 0)$ and $\mathbf{b} = (0, 1)$ containing k sites as represented in FIG. 5.1. We see that all horizontal bonds are real and the vertical ones have a complex phase. For more details on the phases, refer to the legend of the figure.

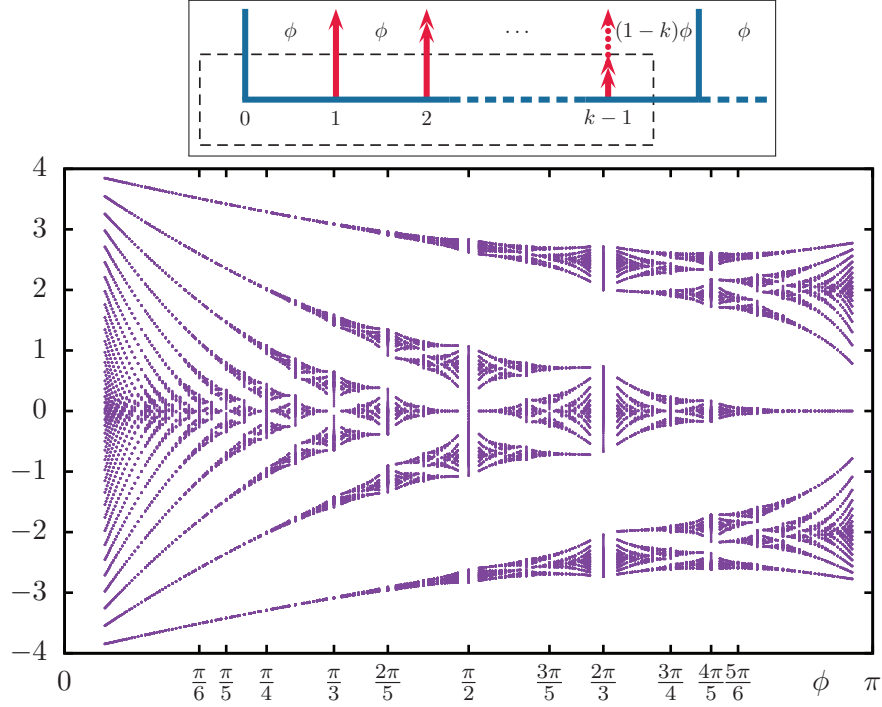


Figure 5.1 – Upper panel: Schematic representation of the χ_{ij} on a square lattice. The dashed black rectangle represents the unit cell with k sites. The colourful lines are the bonds connecting different sites of the lattice. The blue lines take the value $\chi \in \mathbb{R}$, while the red arrows take the value $\chi e^{i s \phi}$, where s denotes the site index. The value of the phase is also symbolised by the number of head per arrows. All horizontal bonds are real and the vertical ones have a complex phase. Each plaquette contains a flux of ϕ or equivalently $(1 - k)\phi = \phi - 2\pi$. Lower panel: Hofstadter butterfly for the square lattice computed using the unit cell above for fluxes $\phi = p\pi/q$, $p \leq q \in \mathbb{N}$.

5.1.1.2 Derivation of the mean-field energy

Here we present in detail what has been used in [43] to compute the chiral energy for $5 \leq k \leq 8$. We do so because we are interested in the unpublished energies for the cases $k = 3, 4$.

In the Hamiltonian (1.91), let us rewrite the sum over all pairs of nearest neighbours by a sum over all unit cells. By noting \mathbf{m} , the position of the unit cell, and s , the index of the particles inside it, the first term in the Hamiltonian (5.1) becomes:

$$\sum_{\langle i, j \rangle} \chi_{ij} \hat{c}_i^\dagger \hat{c}_j = \sum_{\mathbf{m}} \sum_{s=0}^{k-1} \chi_{(\mathbf{m}, s), (\mathbf{m}+\mathbf{b}, s)} \hat{c}_{\mathbf{m}, s}^\dagger \hat{c}_{\mathbf{m}+\mathbf{b}, s} + \chi_{(\mathbf{m}, s), (\mathbf{m}, s+1)} \hat{c}_{\mathbf{m}, s}^\dagger \hat{c}_{\mathbf{m}, s+1} \quad (5.4)$$

Note that two neighbours may belong to two different cells and therefore in this notation $(\mathbf{m}, k) = (\mathbf{m} + \mathbf{a}, 0)$ means that the site indexed by the k -th site in the unit cell at position \mathbf{m} is also the one indexed by 0 in same unit cell translated by \mathbf{a} .

Chapter 5. Square lattice

To enforce the flux configuration shown on FIG. 5.1, we consider only exchange terms such that:

$$\chi_{(\mathbf{m},s),(\mathbf{n},s')} = \begin{cases} \chi & \text{if } s' = s + 1 \text{ and } \mathbf{m} = \mathbf{n} \\ \chi e^{is\varphi} & \text{if } s' = s \text{ and } \mathbf{m} = \mathbf{n} \pm \mathbf{b} \\ 0 & \text{otherwise} \end{cases} \quad \chi \in \mathbb{R} \quad (5.5)$$

The constant term becomes:

$$\epsilon_0 = \frac{2n\chi^2}{JN} \quad (5.6)$$

because on a square lattice with n sites, there is $2n$ bonds connecting nearest neighbours.

We should now define the creation and annihilation operators in the momentum space:

$$\hat{c}_{\mathbf{m},s} = \frac{1}{\sqrt{M}} \sum_{\mathbf{p}} \hat{c}_{\mathbf{p},s} e^{i\mathbf{p}\mathbf{m}} \quad \hat{c}_{\mathbf{m},s}^\dagger = \frac{1}{\sqrt{M}} \sum_{\mathbf{p}} \hat{c}_{\mathbf{p},s}^\dagger e^{-i\mathbf{p}\mathbf{m}} \quad (5.7)$$

$$\hat{c}_{\mathbf{p},s} = \frac{1}{\sqrt{M}} \sum_{\mathbf{m}} \hat{c}_{\mathbf{m},s} e^{-i\mathbf{p}\mathbf{m}} \quad \hat{c}_{\mathbf{p},s}^\dagger = \frac{1}{\sqrt{M}} \sum_{\mathbf{m}} \hat{c}_{\mathbf{m},s}^\dagger e^{i\mathbf{p}\mathbf{m}} \quad (5.8)$$

where M is the number of unit cell, $n = kM$ when n is the number of sites. Thus the Fourier transform of a generic term is:

$$\sum_{\mathbf{m}} \chi_{(\mathbf{m},s),(\mathbf{n},s')} \hat{c}_{\mathbf{m},s}^\dagger \hat{c}_{\mathbf{n},s'} = \frac{1}{M} \sum_{\mathbf{m}} \sum_{\mathbf{p},\mathbf{q}} \chi_{(\mathbf{m},s),(\mathbf{n},s')} \hat{c}_{\mathbf{p},s}^\dagger \hat{c}_{\mathbf{q},s'} e^{-i\mathbf{p}\mathbf{m}} e^{i\mathbf{q}\mathbf{n}} \quad (5.9)$$

This expression could be specialised to the two terms in (5.4) to get:

$$\sum_{\mathbf{m}} \chi_{(\mathbf{m},s),(\mathbf{m}+\mathbf{b},s)} \hat{c}_{\mathbf{m},s}^\dagger \hat{c}_{\mathbf{m}+\mathbf{b},s} = \frac{\chi}{M} \sum_{\mathbf{m}} \sum_{\mathbf{p},\mathbf{q}} \hat{c}_{\mathbf{p},s}^\dagger \hat{c}_{\mathbf{q},s} e^{i(s\varphi+\mathbf{q}\mathbf{b})} e^{-i\mathbf{m}(\mathbf{p}-\mathbf{q})} = \chi \sum_{\mathbf{p}} \hat{c}_{\mathbf{p},s}^\dagger \hat{c}_{\mathbf{p},s} e^{i(s\varphi+\mathbf{p}\mathbf{b})} \quad (5.10)$$

$$\sum_{\mathbf{m}} \chi_{(\mathbf{m},s),(\mathbf{m},s+1)} \hat{c}_{\mathbf{m},s}^\dagger \hat{c}_{\mathbf{m},s+1} = \frac{\chi}{M} \sum_{\mathbf{m}} \sum_{\mathbf{p},\mathbf{q}} \hat{c}_{\mathbf{p},s}^\dagger \hat{c}_{\mathbf{q},s+1} e^{-i\mathbf{m}(\mathbf{p}-\mathbf{q})} = \chi \sum_{\mathbf{p}} \hat{c}_{\mathbf{p},s}^\dagger \hat{c}_{\mathbf{p},s+1} \quad (5.11)$$

By gathering these two last equalities, we get:

$$\sum_{\langle i,j \rangle} \chi_{ij} \hat{c}_i^\dagger \hat{c}_j = \chi \sum_{\mathbf{p}} \sum_{s=0}^{k-1} e^{i(\mathbf{p}\mathbf{b}+s\varphi)} \hat{c}_{\mathbf{p},s}^\dagger \hat{c}_{\mathbf{p},s} + e^{i\mathbf{p}\mathbf{a}\delta_{s+1,k}} \hat{c}_{\mathbf{p},s}^\dagger \hat{c}_{\mathbf{p},s+1} \quad (5.12)$$

The other non constant term of (1.91) is simply the complex conjugate of the previous equation which allows us to introduce a convenient matrix notation:

$$\hat{H}_{\text{MFS}}^\chi = \sum_{\mathbf{p}} \hat{c}_{\mathbf{p}}^\dagger \chi_{\mathbf{p}} \hat{c}_{\mathbf{p}} + \epsilon_0 \quad \hat{c}_{\mathbf{p}}^\dagger = \left(\hat{c}_{\mathbf{p},0}^\dagger, \dots, \hat{c}_{\mathbf{p},k-1}^\dagger \right) \quad (5.13)$$

where $\chi_{\mathbf{p}}$ are $k \times k$ matrices which entries are:

$$(\chi_{\mathbf{p}})_{lm} = \begin{cases} \chi \cos(\mathbf{p}\mathbf{b} + l\phi) & \text{if } l = m \\ \chi e^{\text{sgn}(l-m)i\mathbf{p}\mathbf{a}} & \text{if } |l - m| = k - 1 \\ \chi & \text{if } |l - m| = 1 \\ 0 & \text{otherwise} \end{cases} \quad (5.14)$$

We can diagonalise this Hamiltonian using a unitary matrix $U_{\mathbf{p}}$ and defining new operators $\hat{\mathbf{f}}_{\mathbf{p}}$ and $\hat{\mathbf{f}}_{\mathbf{p}}^{\dagger}$ such that:

$$\hat{\mathbf{f}}_{\mathbf{p}} = U_{\mathbf{p}} \hat{\mathbf{c}}_{\mathbf{p}} \quad \hat{\mathbf{f}}_{\mathbf{p}}^{\dagger} = \hat{\mathbf{c}}_{\mathbf{p}}^{\dagger} U_{\mathbf{p}}^{\dagger} \quad (5.15)$$

Let us explicit the connection between those operators:

$$\hat{f}_{\mathbf{p},b} = \sum_{s=0}^{k-1} (U_{\mathbf{p}})_{bs} \hat{c}_{\mathbf{p},s} \quad \hat{f}_{\mathbf{p},b}^{\dagger} = \sum_{s=0}^{k-1} (U_{\mathbf{p}}^{\dagger})_{sb} \hat{c}_{\mathbf{p},s}^{\dagger} \quad (5.16)$$

$$\hat{c}_{\mathbf{p},s} = \sum_{b=0}^{k-1} (U_{\mathbf{p}}^{\dagger})_{sb} \hat{f}_{\mathbf{p},b} \quad \hat{c}_{\mathbf{p},s}^{\dagger} = \sum_{b=0}^{k-1} (U_{\mathbf{p}})_{bs} \hat{f}_{\mathbf{p},b}^{\dagger} \quad (5.17)$$

After the diagonalisation, the Hamiltonian takes the form:

$$\hat{H}_{\text{MFS}}^{\chi} = \sum_{\mathbf{p}} \hat{\mathbf{f}}_{\mathbf{p}}^{\dagger} E_{\mathbf{p}} \hat{\mathbf{f}}_{\mathbf{p}} + \epsilon_0 \quad \text{with} \quad (E_{\mathbf{p}})_{sb} = \delta_{sb} \omega_{\mathbf{p},b}(\chi) \quad (5.18)$$

The explicit dependence of the eigenvalues $\omega_{\mathbf{p},b}(\chi)$ has been written to make more obvious the fact the spectrum is a homogeneous function of χ :

$$\omega_{\mathbf{p},b}(\lambda\chi) = \lambda \omega_{\mathbf{p},b}(\chi) \quad \text{for} \quad \lambda \in \mathbb{R} \quad (5.19)$$

It is now trivial to construct a state consisting of a filled first band:

$$|\chi\rangle = \prod_{\mathbf{p}} \hat{f}_{\mathbf{p},1}^{\dagger} |0\rangle \quad (5.20)$$

The corresponding energy is given by:

$$\langle \hat{H}_{\text{MFS}}^{\chi} \rangle = \langle \chi | \hat{H}_{\text{MFS}}^{\chi} | \chi \rangle = \sum_{\mathbf{p}} \omega_{\mathbf{p},1}(\chi) + \epsilon_0 \quad (5.21)$$

As this energy only takes into account a single colour, it has to be multiplied by N to get the total energy:

$$E_{\text{MFS}}^{\chi} = N \langle \hat{H}_{\text{MFS}}^{\chi} \rangle = N \sum_{\mathbf{p}} \omega_{\mathbf{p},1}(\chi) + \frac{2n\chi^2}{J} \quad (5.22)$$

Chapter 5. Square lattice

This can be expressed in a more convenient fashion by introducing $\tilde{\chi}$ such that $\chi = JN\tilde{\chi}$:

$$\epsilon_\chi \equiv \frac{E_{\text{MFS}}^\chi}{JN^2n} = \frac{1}{n} \sum_{\mathbf{p}} \omega_{\mathbf{p},1}(\tilde{\chi}) + 2\tilde{\chi}^2 \quad (5.23)$$

$$= \frac{1}{kM} \sum_{\mathbf{p}} \omega_{\mathbf{p},1}(\tilde{\chi}) + 2\tilde{\chi}^2 \quad (5.24)$$

$$= \frac{1}{kS} \int \omega_{\mathbf{p},1} d\mathbf{p}(\tilde{\chi}) + 2\tilde{\chi}^2 \quad (5.25)$$

where S is the integration surface. As $\omega_{\mathbf{p},1}$ depends on χ , the energy will be proportional to χ . So if one was to compute this energy with a random value of χ , the energy would of course be wrong. To correctly fix χ , the constraint (5.3) on χ_{ij} has to be used:

$$\chi_{(\mathbf{m},s),(\mathbf{n},s')} = -JN \langle \hat{c}_{\mathbf{m},s}^\dagger \hat{c}_{\mathbf{n},s'} \rangle \quad (5.26)$$

$$= -\frac{JN}{M} \sum_{\mathbf{p},\mathbf{q}} e^{-i\mathbf{p}\mathbf{m}} e^{i\mathbf{q}\mathbf{n}} \langle \hat{c}_{\mathbf{p},s}^\dagger \hat{c}_{\mathbf{q},s'} \rangle \quad (5.27)$$

$$= -\frac{JN}{M} \sum_{\mathbf{p},\mathbf{q}} \sum_{b,b'} e^{-i\mathbf{p}\mathbf{m}} e^{i\mathbf{q}\mathbf{n}} (U_{\mathbf{p}})_{bs} (U_{\mathbf{q}}^\dagger)_{s'b'} \langle \hat{f}_{\mathbf{p},b}^\dagger \hat{f}_{\mathbf{q},b'} \rangle \quad (5.28)$$

$$= -\frac{JN}{M} \sum_{\mathbf{p}} e^{-i\mathbf{p}(\mathbf{m}-\mathbf{n})} (U_{\mathbf{p}})_{1s} (U_{\mathbf{p}}^\dagger)_{s'1} \langle \hat{f}_{\mathbf{p},1}^\dagger \hat{f}_{\mathbf{p},1} \rangle \quad (5.29)$$

$$= -\frac{JN}{M} \sum_{\mathbf{p}} e^{-i\mathbf{p}(\mathbf{m}-\mathbf{n})} (U_{\mathbf{p}})_{1s} (U_{\mathbf{p}}^\dagger)_{s'1} \quad (5.30)$$

The same kind of computation leads to:

$$m = N \langle \hat{c}_{\mathbf{m},s}^\dagger \hat{c}_{\mathbf{m},s} \rangle = \frac{N}{M} \sum_{\mathbf{p}} (U_{\mathbf{p}})_{1s} (U_{\mathbf{p}}^\dagger)_{s1} \quad (5.31)$$

It is worth noticing that there is a simpler solution than computing (5.25). Coming back to (1.91), we see that the energy will be given by:

$$E_{\text{MFS}}^\chi = N \sum_{\langle i,j \rangle} \left(\chi_{ij} \langle \hat{c}_i^\dagger \hat{c}_j \rangle + \chi_{ij}^* \langle \hat{c}_j^\dagger \hat{c}_i \rangle \right) + E_0 \quad (5.32)$$

$$= -\frac{1}{J} \sum_{\langle i,j \rangle} \left(\chi_{ij} \chi_{ij}^* + \chi_{ij}^* \chi_{ij} \right) + E_0 \quad (5.33)$$

$$= -\frac{2n|\chi|^2}{J} \quad (5.34)$$

This leads to a normalised energy of:

$$\epsilon_\chi = -2|\tilde{\chi}|^2 \quad (5.35)$$

We have given two equivalent ways to compute the energy. Both ways require the initial computation of $\tilde{\chi}$ using (5.30) for a particular bond, *e.g.* for $\chi_{(\mathbf{m},s),(\mathbf{m},s+1)}$. Once this value is known, it can be plugged in (5.25) or more simply in (5.35).

5.1.2 Valence Cluster State

The other states of interest, introduced by Hermele and Gurarie [44] as k -simplex VCS states, are the analog of the valence bond states for $k \geq 3$ introduced by Rokhsar [42] for $k = 2$. These states were already predicted to be the ground state for SU(3) on the kagome lattice or SU(4) on the checkerboard lattice in the fundamental irrep [77]. They break the lattice symmetries by building k -site singlet. At the saddle point, *i.e.* in the large- N limit, each site belonging to a given k -simplex K is connected to all other sites of K by $\chi_{ij} = \chi \neq 0$, $i, j \in K$ and disconnected from sites of other k -simplices, $\chi_{ij} = 0$, $i, j \notin K$. For $k \geq 2$, these states have an energy which provides a lower bound to the mean-field energy:

$$\frac{E_{\text{MFS}}}{JN^2n} \geq \frac{1-k}{2k^2} \quad (5.36)$$

For bipartite lattices, the bound is even stricter when $k > 2$:

$$\frac{E_{\text{MFS}}}{JN^2n} \geq \frac{E_{\text{MFS}}^{k\text{VCS}}}{JN^2n} \equiv \epsilon_{k\text{VCS}} = -\frac{1}{4k} \quad (5.37)$$

This lower bound may not only be saturated by k -simplex VCS states. For instance the square lattice does not admit any k -simplex VCS state for $k \geq 3$, but the VCS states shown in FIG. 5.2 for $k = 3, 4$ saturate the bounds. The energy of the 2-site problem gives an additional lower bound:

$$\frac{E_{\text{MFS}}}{JN^2n} \geq -\frac{2}{k^2} \quad (5.38)$$

which becomes stricter than (5.37) for $k > 8$ and therefore prevents the bound saturation. For $5 \leq k \leq 8$, the conditions required to saturate the bounds are very strong, it is therefore expected that no saturation can occur.

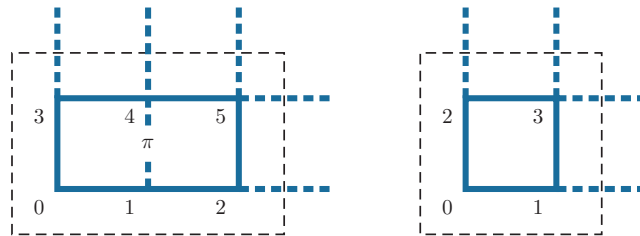


Figure 5.2 – VCS states for $k = 3$ and $k = 4$ are represented on the left and right respectively. The blue dashed lines are such that $\chi_{ij} = 0$, while the continuous ones are bonds that connect different sites of the same k -simplex and are such that $\chi_{ij} = \chi$. Note that for the $k = 3$ case, the rectangular clusters contain a flux π . The black dashed lines represent the (3×2) and (2×2) unit cells.

5.1.3 Mean-field energies

Now that the relevant mean-field states have been introduced, the TAB. 5.1 lists their energies respectively computed with (5.35) or (5.37) for $3 \leq k \leq 6$. This table confirms that the k -simplex VCS energy is always lower than the chiral energy, but one should keep in mind that the k -simplex VCS energy occurs at bond saturation which is never the case for $k \geq 5$.

k	3	4	5	6
ϵ_χ	-0.0820492	-0.0581951	-0.0430802	-0.0330693
$\epsilon_{k\text{VCS}}$	-0.083	-0.0625	-0.05	-0.0416
r	0.007764	0.035666	0.074342	0.115041

Table 5.1 – Comparison between the chiral and k -simplex VCS energies for different k . The energies are given in units of JN^2n and the ratio is given by $r = (\epsilon_\chi - \epsilon_{k\text{VCS}}) / (|\epsilon_\chi + \epsilon_{k\text{VCS}}|)$

The quite intuitive reason why saturation is unlikely for $k \geq 5$, is that the square lattice cannot be split into k -simplex. It is nevertheless worth wondering what happens for $k = 6$. Indeed we saw that for $k = 3$, a VCS state composed with six-site clusters saturates the bonds. The same kind of state could eventually saturate the bonds in the $k = 6$ case. This would therefore challenge the supposed existence of a chiral ground state in the mean-field. As there is a big energy difference, $r \approx 10\%$, between the chiral and k -simplex VCS states, some intermediate states could exist. The $k = 3$ case is also interesting because the energy difference is very small, $r \approx 0.8\%$. Hence, we may wonder how competitive the VCS state is, when we move away from the mean-field limit.

The next section will explain the use of the VMC with the PSO algorithm to go beyond the mean-field approximation and find energetically good solutions. From now on, we fix $J = 1$ for simplicity, so J will disappear from all equations.

5.2 Variational wave functions and PSO

As we mentioned, the $SU(3m)$ and $SU(6m)$ are very interesting models because they share some properties but exhibit completely different mean-field ground states. The principle aim of this work is to distinguish $SU(km)$ models with fixed k that have a chiral or VCS ground state in the mean-field limit. We also want to find for which finite value of m , the ground state becomes qualitatively similar to the mean-field solution. Indeed for $m = 1$, as some ground states are known to be different from the mean-field ones, a transition must occur. For instance, beside the well-known $SU(2)$ case, a three-sublattice ordered state is predicted for $N = 3$ [28]. For $N = 4$ the ground state is believed to consist of dimers of alternating pairs of colour building a Néel-like state [31]. The $N = 5$ case has been less studied but exact diagonalisation tends to show that there is a five-sublattice colour ordered ground state [32]. All of these possibilities have been explored with VMC and the results will be shown in section 5.4. Unfortunately, as we will see later, VMC based on fermionic wave functions is ill-suited to

study ordered phases. Therefore, we will not probe for colour ordered states in the study of the $SU(3m)$ and $SU(6m)$ phase diagrams.

Now that we have selected what type of ground states we want to probe, we can define variational wave functions adapted to this task. By getting rid of the chemical potential in the variational Hamiltonian (2.10), we get:

$$\hat{T} = \sum_{\langle i,j \rangle} t_{ij} \hat{c}_i^\dagger \hat{c}_j + \text{h.c.} = \sum_{\mathbf{m}} \sum_{s=1}^{n/M} \sum_{\tau \in \{h,v\}} t_{s\tau} \hat{c}_{\mathbf{m}s}^\dagger \hat{c}_{\mathbf{m}s+\tau} + \text{h.c.} \quad (5.39)$$

where \mathbf{m} keeps track of the unit cell position, s is indexing the sites inside the unit cell and τ is the direction of the bond (horizontal or vertical).

As discussed in the previous section, we want to compare two completely different states, chiral and VCS states. The unit cell shown in FIG. 5.1 together with (5.5) allows the creation of a wave function that captures the physics of the chiral state with $\phi = 2\pi/k$ flux per square plaquette. All bonds connecting two sites s and $s+\tau$ have the same hopping amplitude $|t_{s\tau}| = t$. The flux is created by setting the phase of all horizontal bonds to zero $t_{sh} = t$, while the vertical ones carry a phase $s\phi$: $t_{sv} = t e^{is\phi}$. This is a very simple variational wave function to study because there is no variational parameter and thus, no optimisation is required.

The other relevant wave function is the VCS one. The most straightforward way to build it is to set the amplitude of the bonds so that the energy of the bonds produces a VCS state after projection. As the results will show, it is less obvious than it seems to build an optimal VCS wave function. Therefore, we chose another approach to systematically explore the phase diagram. Instead of guessing the optimal way to build the VCS wave function, we decided to start with the variational Hamiltonian (5.39) and to optimise the hopping parameters $t_{s\tau} \in \mathbb{R}$ for some unit cells. The (3×2) unit cell is the smallest unit cell that we used and is depicted on the left of FIG. 5.2. We used two other unit cells, namely the (3×3) and (4×3) containing 9 and 12 sites respectively. For a unit cell with B bonds, we will use $B - 1$ bonds as free variational parameters, the remaining bond being set to $t = -1$. The value of one bond has to be fixed to prevent having two identical variational wave functions created by two different sets of hopping terms. Indeed, by rescaling all hopping terms by a constant, the eigenvectors of \hat{T} and the variational wave function are unchanged. Finally, as they depend on free variational parameters, these wave functions will be referred to as free wave functions except when all hopping terms are t . In that case, the particular name of Fermi wave function is chosen. We see that the number of parameters to optimise can be quite large, up to 23 free parameters for the (4×3) unit cell. The optimisation process was performed by the PSO algorithm, presented in 2.2. We will study systems with antiperiodic boundary conditions for $k = 3, 6$, $m = 1, 2, 3, 4$, $n = 36, 72, 144$ and all allowed unit cells. On average more than 170 000 different variational parameters have been measured for each simulation.

5.3 Results

We will now present the results obtained for the phase diagram of the $SU(3m)$ and $SU(6m)$ Heisenberg model. We will start by discussing the case $k = 3$ and provide a strong indication that the ground state is a VCS state, when $m > 3$. The cases $m = 2, 3$ will turn out to be more controversial due to the intense competition between the chiral and VCS state. Nevertheless, the variational results indicate that the ground state is chiral for $m = 2$ and VCS for $m = 3$. The second part will present results for the case $k = 6$, for which VMC predicts a chiral ground state for $m > 1$. The $m = 1$ case is also more subtle, but the ground state is expected to break the translation symmetries in both directions.

5.3.1 $k = 3$

To present the results obtained for the $SU(3m)$ Heisenberg model, we will first discuss raw VMC results obtained by the PSO algorithm. Despite looking complicated, we will see that most of the solutions are related to each other, at least at the physical level. This will allow us to draw some conclusions on the nature of the optimal solution in the thermodynamic limit. These solutions will finally be compared to other variational wave functions.

The first results that we show in FIG. 5.3 are the optimal solutions found by the PSO algorithm for the free wave function. Each row represents a different value of m and each column a different system size. For all solutions, the variational parameters are indicated on the left and the bond energy on the right. Before discussing the physics and reliability of the results, some general observations will be made. Some of the solutions display a non-trivial flux configuration with a flux of π in some plaquettes. Indeed, when a hopping term is positive (shown in blue), it carries a phase of π . The presence of a flux per plaquette is then simply determined by the parity of the number of positive bond around that plaquette. As only the parity is involved, one could reverse the sign of all hopping terms and still get the exact same solution. Moreover, there are different ways to achieve the same flux-configuration. For instance the signs of the hopping terms of (a) and (d) are different, but the overall flux-configuration is identical. By looking at (e) and (f), one should notice that those two solutions are similar in the sense that up to some translation of the unit cell, both solutions present very similar bond energy. Note also for instance that the solutions (h), (i), (k) and (l) are similar.

Let us briefly comment on the reliability of those results. It is impossible to know if the solutions presented are the optimal ones, but we strongly believe that, if they are not optimal, they are at least very close in energy. Indeed, we observed that already after a few thousands of measures, the solutions found were usually similar to the ones shown in FIG. 5.3 and have a competitive energy. We should also mention that the term “optimal” has to be understood in the sense that only the hopping terms of the variational Hamiltonian (5.39) have been optimised. One could start with a different variational Hamiltonian and get better variational energies.

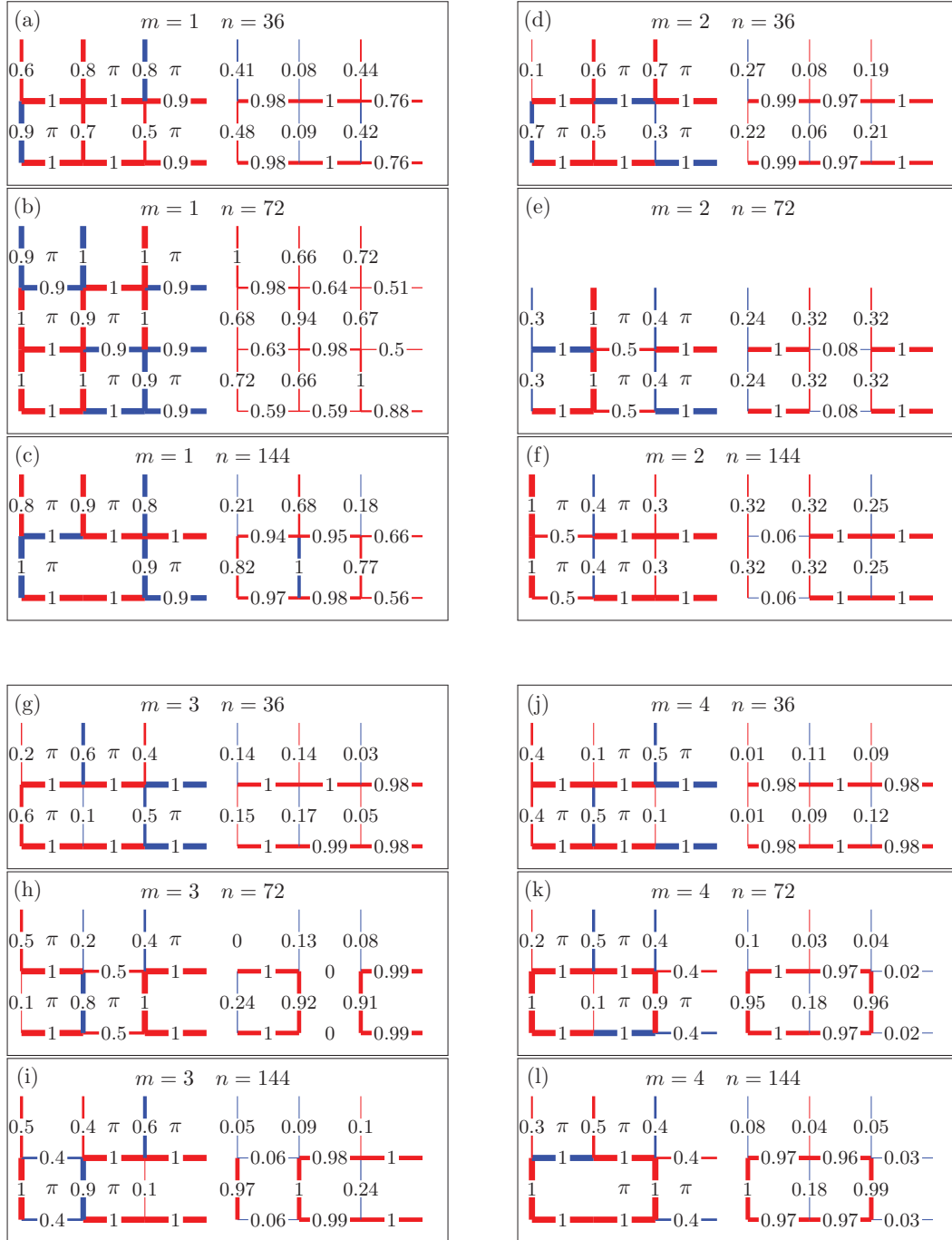


Figure 5.3 – Raw results of the optimal solution found by the PSO algorithm for $k=3$ with different m and n . For each solution we schematically present for one unit cell the set of optimal parameters on the left and the energies of the bonds on the right. Their absolute values are expressed by the width of the lines and by a number proportional to the maximal absolute value. A link is drawn in red (blue) if negative (positive). The flux in each square plaquette is also indicated by π .

We will start discussing the physics for each particular values of m by saying that, according to previous studies, the $m = 1$ case should exhibit a three-sublattice colour order. Therefore, we do not expect to find competitive energies because our variational wave functions are not supposed to reproduce this type of order. Nonetheless, it is worth commenting the finite size effect of the results. The solution (b) is the only type of optimal solution found on a (3×3) unit cell. This state consists of diagonal zig-zagging chains with stronger bond energies and is triply degenerate. The other unit cells seem to be penalised on the 72-site system due to its particular tilted geometry. This is confirmed because on the 144-site system, where finite size effects are weaker, the optimal solution shown on a (3×2) unit cell is in competition with a solution similar to (b).

For $m > 1$, on the smallest systems, where the finite size effects are big, we see that the optimal solution consists of chains coupled together by weak positive and negative bonds. As soon as the systems are big enough, $n \geq 72$, the translation symmetries are broken and a columnar trimer state is favoured for $m = 2$, while a plaquette state is favoured for $m \geq 3$. This plaquette state consists of 6-site rectangular clusters, where the central bond is weaker than the other and positive. It is interesting to note that the bigger n and m are, the stronger the bonds between the six sites become and the weaker the central bond gets. This is the awaited behaviour since these state are expected to become the VCS state shown in FIG. 5.2 in the mean-field limit. To finalise this analysis, we should emphasise that for each case we found many non-trivial sets of variational parameters giving comparable energies. It is impossible to list them all here, but the relevant criterion is not the set variational parameters but the states obtained after projection, *i.e.* the bond energies. We saw on FIG. 5.3 that the general trend is that the larger m is, the more favored the VCS states become. This could have been guessed from the mean-field analysis, but here we provide a quantitative confirmation which is valid even for small m .

Now that we have analysed the results for the free wave function, we compare them to the chiral and the Fermi ones in FIG. 5.4. Each plot represents a different value of m and displays the normalised energies as a function of the inverse system size. The normalisation is done such that the energy in the thermodynamic limit of the free wave function is at the origin. As we saw for the 72-site system, the ground state energy may be affected by the geometry of the system, *i.e.* whether it is tilted ($n = p^2 + q^2$) or not ($n = L^2$). To do a proper extrapolation, the geometry has to be taken into account. As there are not enough points to do an extrapolation for both type of geometries, energies on larger systems, *e.g.* $n = 180, 288, 324$, were computed using the best set of variational parameter obtained for the system with $n = 144$. Even if these energies are not optimal, they provide a higher bond. Thanks to those additional data, one fit can be performed for the system with 36, 144 and 324 sites, and another with 72, 180 and 288. The energy of the free wave function in the thermodynamic limit is then given by the average of the two extrapolations. Doing one fit for the chiral wave function for all sizes is satisfying because the finite site effects are weaker. On this scale, the energy of the Fermi wave function cannot be seen because it is too high.

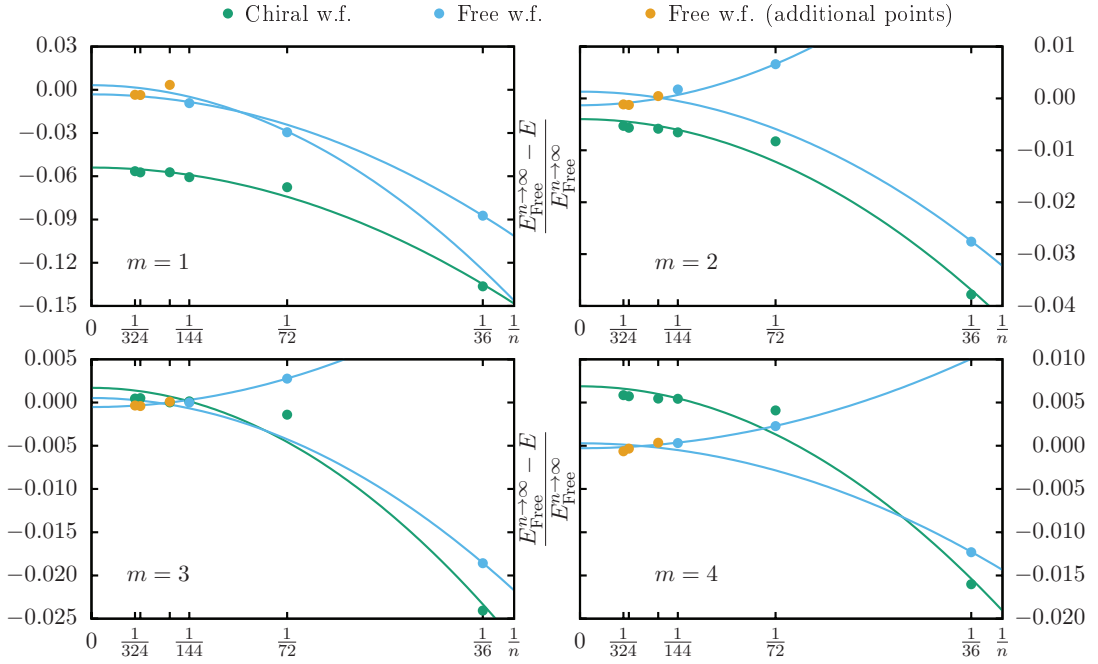


Figure 5.4 – The green and blue circles represent VMC energies for the $SU(3m)$ Heisenberg model obtained thanks to the PSO algorithm for respectively the chiral and free wave function. The yellow circles are the additional energies of the free wave function computed with best variational parameter obtained for the $n = 144$ system. The energies given as a function of the inverse system size are normalised so they can be plotted on a comparable scale. To take the different geometries into account, two extrapolations (blue lines) of the energies of the free wave function were averaged to give $E_{\text{Free}}^{n \rightarrow \infty}$. The function used to fit the data is $f(x) = ax^2 + b$ and the error bars are smaller than the symbols.

The plot on FIG. 5.5 displays the extrapolated energies for the three wave functions. The $m = 1$ case shows that the chiral wave function has the best variational energy despite being higher than the energy of the three sublattice ordered state. For $m = 2$, the best variational energy is again the chiral one, even if the competition with a columnar trimerised state given by the free variational wave function is strong. As there is currently no other numerical result and as the energy difference between the chiral and columnar state is very small, it is difficult to conclude with certainty on the nature of this ground states. Nevertheless, if the VMC results are correct, the $SU(6)$ with $m = 2$ is an experimentally realisable system, where a chiral ground state could be observed. As soon as m is larger, $m \geq 3$, the free wave function becomes optimal. This is also supported by the fact that, before extrapolation, the chiral energies are higher for $n > 144$, even if no proper optimisation was performed for those system sizes. The state created by this wave function is a 6-site plaquette state like the VCS state expected in the mean-field limit. The guides to the eyes on FIG. 5.5 show that the VMC results qualitatively agree with the mean-field solutions, more explicitly the chiral energy is higher than the VCS one when m is large enough.

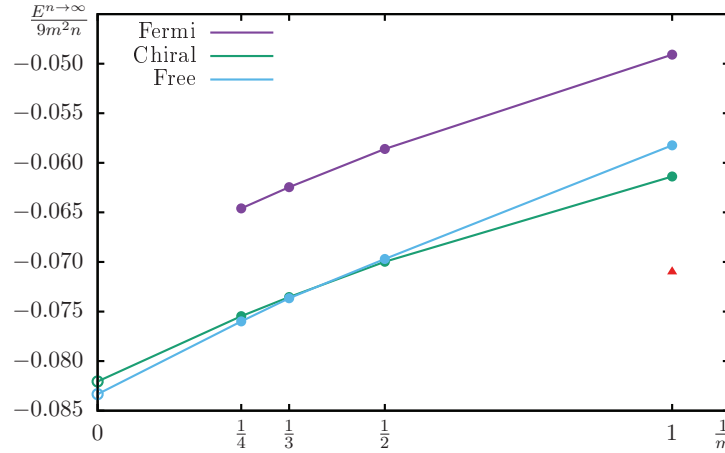


Figure 5.5 – The filled circles represent VMC thermodynamic energies for the $SU(3m)$ Heisenberg model as a function of m . The purple, green and blue colours are respectively for the Fermi, chiral and free wave function. The error bars are smaller than the symbols. The red triangle gives an indication of the energy obtained in reference [28]. The empty circles are mean-field energies for the chiral and VCS states shown in TAB. 5.1. The lines are a guide to the eyes.

The essential result presented in this section is that the optimisation of the free variational wave function has found an optimal set of parameters that gives a variational energy lower than the chiral energy for $m > 2$. Even if the optimal variational parameter sets are highly non-trivial, the bond energy configuration is quite simple and presents the same features than the VCS states. Additionally, the presence of a chiral phase for $m = 2$ cannot be excluded.

5.3.2 $k = 6$

We will now focus on the results for the $SU(6m)$ cases. The optimal solutions found for $m = 1, 2, 3, 4$ on a system with 144 sites will be introduced first. We will then see how the thermodynamic limit can be reached and what the other competitive states are. We will conclude by showing that the chiral state dominates when $m = 1$.

The solutions shown on the left in FIG. 5.6 are obtained for the systems with 144 sites (a)-(d). In all cases, the optimal solution exhibits the same bond energy pattern. The system is composed of stripes of dimers coupled by energetically non-uniform pairs of bonds. Indeed, one pair of facing bonds has a slightly different energy than the two other pairs. This implies that the translation symmetry is broken in both directions.

To do a proper extrapolation to the thermodynamic limit, bigger systems have been studied. As the computation time is large, the simulations have only measured on average 50 000 sets of variational parameter for $n = 180, 288, 324$. The solutions found may not be as optimal as the ones for smaller systems, but they give additional interesting information. Indeed, FIG. 5.6 shows four states on the right (e)-(h) that exhibits some similarities with the optimal solutions

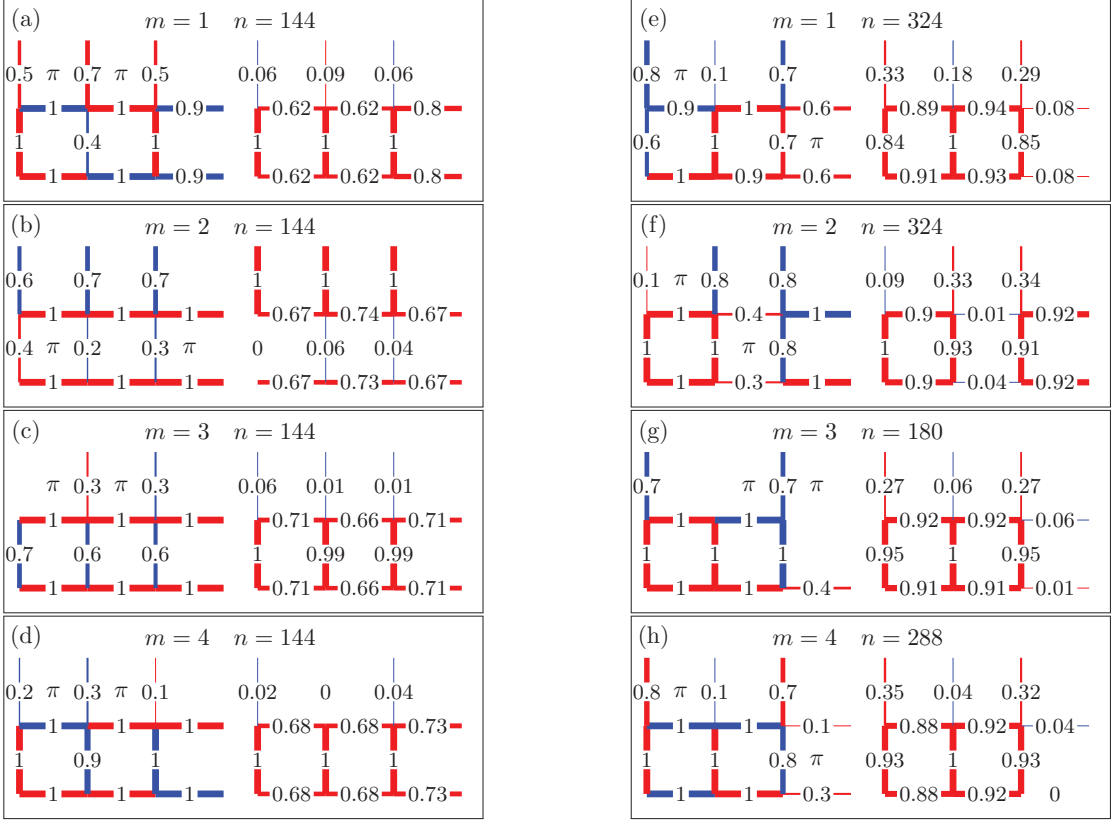


Figure 5.6 – Left: Optimal solutions found by the PSO algorithm for $k = 6$, $m = 1, 2, 3, 4$ and $n = 144$. Right: Examples of competitive solutions obtained in the $k = 6$ case for $m = 1$ with $n = 324$, $m = 2$ with $n = 324$, $m = 3$ with $n = 180$ and $m = 4$ with $n = 288$.

The conventions used here are identical to the ones in FIG. 5.3.

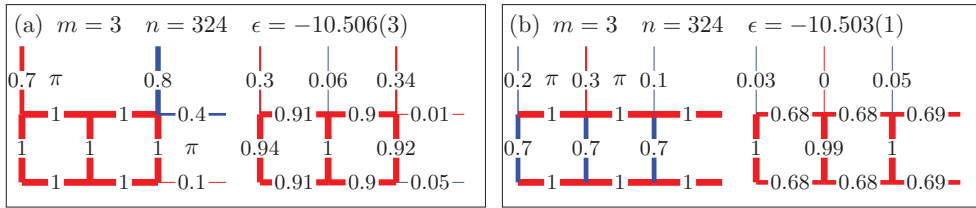


Figure 5.7 – Two best solutions obtained after the measure of more than 50 000 samples for SU(18) $m = 3$ on a system with $n = 324$ sites. The difference between the variational energies are of the order of the error bars.

of the $k = 3$ cases. They display 6-site rectangular plaquettes strongly coupled together along one direction. Along that direction, the couplings between the plaquette consist of one very weak positive bond and two negative ones. In the mean-field limit, the positive bond is expected to disappear, leaving a π -flux between the plaquettes. The bond energies in the other direction is also expected to disappear in this limit. These states can be thought of as

decoupled ladders, where each rung consists of a 6-site singlet. It should be emphasised that the competition between the two types of variational states found by the PSO algorithm is very strong. For instance, for $m = 3$ and $n = 324$ the two best solutions shown in FIG. 5.7 were measured to be equal (within error bars). Of course, by increasing the simulation time one could decide which of those two solutions has the lowest energy.

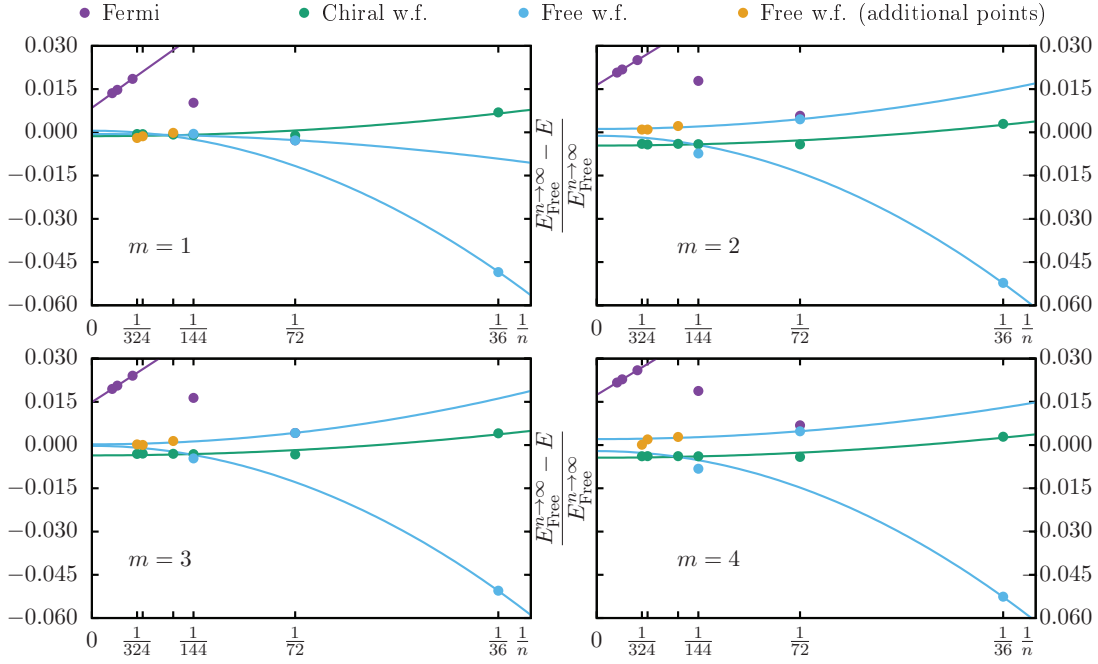


Figure 5.8 – VMC energies for the $SU(6m)$ Heisenberg model. The conventions are the same as in FIG. 5.4 with the exception that the yellow circles are energies obtained after a partial optimisation for $n = 180, 288, 324$.

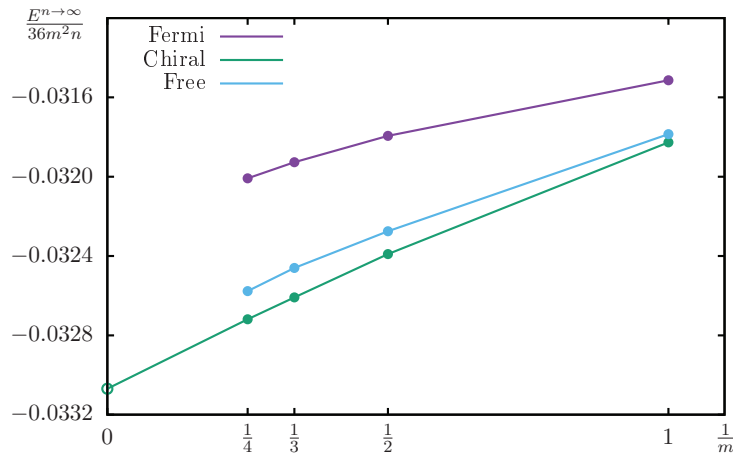


Figure 5.9 – VMC thermodynamic energies for the $SU(6m)$ Heisenberg model. The conventions are the same as in FIG. 5.5.

Thanks to this partial optimisation on larger systems, an extrapolation to the thermodynamic limit was performed and the results are shown in the plots of FIG. 5.8. As in the $k = 3$ case, two different fits were required to extrapolate the energy of the free variational wave function. In FIG. 5.9, the extrapolated energies are given for the three variational wave functions. The $m = 1$ case requires some attention because the chiral and free variational wave functions give comparable energies. By carefully looking at FIG. 5.8 for $m = 1$, we can see that for the largest system, the lowest energy is reached by the state (e) shown in FIG. 5.6. As this state was found after testing few samples, one could certainly improve this energy by performing much longer optimisation. Therefore, the chiral phase is most likely not the ground state for the $m = 1$ case. However for $m > 1$, it becomes clear that the chiral wave function gives the best energy as it is extremely unlikely to find a lower energy using the variational Hamiltonian (5.39). Finally, the guides to the eyes on FIG. 5.9 indicates the good agreement between the chiral energies measured for finite m and the mean-field limit. As expected, neither the Fermi nor free wave function energy is close to the energy of the VCS state at saturation. This confirms the fact that saturation is impossible for $k = 6$.

It is remarkable that the mean-field predictions seem to hold for $m > 1$, *i.e.* the chiral wave function dominates the other wave functions in almost all cases but for $m = 1$. In that specific case, we have found that the ground state of the SU(6) Heisenberg model forms 6-sites plaquette as shown in FIG. 5.6 (e).

5.4 Additional results for $k = 3, 4, 5$

This section will present the attempt to find variational wave functions that create ordered states. The ground states of the Heisenberg model in the fundamental irrep of SU(3), SU(4) and SU(5) are expected to present some kind of colour order. We will shortly discuss the variational results attempting to recover the colour order of SU(3) and SU(5). The SU(4) case deserves more attention and will be treated last.

5.4.1 $k = 3$ and $k = 5$

The SU(3) and SU(5) cases for $m = 1$ are both expected to have a colour ordered ground state given in FIG. 5.10 on the left and right respectively. For SU(3), it consists in a three-sublattice order forming diagonal stripes for each colour [28], while for SU(5), the only colour configuration (up to colour permutation and mirror symmetry) selected by LFWT [32]. To reproduce these types of colour order with VMC, the use of an on-site chemical potential is possible. As we saw in (2.9), it is possible to choose a different variational Hamiltonian for each colour. We will define k different Hamiltonians on the same unit cell containing k sites. The colour $\alpha \in [1, N]$ will obey the Hamiltonian \hat{T}_α with $a = \text{mod}(\alpha, k) + 1 \in [1, k]$. The difference

between the Hamiltonians lies in the position of the chemical potential, *e.g.* \hat{T}_a is given by:

$$\hat{T}_a = \sum_{\mathbf{m}} \sum_{s=1}^{n/M} \left(t \sum_{\tau \in \{h,v\}} \left(\hat{c}_{\mathbf{m}s}^\dagger \hat{c}_{\mathbf{m}s+\tau} + \hat{c}_{\mathbf{m}s+\tau}^\dagger \hat{c}_{\mathbf{m}s} \right) + \mu \delta_{sa} \hat{c}_{\mathbf{m}s}^\dagger \hat{c}_{\mathbf{m}s} \right) \quad (5.40)$$

where μ/t is the variational parameter and δ_{sa} is equal to 1, only when the index s of the site in unit cell is equal to the index a .

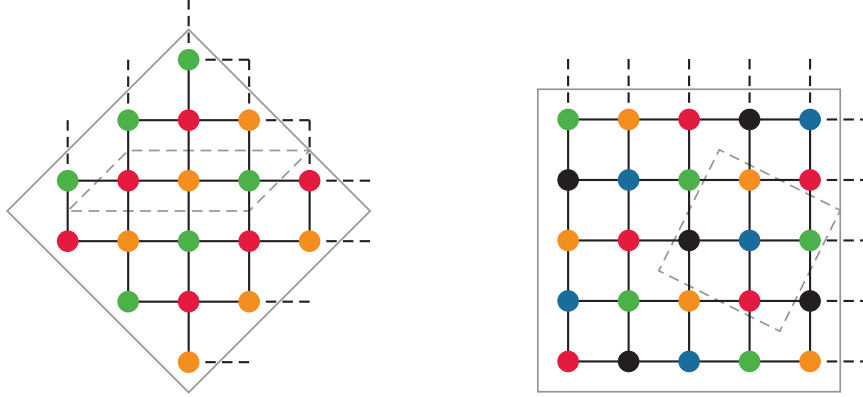


Figure 5.10 – The expected colour order for the SU(3) and SU(5) cases for $m = 1$ are respectively shown on the left and the right. The unit cell is depicted in both cases by the gray dashed lines.

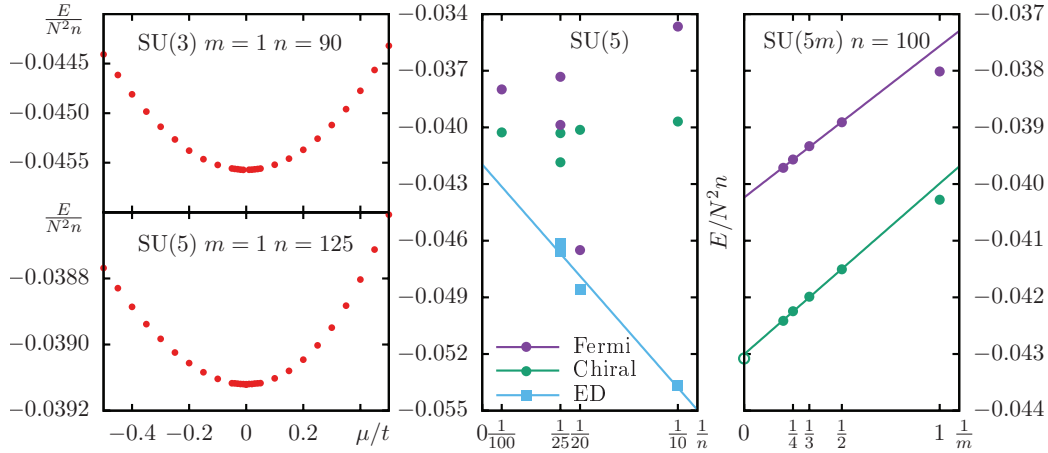


Figure 5.11 – The results were obtained for systems with periodic boundary conditions (except for the Fermi wave function for $n = 20, 100$) and all symbols are bigger than the error bars. Left plots: Variational energy for $m = 1$ as a function of the ratio μ/t for SU(3) (above) on 90 sites and SU(5) on 125 sites (below). Central plot: Comparison between the SU(5) energies obtained by VMC (filled circles) and by ED (filled squares) for different sizes. For $n = 25$, the two different energies correspond to the two possible geometries (tilted or not). The straight line is a linear fit of the ED energies. Right plot: Extrapolation to the mean-field limit of the variational energies of the Fermi and chiral wave function for SU(5m) on a system with 100 sites. The empty circle is the mean-field energy given in TAB. 5.1.

Thanks to this wave function, it should in principle be possible to detect the presence of an ordered state. Unfortunately as the left plots of FIG. 5.11 show, this type of wave function does not seem to be sensitive enough because as soon as $\mu/t \neq 0$, the energy increases and becomes higher than the energy of the Fermi wave function for which $\mu/t = 0$. One could explain this by the fact that the chemical potential “freezes” the particles and the loss of kinetic energy is not compensated by the gain coming from the chemical potential. We confirm a posteriori that the wave function based on (5.40) is not able to capture a colour ordered state for SU(3) and SU(5) with $m = 1$. Hence, the results presented earlier for SU(3) are not challenged by this variational wave function.

The central plot of FIG. 5.11 compares the energies for different system sizes for SU(5) $m = 1$ obtained by ED and VMC for two variational wave functions. The exact energies extrapolate to $\epsilon_{\text{ED}} = -0.042$ which compares relatively well with the energy of the chiral wave function $\epsilon_\chi = -0.040$ with a flux of $2\pi/5$ per square plaquette. A flux of $4\pi/5$ has also been tested but is not represented on the figure because its energy is higher than the one for $2\pi/5$. It was expected to have a higher energy for a flux $4\pi/5$ because the gap between the filled and empty states is bigger for $2\pi/5$ than for $4\pi/5$ as it can be seen in FIG. 5.1. Moreover for SU(5) $m = 1$, the long range correlations computed with Fermi wave function on systems of 25 and 125 sites with periodic boundary conditions are similar to ED results [32]. They both exhibit a pattern, where positive correlations occur for vectors $(2, -1)$ or $(2, 1)$ as predicted by LFWT, see FIG. 5.12. Note that for a system with 125 sites, the symmetry is broken and only one vector is allowed.

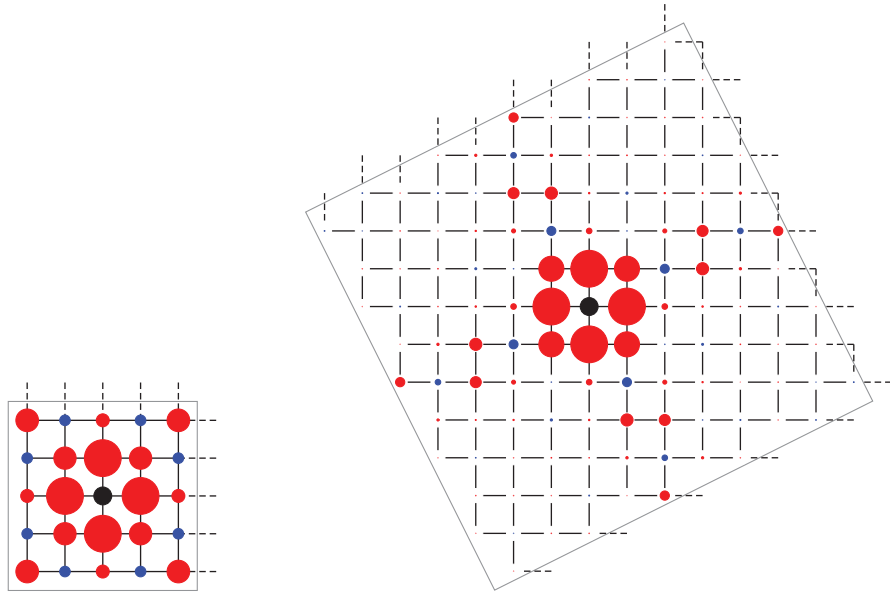


Figure 5.12 – Long range correlations obtained by VMC for the Fermi wave function. The size of the circles is proportional to the correlation. The positive (negative) correlation are in blue (red). The central black circle is the site reference. The left systems contains 25 sites, while the right one contains 125 sites.

For completeness, we present additional results for $SU(5m)$. The right plot of FIG. 5.11 shows the energy of the chiral and Fermi wave functions for a system of 100 sites for different values of m . The chiral wave function is always favoured against the Fermi one. In the limit where $m \rightarrow \infty$, the chiral wave function recovers the mean-field energy shown in TAB. 5.1.

5.4.2 $k = 4$

Let us now turn to the $SU(4)$ $m = 1$ case for which a plaquette state was first predicted [78] but Corboz et al. [31] have shown that a dimerisation appears in the ground state. This means that an irrep of dimension 6 is present on each dimer which provides additional degrees of freedom. The system is then able to develop a Néel-like order consisting in dimers involving different pairs of colours. The left pictures of FIG. 5.13 present the qualitative bond energies (a) and colour occupations (b) of this state in the appropriate (4×2) unit cell. In (a), the system is divided into horizontal dimers of equal strength. The dimers are connected together with vertical bonds of equal strength and weaker horizontal bonds also of equal strength. The imbalance between pairs of colours on each dimer creates a Néel-like order because a dimer with dominant colours A, B is surrounded by dimers with dominant colours C, D as shown in (b).

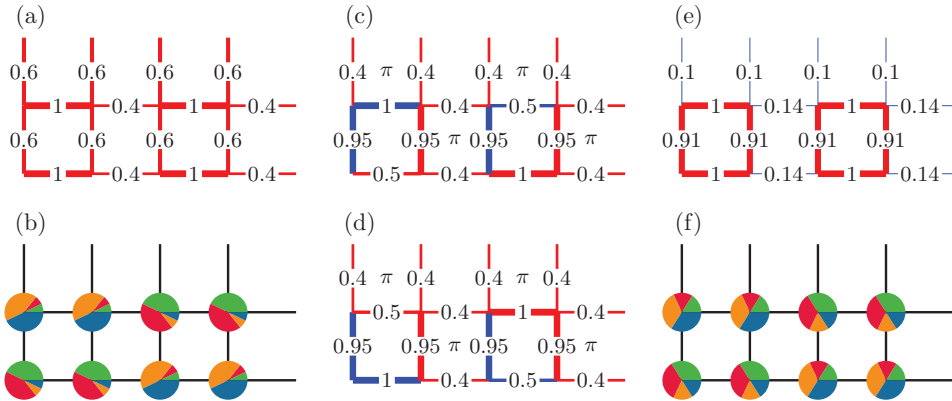


Figure 5.13 – Left: Schematic properties of the ground state of the $SU(4)$ $m = 1$ Heisenberg model. Center: Example of hopping parameters for the variational wave function that is expected to capture the ground state. Right: Results of the VMC simulation for the particular set of parameter shown in (c),(d). The colour code is the same for (a),(c),(d) and (e), the red (blue) bonds are negative (positive) and their width is proportional to the amplitude. For each bond the number refers to the ratio between the bond with maximal absolute value and its own. For (b),(f) the size of each sector is proportional to the colour occupation on that site.

After many empirical attempts to reproduce this type of state, a choice of parameter, like the one proposed in (c),(d) of FIG. 5.13, happened to capture the properties of this ground state as shown in (e),(f). In (c),(d) we see how the hopping terms are set and it should be emphasised that those two pictures represent two Hamiltonians, *i.e.* \hat{T}_a for (c) and \hat{T}_b for (d). The total variational Hamiltonian is then given by $\hat{T} = \hat{T}_a \oplus \hat{T}_a \oplus \hat{T}_b \oplus \hat{T}_b$ which mean that half of the

colours sees the strongest hopping term on different bonds than the other half. Indeed by comparing the horizontal hopping terms between (c) and (d), it should be noticed that they are not identical. This difference creates the colour occupation pattern given in (f). As for the variational Hamiltonian with on-site chemical potential, the use of different variational Hamiltonians for different colours induces a particular colour order. Of course the hopping terms given as an example in (c),(d) are not optimal. Actually, they are not creating a state for which the bond energies are like in (a). Nevertheless, the dimerisation on the horizontal bonds has been reproduced even if their energies are not correct, compare (a) and (e). This proof of concept, shows that this variational Hamiltonian should be able to capture colour ordered states like the expected ground state of the $SU(4)$ $m = 1$ Heisenberg model on the square lattice. The related variational wave function, which will be referred to as Néel wave function, depends on 31 free variational parameters (15 for \hat{T}_a and 16 for \hat{T}_b). This number has been reduced to 7 by taking into account some symmetries. For instance, the four sites on the left of the unit cell should be connected like the four sites on the right up to a point symmetry and \hat{T}_a should be related to \hat{T}_b by a mirror symmetry.

The Néel wave function has another feature that should be presented. There is a non-trivial flux configuration with π -fluxes in every two square plaquettes. The presence of a flux can dramatically change the variational energy because changing the flux configuration would require a change in the sign of least the one hopping term. It should therefore be checked whether this flux configuration is optimal or not. To achieve this, another variational wave function named flux wave function, needs to be tested. This wave function is defined on a (2×2) unit cell and has complex hopping terms which means that in the Hamiltonian (5.39), $t_{ST} \in \mathbb{C}$.

Like for the $k = 3$ and $k = 6$ cases, the optimisation of the wave functions has been performed by the PSO algorithm on a 64-site system with periodic boundary conditions to reduce as much as possible the finite size effects. On average more than 75 000 and 160 000 different variational parameters have been measured for respectively the Néel and flux wave function because the former wave function has less free parameters than the latter. The pictures in FIG. 5.14 represent the best solutions obtained by the PSO algorithm for the Néel (a)-(d) and flux (e)-(h) wave functions.

Interestingly the optimisation for both wave functions gives the exact same result for $m = 1$, this shows that the flux configuration chosen for the Néel wave function is pertinent. Unfortunately, this optimal Néel wave function does not favour the dimer phase nor the colour order because the hopping amplitude is maximal on two square plaquettes and hence $\hat{T}_a = \hat{T}_b$. For $m = 1$, the VMC method is not able to capture the colour ordered Néel-like state observed in reference [31] but reproduces the plaquette state selected by LFWT.

For $m > 1$, both wave functions give comparable energies. There is a slight preference for the flux wave function with a pattern of alternating $\pi/4$ and π fluxes. Even if the energy difference is bigger than the error bars, it is believed to be a finite size effect and the Néel wave function

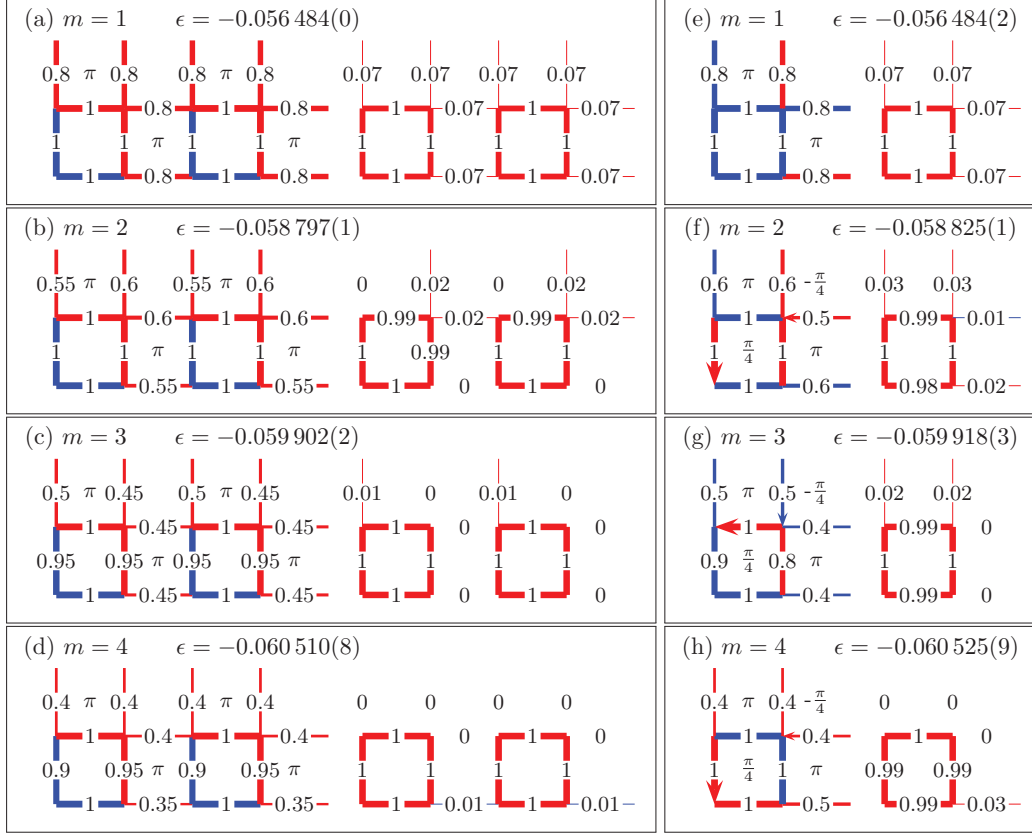


Figure 5.14 – The conventions used here are identical to the ones in FIG. 5.3. Optimal solution for $SU(4m)$ with $m = 1, 2, 3, 4$ found by the PSO algorithm for the Néel (left) and flux (right) wave functions. For the flux wave function, the arrows indicate the orientation of the $\pi/4$ phase.

should be favoured in the thermodynamic limit. Moreover the bond energy pattern is very similar and consist in both cases in square plaquette. This pattern corresponds to the VCS state expected in the mean-field limit [43], see FIG. 5.2.

Let us now see how the variational energies scale for the $SU(4m)$ Heisenberg model when m increases. The plot FIG. 5.15 summarises the best variational energies found by the PSO for the Néel and flux wave functions as well as the energies for the Fermi and chiral ones. The use of antiperiodic boundary conditions was required to avoid degeneracy at the Fermi level for the Fermi wave function but as the energy is very high, we do not expect this wave function to be competitive even for periodic boundary conditions. The chiral wave function is constructed such that there is a $\pi/2$ flux per square plaquette. Its energy is lower than the Fermi one but still higher than the Néel or flux ones. As presented earlier, the energies of the Néel and flux wave functions are very close and they cannot be distinguished on the plot FIG. 5.15. They both produce a plaquette state with the lowest variational energy found during this study. The linear fit shown for all wave functions recover the mean-field energy of the chiral and VCS states.

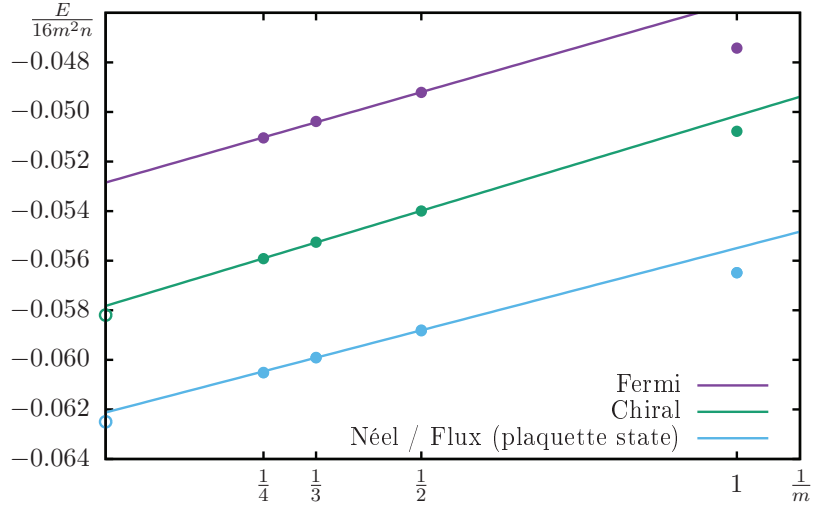


Figure 5.15 – The filled circles are variational energies for the $SU(4m)$ on a square lattice with 64 sites. The error bars are smaller than the symbols and periodic boundary conditions have been used for all but the Fermi wave function. The linear fit based on $m = 2, 3, 4$ extrapolates the energies to the mean-field limit. The empty circles are mean-field energies.

In summary, the attempt to recover an ordered state on the square lattice for $SU(3m)$, $SU(4m)$ or $SU(5m)$ with one particle per site is unsuccessful. None of the variational wave function is able to reproduce the expected ground state at $m = 1$. On the positive side, when $m > 1$, the variational results are in agreement with the mean-field solution.

5.5 Chapter summary

Thanks to an extensive use of the PSO algorithm, we were able to study the $SU(N)$ Heisenberg model for many fully antisymmetric irreps. The updated phase diagram FIG. 5.16, originally proposed by Hermele and Gurarie [44], summarises the new results obtained in this chapter.

For $k = 3$ the PSO algorithm has essentially found a 6-site plaquette state having a central bond with positive energy when $m > 2$. This state has the lowest variational energy and the larger m is, the stronger the plaquette becomes. For $m \rightarrow \infty$, this state reproduces faithfully the mean-field VCS state with a π flux in the rectangular plaquette. In the other limit, *i.e.* for $m = 1$, the attempt to recover the three-sublattice order failed and the lowest variational energy is reached by a chiral wave function with $2\pi/3$ flux per square plaquette. For $m = 2$, there is a competition between a columnar trimer state and the chiral one. Interestingly, this system, *i.e.* $SU(6)$ $m = 2$ seems to be a good candidate to stabilise a chiral phase.

For $k = 4$, the PSO has found a 4-site plaquette state which agrees with the mean-field VCS state when $m \rightarrow \infty$. This state has always the lowest variational energy so that for $m = 1$, the Néel-like state with colour order was not recovered.

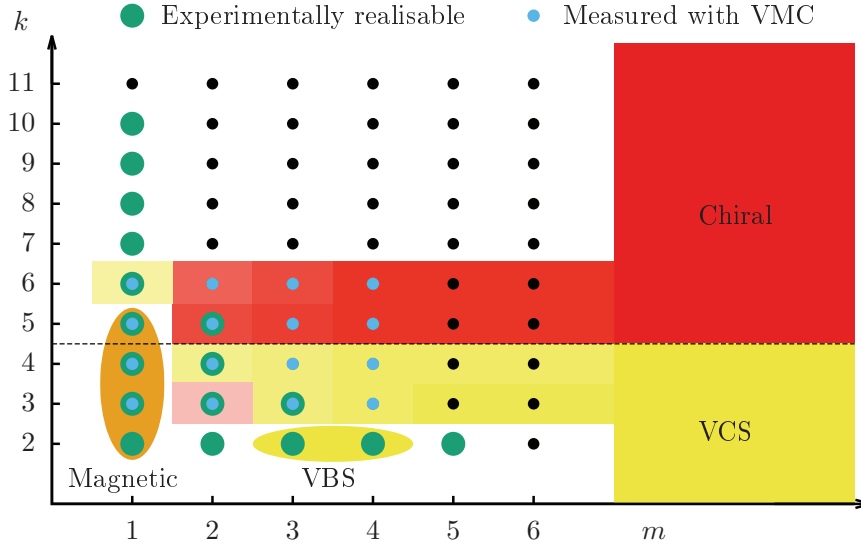


Figure 5.16 – Phase diagram of the $SU(N)$ Heisenberg model for all fully antisymmetric irreps. For $m = 1$ and $k = 2, 3, 4$, a magnetic order was already predicted and recent ED results showed that it may also be true for $k = 5$ (orange ellipse). Additionally there are some very recent LFWT results that predict a magnetic order for $k = m = 2$. For $k = 2$ and $m = 3, 4$, Assaad [35] predicted a VBS state using QMC. All other points for $m < 5$ are VMC results. The ground state is chiral (red) for $k = 5, 6$ and $m > 1$ and for $k = 3$ with $m = 2$. The VCS state (yellow) spans $2 < k < 5$ for all $m > 1$ but for $k = 3$. The shades of yellow or red indicate the energy difference between the two different variational states with lowest energy.

The ordered state for $SU(5)$ $m = 1$ was not recovered with the use of an on-site chemical potential. Nevertheless, the long range correlations computed with the Fermi wave function are in agreement with ED results. For $SU(5m)$ $m \geq 1$, the chiral state has a lower energy than the Fermi one and the extrapolation $m \rightarrow \infty$ matches the mean-field energy.

For $k = 6$, the best solution found by the PSO algorithm are a state consisting of stripes of dimers connected with uneven bonds and a state built with 6-site plaquettes having a central bond with negative energy. For this latter state, when $m \rightarrow \infty$, the central bond does not vanish as for $k = 3$. These plaquettes can therefore be seen as 6-site singlets constituting the rungs of decoupled ladders. These two states are in competition with a chiral state with a $\pi/3$ flux per square plaquette. According to the VMC results, the ground state is chiral for $m > 1$. Moreover the energies between the chiral and free wave functions are so close for $m = 1$, that it is difficult to conclude with certainty but the chiral wave function is believed to have a higher energy than the plaquette one.

Note that for $k = 3, 6$, the PSO algorithm has also been run for a (4×3) unit cell and same types of solutions as on the (3×2) were recovered. Finally, we saw during this study that any type of colour order is very hard to capture with this type of variational wave functions. Nevertheless, the VCS states predicted in the mean-field limit have all been recovered for $k < 5$. Moreover it is reasonable to assume that the chiral state is really favoured when $k \geq 5$ for $m > 1$.

6 Honeycomb lattice

In this chapter, our aim is to address the possibility to stabilise chiral phases in the context of the $SU(N)$ Heisenberg model on the honeycomb lattice. This model has been studied by Szirmai et al. [79] and Sinkovicz et al. [80] for $k \equiv N/m = 6$ in the mean-field limit where N and m tend to infinity keeping the ratio k fixed. They found a chiral ground state with $2\pi/3$ flux per hexagonal plaquette, and two plaquette states with higher energies: the $0\pi\pi$ plaquette in which each 0 flux plaquette is surrounded by π flux plaquettes, and a 000 plaquette phase in which hexagons are completely decoupled. However, a recent work [26] done on the same lattice for $SU(6)$ in the fundamental irrep has given strong evidence in favour of the $0\pi\pi$ plaquette ground state over the chiral one with $2\pi/3$ flux. This irrep corresponds to a physical model with $m = 1$ particle per site for which (1.45) reduces to the simple permutation Hamiltonian (1.46):

$$\hat{H}_{\hat{P}} = \sum_{\langle i,j \rangle} \hat{P}_{ij} \quad (6.1)$$

It was also shown in reference [26] that the chiral phase can be stabilised by adding a ring-exchange term:

$$\hat{H}_{\square} = i \sum_{\square} (\hat{P}_{\square} - \hat{P}_{\square}^{-1}) \quad (6.2)$$

to the Hamiltonian. Indeed the authors studied the stability of the plaquette ground state of the following Hamiltonian:

$$H_{\theta} = \cos(\theta) \hat{H}_{\hat{P}} + \sin(\theta) \hat{H}_{\square} \quad (6.3)$$

starting from the pure Heisenberg model ($\theta = 0$). Using a combination of ED, VMC based on Gutzwiller projected wave functions and iPEPS, they showed that a transition occurs between the plaquette and chiral state for a finite value of θ . Note that plaquette and chiral states can easily be distinguished experimentally by their very different signatures in the spin structure factor [79, 80].

Here we explore another path to the possible stabilisation of a chiral phase for the $SU(N)$ Heisenberg model. Instead of adding a ring-exchange term, we increase the number of particles per site m for $k = 6$, and we study fully antisymmetric irreps on each site labelled by a Young tableau with m boxes in one column. In the following, our goal is to investigate how the system evolves between the chiral ground state of reference [79] for $m = \infty$ and the $0\pi\pi$ plaquette ground state of reference [26] obtained for $m = 1$. We will present numerical results that give strong indication that the chiral phase is stabilised for $m > 1$.

6.1 Variational wave functions

As for the previous systems, we intend to use the VMC algorithm to study the $SU(N)$ Heisenberg model on the honeycomb lattice. To have meaningful results we need to define a representative set of variational wave functions. Following other papers [25, 26] and inspired by the mean-field results [79], we have tested five different variational wave functions represented in FIG. 6.2, one chiral and four plaquette states.

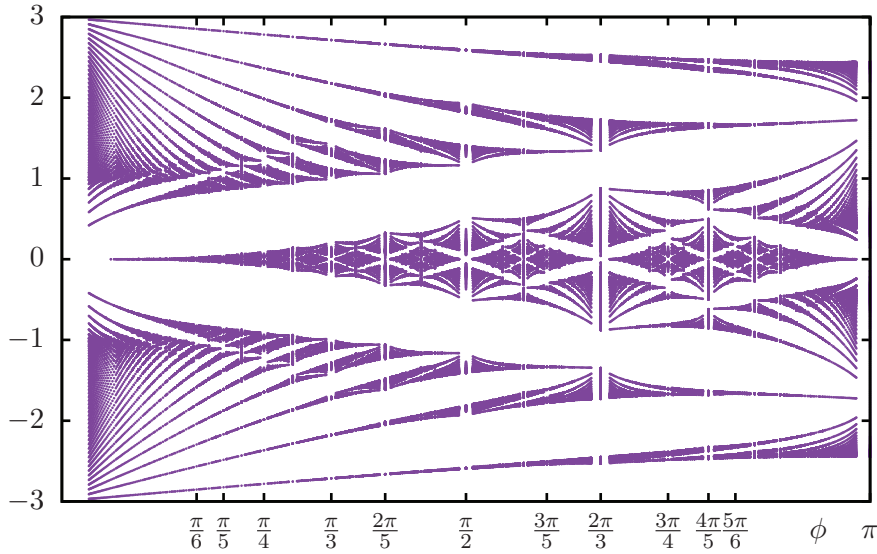


Figure 6.1 – Hofstadter butterfly for the honeycomb lattice. The spectrum is given in function of $\phi = p\pi/q$, $p \leq q \in \mathbb{N}$.

The chiral wave function is the only one having no variational parameter. It has uniform hopping amplitudes but non-uniform phase factors that creates a homogeneous flux of $2\pi/3$ per hexagonal plaquette. This wave function does not break the lattice symmetry but breaks the time reversal one. The wave function created with this particular flux has the largest gap at the $1/6$ filling. This can be observed in FIG. 6.1, where the spectrum is plotted for a large range of flux. For instance for $\phi = \pi/6$, the first two bands need to be filled and the gap is small compared to the gap at $\phi = 2\pi/3$, where only the lowest band must be filled.

We want the other wave functions to preserve the time reversal symmetry, therefore the only allowed fluxes are 0 and π . To preserve the rotation symmetry, and since we chose unit cells containing at most 12 sites, there are only 4 non-equivalent flux configurations. Two of them have already been introduced, $0\pi\pi$ and 000 , while the other two are: $\pi 00$ consisting of a central hexagon with π flux surrounded by 0 fluxes and $\pi\pi\pi$ having a homogeneous π flux in each hexagon. Due to the simplicity of the chosen flux configurations, there are only two meaningful variational parameters, t and t_d : the hopping terms around the central hexagons t , and the hopping terms linking these hexagons t_d . Using additional hopping terms would break other symmetries, for instance having different hopping terms around the central hexagon would break the rotational symmetry. Since the honeycomb lattice is bipartite, only the relative sign of t_d and t matters, therefore, for the plaquette wave functions, we have a single variational free parameter, the ratio t_d/t with fixed $t = -1$.

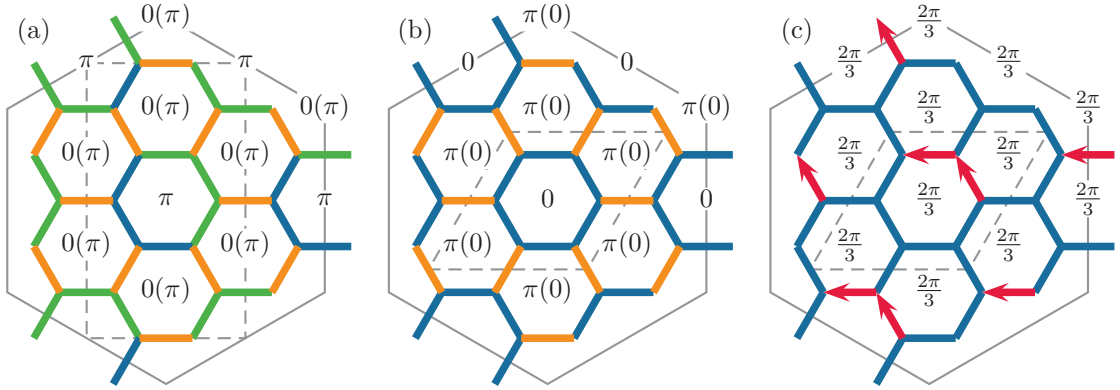


Figure 6.2 – Representation of the five wave functions with their unit cell (dashed lines) on a 24-site cluster with periodic boundary conditions. (a)-(b) Plaquette wave functions, where blue and green bonds are respectively t and $-t$, while the yellow ones are t_d . By changing the sign of the ratio t_d/t from negative to positive, the flux configuration of the wave function will change from $\pi 00$ to $\pi\pi\pi$ in (a) and from $0\pi\pi$ to 000 in (b). (c) Chiral wave function for which the hopping terms are given by $t_{ij} = t e^{i2\pi/3} = t_{ji}^*$ between the sites i and j connected by a red arrow and by t otherwise. The flux per plaquette is defined mod 2π .

6.2 Results

In this section, results on a 72-site cluster with antiperiodic boundary conditions will first be presented. Then a finite size analysis on a representative example, $m = 3$, will show how accurately the thermodynamic energies can be extracted. This accuracy allows us to draw conclusions on how the VMC recovers the mean-field limit and gives new indications of a chiral phase for $m > 1$.

FIG. 6.3 shows the variational energies as a function of m for different values of the ratio t_d/t for all different wave functions on a 72-site cluster with antiperiodic boundary conditions. This particular choice of boundary conditions allows us to measure the energy for $t_d/t = -1$ because it lifts the well-known degeneracy at the Fermi level, an important requirement to

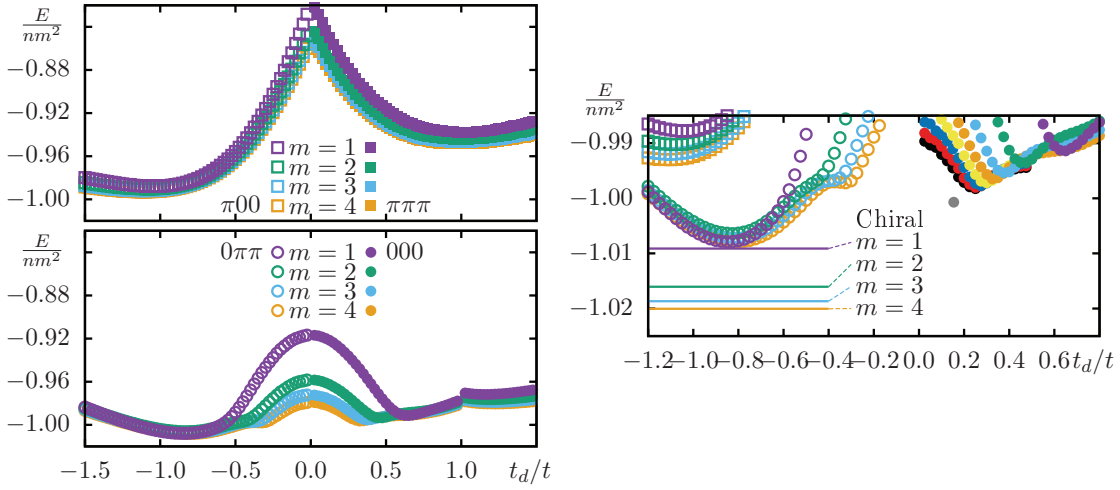


Figure 6.3 – Energy per site for a cluster of 72 sites. The left plots are given on the same scale to allow better comparison while the right plot is a zoom around the minima. The colour code is the same for all wave functions and error bars are smaller than the symbols. Upper left plot: The empty and filled squares indicate the energy of the $\pi 00$ and $\pi \pi \pi$ wave function respectively. Lower left plot: The empty and filled circles indicate the energy of the $0 \pi \pi$ and 000 wave function respectively. Right plot: All wave functions are shown together. The energies of the chiral wave functions are represented with straight lines. Additional values for the 000 wave function for $5 \leq m \leq 8$ have been included. The grey filled circle corresponds to the minimal energy for the 000 wave function obtained by extrapolation in the limit $m \rightarrow \infty$. For larger systems, the extrapolated value of t_d/t for the 000 wave function tends to zero, as it should since the mean-field result corresponds to isolated plaquettes, see FIG. 6.4.

construct Gutzwiller projected wave functions. However, it does not lift the degeneracy for the value $t_d/t = 1$. The other missing energy is for $t_d/t = 0$ because the VMC fails to find a well defined starting configuration, since all hexagons are disconnected, see appendix B.3. On the right plot, the chiral energies are also shown as straight lines. We can see that each plaquette wave function has at least one local minimum. While the exact position of the minima does not really matter, it is interesting to note that for all wave functions but the 000 one, the minima stay roughly stable. Indeed, we know that the 000 mean-field solution consists of disconnected hexagons with 0 flux. This solution is expected to be captured by the 000 variational wave function, when m is going to infinity for a small value of t_d/t . This is indeed what can be observed in the right plot of FIG. 6.3: the position of the 000 minimum moves to the left when m increases but the value of its energy remains higher than the energy of both the $0 \pi \pi$ and the chiral wave function. By looking more carefully at the energies of the chiral and $0 \pi \pi$ wave functions, it seems that the former becomes lower when m increases and the latter remains stable. This behaviour is the most interesting feature of this analysis on a 72-site cluster. Indeed, there is a strong competition between the chiral and $0 \pi \pi$ wave functions when $m = 1$ but for $m > 1$ the energy of the chiral wave function becomes clearly lower.

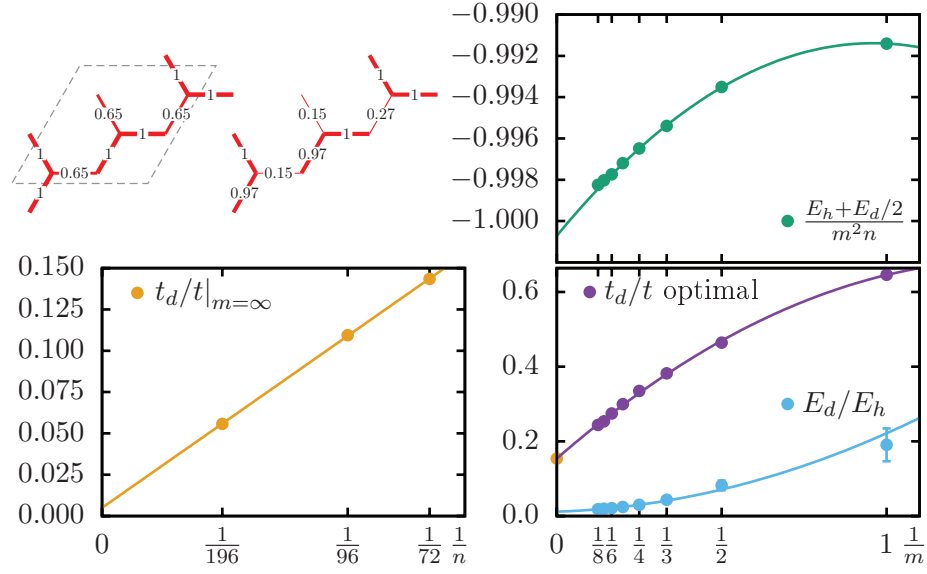


Figure 6.4 – Upper left panel: The pictures represent the hopping amplitude (left) and the bond energy (right) obtained by VMC inside the unit cell shown in FIG. 6.2 (b). All values are negative and their absolute value is shown by the width of the lines and by a number proportional to the maximal absolute value. The right picture shows the difference in energy between the strong bonds building the hexagonal plaquettes (E_h) and the weak ones connecting them (E_d). Right panels: $1/m$ evolution of the energy $E = E_d + 2E_h$ (above), the optimal parameter (below, purple) and the energies ratio between the strong and weak bonds (below, blue) for a 72-site system. The function $f(x) = ax^2 + bx + c$ fits the data with continuous lines. Lower left: Evolution as a function of the system size of the optimal variational parameters extrapolated in the mean-field limit. The straight line extrapolates this value to the thermodynamic limit.

As we saw, the 000 wave function is supposed to capture the mean-field solution when $m \rightarrow \infty$. In the plot FIG. 6.4, we study more carefully the evolution of this wave function when m increases. The right picture of upper left panel shows that the strong bonds with energy E_h and forming the hexagonal plaquette are coupled together with bonds of energy E_d which are on average five times weaker. The small anisotropy (0.15 vs 0.27) is due the antiperiodic boundary conditions and should disappear in the thermodynamic limit. The energy of this state is given in the upper right panel for $m = 1$. This panel shows also how the variational energy evolves when m gets larger. To obtain these energies, one needs to find the optimal variational parameter for each m . These values are then reported in the lower right panel, where we can see how they evolves with m . The extrapolation to $m \rightarrow \infty$ of this parameter and its related energy corresponds to the grey point in FIG. 6.3. Even if the lower right plot confirms that the ratio of the energy between the weak and strong bonds vanishes in that limit, which shows that the hexagons are decoupled, one might be concerned to see a non-zero optimal variational parameter. Indeed the VMC algorithm should recover the mean-field results for large m and the variational parameter should therefore be zero. To get this results, one needs to get rid of the finite size effect by going to larger system. The lower left plot of FIG. 6.4 shows that the mean-field optimal variational parameter goes to zero in the thermodynamic limit.

The same study has been done for larger clusters (up to 288 sites) and the energies in the thermodynamic limit have been extrapolated. As an example, FIG. 6.5 shows the variational energies as a function of the system size for $m = 3$. It is clear that the chiral wave function gives lower energies than any of the plaquette ones no matter what the size of the system is.

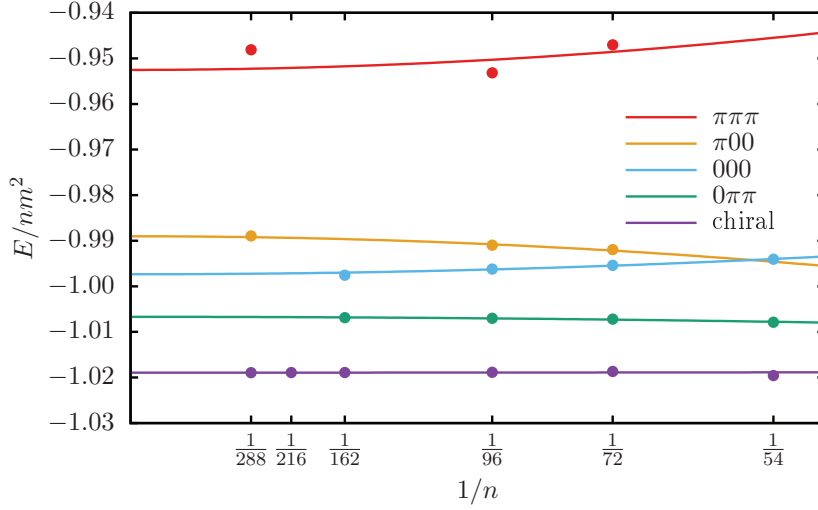


Figure 6.5 – Finite size scaling for $m = 3$. The function used for the fit is of the type $f(x) = ax^2 + b$ for all data sets. For some system sizes, some values are missing. This is due to a degeneracy at the Fermi level. The error bars on the points are smaller than the symbols.

The results shown in FIG. 6.6 are the energies extrapolated in the thermodynamic limit. Let us first focus on already published results for the case with $m = 1$. The chiral and $0\pi\pi$ wave function are in strong competition as already visible in FIG. 6.3. It was numerically concluded on the basis of extensive ED, VMC and iPEPS calculations [26] that the ground state is the $0\pi\pi$ plaquette state. In the context of our calculation, where we only calculate the energy of a single wave function, the chiral state turns out to have a slightly lower energy, but as shown in reference [26], if several variational wave functions with different boundary conditions are coupled, this small energy difference is reverted in favour of the plaquette phase.

As soon as $m = 2$, the energy of the chiral wave function becomes much lower than the energy of any plaquette wave function, with an energy difference of the same order of magnitude than that of the $m \rightarrow \infty$ case. Moreover, this difference increases for larger values of m . The results for $m > 1$ can be fitted linearly in $1/m$, and the slope of the fit of the chiral wave function energy is bigger than that of the plaquette wave function. Let us note that the extrapolations of the fits to the limit $m = \infty$ of the three lowest states (chiral, $0\pi\pi$ and 000 plaquettes) agree with the mean-field energies [79], a good test of the validity of our VMC simulations.

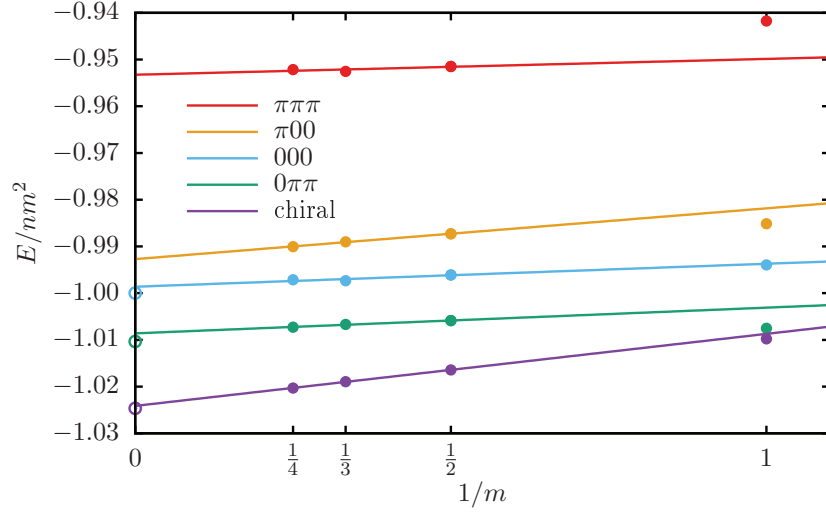


Figure 6.6 – Energies per site obtained by VMC in the thermodynamic limit for different irreps. They are fitted by a line based on $m = 2, 3, 4$ to show the agreement with the empty circles which are the mean-field results [79] valid for $m \rightarrow \infty$.

6.3 Chapter summary

We have shown in the context of the $SU(N)$ model on the honeycomb lattice with $N = 6m$, where m is the number of particles per site, that the presence of chiral order in the mean-field limit ($m \rightarrow \infty$) is representative of finite values of m down to $m = 2$. From that point of view, the case $m = 1$ with its plaquette ground state appears as an exception. This is an interesting step forward towards the stabilisation of chiral order in a simple Heisenberg model with only nearest neighbour permutation and no ring-exchange term. The first candidate in order of increasing N is $SU(12)$ $m = 2$. It is still too large to be realised with alkaline rare earths, which are limited to $N \leq 10$, but very close. This result suggests that a systematic investigation of $SU(N)$ models with $N \leq 10$ for all compatible values of m (i.e. values of m that divide N) and different lattice geometries might indeed reveal a case of chiral order that could be stabilised with alkaline rare earths and only nearest-neighbor permutations.

7 Triangular lattice

The triangular lattice has mostly been studied for the $SU(3)$ $m = 1$ case. For instance Bauer et al. [28] looked for the ground state with DMRG, iPEPS and LFWT. They found a three-sublattice ordered state which is in agreement with another variational study [29]. It is already known from the study on the square lattice that colour ordered states are difficult to capture with VMC. Nevertheless, we will use this method to extend the discussion of the phase diagram for $SU(3m)$. The cases $m > 1$ have only been investigated by mean-field methods and for $k = 3$ the ground state is known to be a k -simplex VCS state [44]. This state saturates the bond and each site belongs to one triangular plaquette which is in a singlet state. All plaquettes are decoupled from each other and can point in any direction. This state has an energy given by:

$$\epsilon_{kVCS} \equiv \frac{E_{MFS}^{kVCS}}{JN^2n} = \frac{1-k}{2k^2} = -\frac{1}{9} = -0.\bar{1} \quad (7.1)$$

In the following, we will make the connection between the $m = 1$ case and the mean-field solution by studying different wave functions with the VMC algorithm. We will separately analyse each variational wave function to finally compare them. In order to avoid finite size effects, all results that will be shown are computed on a system with 324 sites and antiperiodic boundary conditions. It has been checked that the general behaviour is qualitatively equivalent for smaller systems, *i.e.* $n = 36, 144$.

7.1 Individual wave function analysis

As the triangular lattice is not bipartite, the relative sign of the hopping amplitude in the variational Hamiltonian (2.10) matters. The wave functions that will be introduced below, will be defined with one variable fixed to $t = -1$ which will therefore not be considered as a variational parameter. This sets the energy scale and sign reference.

7.1.1 Chiral wave function

Like it has been shown for the square lattice, the mean-field solution of this state can be computed. The formula (5.35) can be used directly, if one takes into account the correct coordination number. On the triangular lattice, there is three times more bonds than sites, therefore the mean-field energy is given by $\epsilon_\chi = -3|\tilde{\chi}|^2$, where $\tilde{\chi}$ is fixed by (5.30). To proceed to the numerical computation of this energy, the definition of a unit cell has to be provided. There are many different unit cells that allow the presence of a homogeneous flux ϕ per triangular plaquette. The one presented in the top panel of FIG. 7.1 is convenient to construct wave functions with any given flux $\phi = p\pi/q$, $p \leq q \in \mathbb{N}$. It has basis vectors $\mathbf{a} = (k, 0)$ and $\mathbf{b} = (1/2, \sqrt{3}/2)$. If the sign of all hopping terms is inverted, *i.e.* $\chi \rightarrow -\chi$, then the flux per triangle goes from $\phi \rightarrow \phi - \pi$, while the spectrum is inverted $E_k \rightarrow -E_k$ because of (5.19). This implies a particular point symmetry around $(0, \pi/2)$ in the Hofstadter butterfly shown in the lower panel of FIG. 7.1.

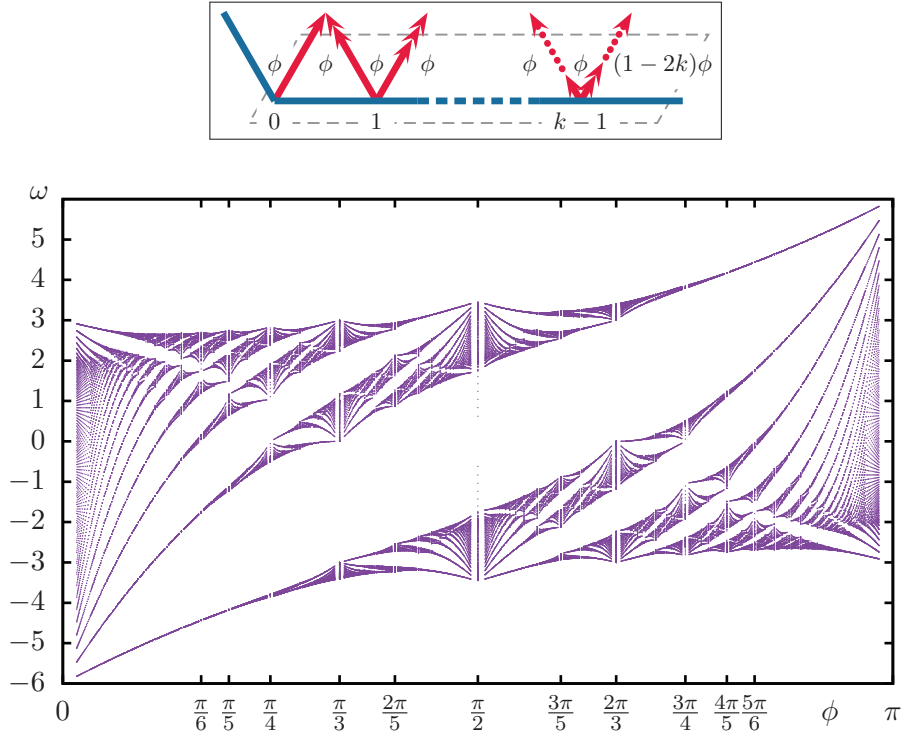


Figure 7.1 – Top panel: Schematic representation of the χ_{ij} on a triangular lattice. The dashed gray parallelogram represents the unit cell with k sites. The colourful lines are the links connecting different sites of the lattice. The blue links take the value $\chi \in \mathbb{R}$, while the red arrows take the value $\chi e^{is\phi}$, where s denotes the site index in the unit cell. The value of the phase is also symbolised by the number of heads per arrow. Each plaquette contains a flux of ϕ or equivalently $(1 - 2k)\phi = \phi - 2\pi$. Lower panel: Hofstadter butterfly for the triangular lattice computed using the unit cell depicted above. The spectrum is given for a wide range of flux per triangular plaquette $\phi = p\pi/q$, $p \leq q \in \mathbb{N}$.

7.1. Individual wave function analysis

m	1	2	3	4	∞
$\pi/3$	-0.05086(3)	-0.07240(2)	-0.08102(3)	-0.08554(3)	-0.099917
$2\pi/3$	0.01575(2)	-0.02094(2)	-0.03379(2)	-0.04029(2)	-0.060400

Table 7.1 – Comparison of the energies given by the chiral wave function with a flux of $\pi/3$ and $2\pi/3$ for the $SU(3m)$ Heisenberg model on the triangular lattice. The first columns show the variational energies obtained for a system of 324 sites with antiperiodic boundary conditions, while the last one displays the exact mean-field energies.

For $k = 3$, $\phi = \pi/3$ and $\phi = 2\pi/3$ are the two flux candidates, they both require a unit cell containing 3 sites and are related by the point symmetry discussed before. At the mean-field level, the energy of the chiral wave function when $\pi/3$ is clearly lower, see the last column of table TAB. 7.1. This is due to the larger gap separating the filled band from the empty ones when $\phi = \pi/3$. We therefore expect that the chiral variational wave function with the flux $\pi/3$ will also give a lower variational energy than with $2\pi/3$. This is confirmed in the first columns of the table TAB. 7.1 which show the energies obtained with VMC for $m = 1, 2, 3, 4$. The wave function used in the VMC algorithm was constructed using the unit cell in FIG. 7.1 for $k = 3$. As for the square lattice the variational Hamiltonian (5.39) can be used:

$$\hat{T} = \sum_{\langle i,j \rangle} t_{ij} \hat{c}_i^\dagger \hat{c}_j + \text{h.c.} = \sum_{\mathbf{m}} \sum_{s=0}^{k-1} \sum_{\tau \in \{1,2,3\}} t_{s\tau} \hat{c}_{\mathbf{m}s}^\dagger \hat{c}_{\mathbf{m}s+\tau} + \text{h.c.} \quad (7.2)$$

where the bond τ goes in the three directions and s indexes the site inside the unit cell at position \mathbf{m} . All hopping terms $t_{s\tau}$ must have the same amplitude $|t_{s\tau}| = t$. The horizontal ones can be real, while the diagonal ones carry a phase:

$$t_{s\tau} = \begin{cases} t & \text{if } \tau = 1 \\ t e^{i(2s+1)\phi} & \text{if } \tau = 2 \\ t e^{i2s\phi} & \text{if } \tau = 3 \end{cases} \quad (7.3)$$

7.1.2 Three sublattice colour-ordered wave function

In an attempt to recover the three-sublattice ordered ground state for $m = 1$ [28, 29], we used an on-site chemical potential depending on the colour. Using the same type of variational Hamiltonian as for the square lattice (5.40):

$$\hat{T}_a = \sum_{\mathbf{m}} \sum_{s=1}^{n/M} \left(t \sum_{\tau \in \{1,2,3\}} \left(\hat{c}_{\mathbf{m}s}^\dagger \hat{c}_{\mathbf{m}s+\tau} + \hat{c}_{\mathbf{m}s+\tau}^\dagger \hat{c}_{\mathbf{m}s} \right) + \mu \delta_{sa} \hat{c}_{\mathbf{m}s}^\dagger \hat{c}_{\mathbf{m}s} \right) \quad (7.4)$$

The chemical potential pattern is most easily understood by looking at the left picture of FIG. 7.2 which illustrates an example for $SU(3)$ $m = 1$ on a 27-site system. To obtain the picture on the right, we performed an optimisation for $SU(3)$ $m = 1$ on the variational parameter μ/t . We ran the VMC simulations for a variational parameter in the range $[-1, 2]$ for each

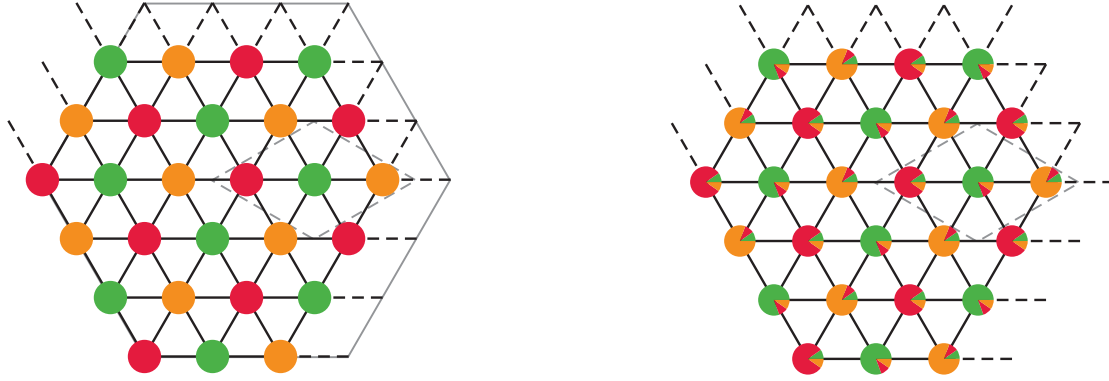


Figure 7.2 – Left panel: The colour of the circles represents the location of the non-zero on-site chemical potential for a given T_a . The different colours represent the different variational Hamiltonians T_a . The chemical potential pattern distinguishes three equivalent sublattices. Right panel: On each site, the pie chart represents the occupation number for each colour obtained by VMC for SU(3) $m = 1$ on a system with 324 sites and antiperiodic boundary conditions with the optimal variational parameter of $\mu/t = 0.975$.

step of 0.025 and found that the optimal one was at $\mu/t = 0.975$. We then computed the occupation number for each colour and for each sites of the unit cell for this value of μ/t . The occupation numbers are then represented by pie-chart on each site of the lattice. Thanks to this occupation number, the local moment defined as:

$$\langle m \rangle = \frac{3}{2} \max_{\alpha} \langle \hat{c}_{i\alpha}^{\dagger} \hat{c}_{i\alpha} \rangle - \frac{1}{2} \quad (7.5)$$

can be computed. Bauer et al. [28] found a local moment in the range $\langle m \rangle \in [0.43, 0.6]$, while this VMC simulation gives $\langle m \rangle \approx 0.7$. This variational wave function clearly reproduces the three-sublattice colour order despite overestimating the local moment.

Let us now present why $\mu/t = 0.975$ is the optimal parameter for $m = 1$ and what the other optimal solutions for $m > 1$ are. The left plot of FIG. 7.3 displays the energy of this variational wave function as a function of the ratio μ/t . For $m = 1$, it clearly shows that the energy reaches a minimum at $\mu/t = 0.975$. This plot allows us to distinguish the cases $m = 1, 2$, where the energy reaches its minimal value for a non zero variational parameter μ/t , from the cases $m = 3, 4$, where the minima are at $\mu/t = 0$.

On the same plot, there is another interesting feature that is worth commenting. We can observe discontinuities for some values of μ/t . These discontinuities are due to bands crossings and finite size effects. To understand this, let us focus on the most obvious discontinuity that occurs just after 0.825. The right plot of FIG. 7.3 shows the band structure of the variational Hamiltonian (7.4) for different values of μ/t . The eigenvectors selected to build the variational wave function are related to the lowest eigenvalues. The variational Hamiltonian is invariant for any unit cell translation because it commutes with the translation operator. The eigenvectors of the variational Hamiltonian are therefore also eigenvectors of the translation operator

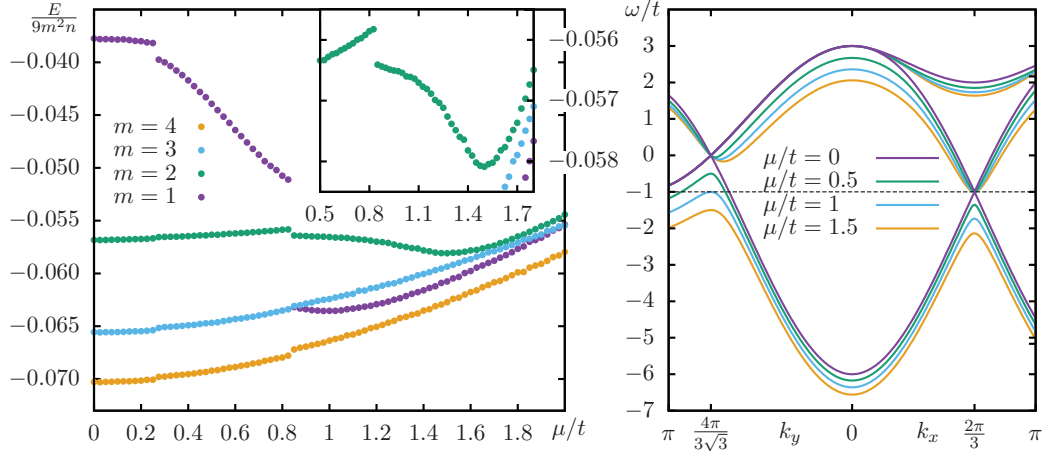


Figure 7.3 – Left panel: Energies for different m given as a function of the on-site chemical potentials obtained by VMC for a system of 324 sites with antiperiodic boundary conditions. The inset is a zoom around the minima for $m = 2$. The error bars are smaller than the symbol size. Right panel: The spectrum of (7.4) is composed of three bands and is given for different values of μ/t . The dashed line shows the energy where a gap opens when $\mu/t > 1$. We present only two cuts in the Brioullin zone, one cut keeps $k_x = 0$ (left) and the other keeps $k_y = 0$ (right).

with eigenvalues related to the quantum numbers $\mathbf{k} = k_1 \tilde{\mathbf{a}} + k_2 \tilde{\mathbf{b}}$ where $\tilde{\mathbf{a}}$ and $\tilde{\mathbf{b}}$ are the basis vectors of the reciprocal space. After diagonalisation, the variational Hamiltonian for a given colour can be expressed with operators indexed by those quantum numbers:

$$\hat{T} = \sum_b \sum_{\mathbf{k}} \omega_{b\mathbf{k}} \hat{f}_{b\mathbf{k}}^\dagger \hat{f}_{b\mathbf{k}} \quad (7.6)$$

with $\omega_{b\mathbf{k}} < \omega_{b+1\mathbf{k}}$ and b is the band index. Filling the energy levels with different \mathbf{k} leads to different states. For $\mu/t > 1$, as the lowest band is below the horizontal dashed line shown in the right plot of FIG. 7.3, only the lowest band will be occupied. This implies that all quantum numbers \mathbf{k} appear once. Below this limit, the first band is not fully filled and the second or third band will have some occupied states and hence some quantum numbers \mathbf{k} will be present more than once. As the quantum numbers for the impulsion are good quantum numbers, in the sense that they survive the Gutzwiller projection because it commutes with the translation operator, we can index the variational wave functions with quantum numbers \mathbf{k} . The variational states for $\mu/t < 1$ and $\mu/t > 1$ will have different quantum numbers and might be drastically different. This explains why the variational energy is discontinuous. For $\mu/t > 1$, a gap opens in the band structure forcing all states to occupy the lowest band and the variational energy is smooth because the quantum numbers indexing the variational wave function do not change. As we are dealing with finite-size systems, only a discrete set of impulsions are possible and they are equally spaced in the Brioullin zone. In this context, all the occupied states may belong to the lowest band for $\mu/t < 1$. By taking different system sizes, the position of this discontinuity moves but will never go above $\mu/t = 1$.

7.1.3 Plaquette wave function

For $k = 3$, the mean-field solution on the triangular lattice given by Hermele and Gurarie [44] predicts a k -simplex VCS state built with decoupled triangles. As the orientation of the triangles does not affect the mean-field energies but can be decisive for finite m , we have selected two different k -simplex VCS states. One has all triangular plaquettes pointing upward and the other has half of them pointing upward and half downward. The variational wave functions, $(\Delta\Delta, \phi)$ and $(\Delta\nabla, \phi)$, that are expected to capture the physics of these states are depicted in the figures FIG. 7.4.

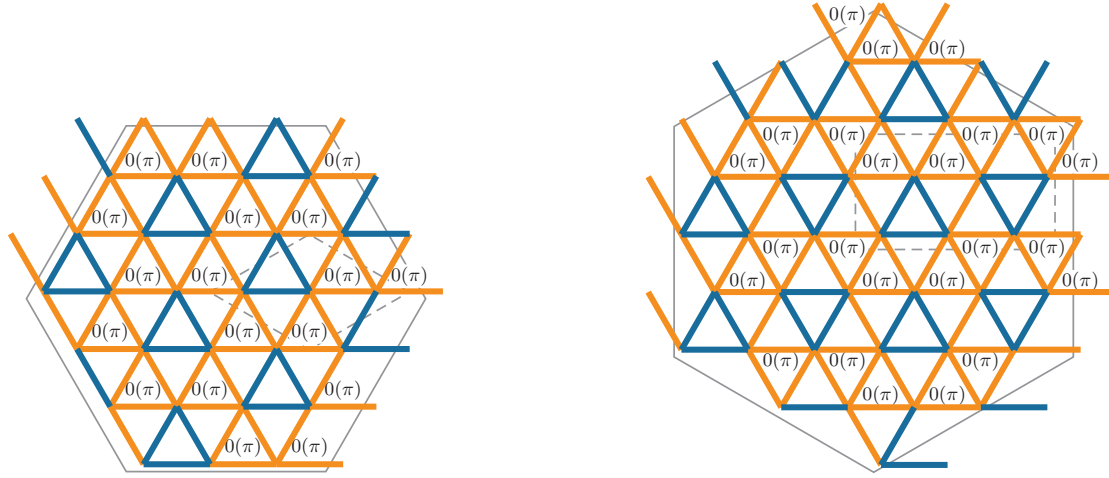


Figure 7.4 – The blue bonds have a hopping amplitude t , while the yellow ones have t_d . By changing the sign of t_d/t from positive to negative, some flux ϕ inside some triangles goes from 0 to π as indicated. The $(\Delta\Delta, \phi)$ and $(\Delta\nabla, \phi)$ wave functions are defined on a 3-site and 6-site unit cell represented by the gray dashed rhombus and rectangle. They can be accommodated on respectively the 27-site and 36-site system shown on the left and right.

Now that these two plaquette wave functions have properly been described, let us look at the results obtained by VMC, see FIG. 7.5. The energies are given as a function of the variational parameter t_d/t for $m = 1, 2, 3, 4$. The left part of the plot corresponds to the wave functions with a π -flux inside some triangular plaquettes, while the right one corresponds to the 0-flux wave functions. Before analysing the data, two comments on the measured parameters are required. The energy has been measured for all values of the variational parameter $t_d/t \in [-1.5, 1.5]$ with a step of 0.025, but some values around 0 are missing. This is due to the usual problem, when one wants to initialise the VMC algorithm with a wave function that only allows few configurations, see B.3 for more information. We also see some discontinuities in the energy which have the same origin as the one explained in 7.1.2.

Let us analyse more carefully the results for $m = 1$ because the same conclusions can be drawn for $m > 1$. We see that there are four local minima, one for each wave function and flux configuration. Thanks to the guides to the eyes, it is clear that the wave function $(\Delta\Delta, \pi)$ reaches the lowest energy for $t_d/t = -0.65$. This wave function with a π -flux pattern and all

triangles pointing upward is preferred over the three other options. For larger values of m , the same wave function is favoured, but the competition with the other ones gets stronger. This behaviour is expected because in the mean-field limit, the ground state is a k -simplex VCS state for which the orientation of the triangles and flux configuration do not matter.

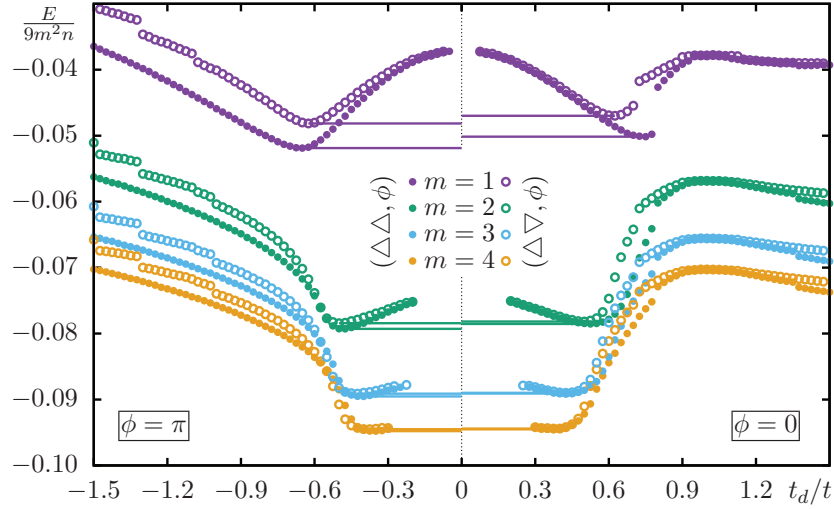


Figure 7.5 – Variational energies with the plaquette wave functions given as a function of the variational parameter t_d/t for a system with 324 sites and antiperiodic boundary conditions. For each values of m , the filled circles stand for $(\Delta\Delta, \phi)$, while the empty ones represent $(\Delta\nabla, \phi)$. In the left part of the plot $\phi = \pi$, while in the right part $\phi = 0$. The horizontal lines are a guide to the eyes to simplify the comparison of the energies between the different minima. The error bars are smaller than the symbol size.

The upper panels of FIG. 7.6 displays in one unit cell the bond energy of the four plaquette wave functions at their optimal variational parameters for $m = 1$. There is no relevant difference in the bond energies between the $(\Delta\Delta, 0)$ and $(\Delta\Delta, \pi)$, all positive bonds connecting triangular plaquettes have the same amplitude. Between the two other wave functions, namely $(\Delta\nabla, 0)$ and $(\Delta\nabla, \pi)$, we can observe a difference in the energy of the diagonal bond connecting the plaquettes horizontally. For the $(\Delta\nabla, \pi)$ wave function this energy is 10 times smaller than the one connecting the sites within a triangular plaquette, while for $(\Delta\nabla, 0)$ it is only 4.5 times smaller. It is also worth studying the evolution of the bond energies, when m gets larger. The lower plot of FIG. 7.6 shows the evolution of the ratio between the positive and negative bonds. As it was observed in the upper panels, this ratio is within $[0.23, 0.27]$ for $m = 1$ and all plaquette wave functions. It is clear that for $m > 1$, this ratio decreases and the energy of the bonds coupling the plaquettes vanishes in the mean-field limit. This proves that the k -simplex VCS state is well captured by any of the variational wave functions, when m is large enough.

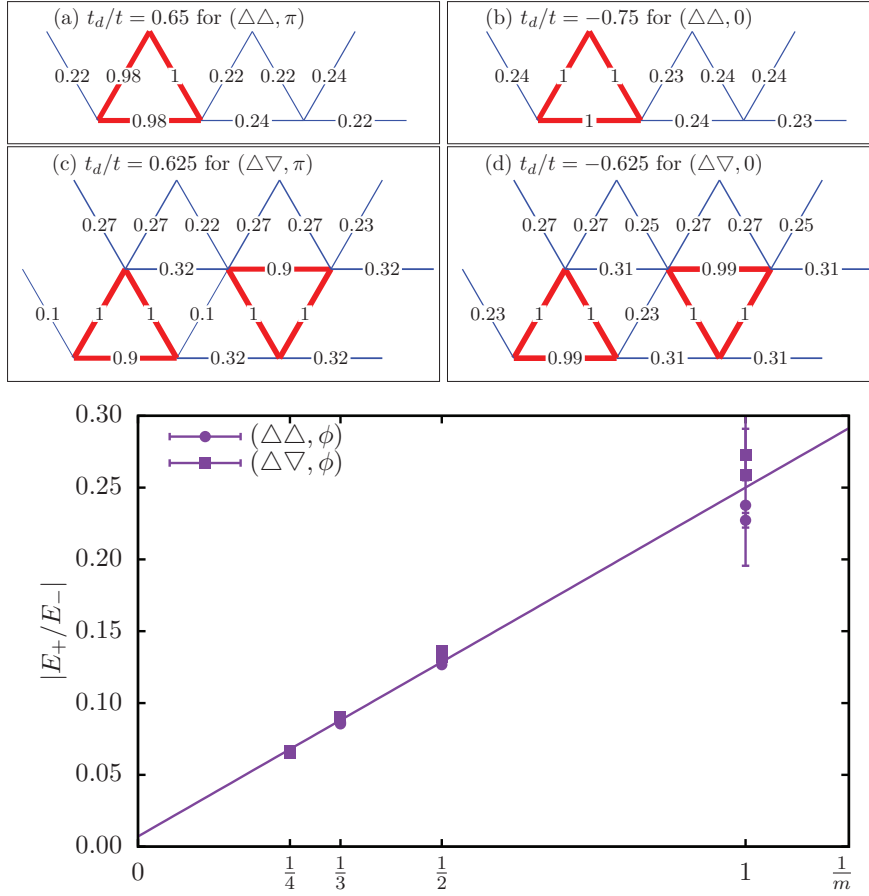


Figure 7.6 – Upper panels: Energy per bond obtained by VMC for a system with 324 site and antiperiodic boundary conditions. The red (blue) bonds have a negative (positive) energy. Their strength is indicated by their width and a number proportional to the strongest bond. Lower plot: Evolution as a function of $1/m$ of the ratio between the bonds with positive and negative energy. The line is a linear fit extrapolating this ratio for infinite m .

7.2 Chapter summary

At this stage, we have introduced the important variational wave functions and the optimal variational parameters have been found. The natural following step is to compare the energies of each wave function at their optimal solution. This is what the plot FIG. 7.7 shows for $m = 1, 2, 3, 4$, where we see the optimal energy for all wave functions.

It was already known that the ground state for the $m = 1$ presents a three-sublattice order. The VMC method provides an additional evidence and reproduces the three-sublattice ordered ground state observed in reference [28]. This shows that the use of an on-site chemical potential is able to capture this type of order. Nevertheless, the variational energy and the local moment obtained are approximately 15% too high. These two overestimations confirm that the particles are “frozen” even if the colour order is correctly reproduced. The chemical

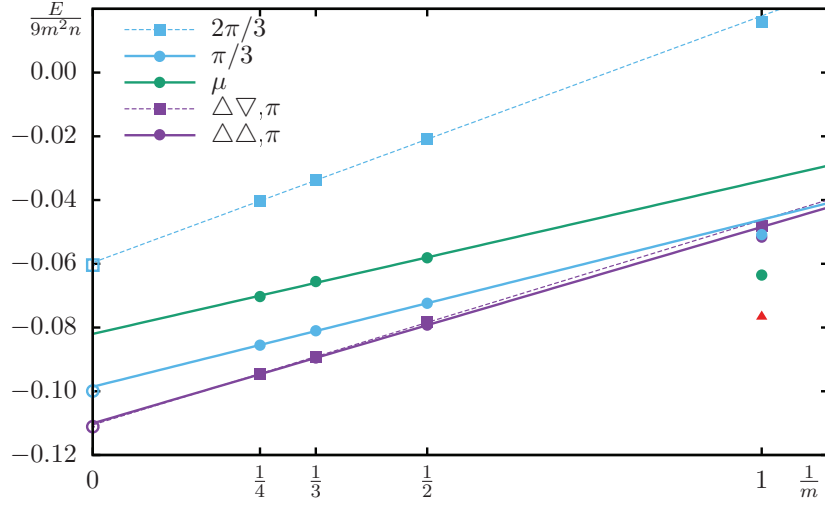


Figure 7.7 – $SU(3m)$ phase diagram for the triangular lattice, where the optimal variational energy of each wave function is given $m = 1, 2, 3, 4$. The blue symbols represent the chiral wave functions with $2\pi/3$ and $\pi/3$ for respectively the squares and circles. The three-sublattice-ordered state is represented in green. The purple shows the plaquette wave functions, squares and circles stand for $(\Delta\nabla, \pi)$ and $(\Delta\Delta, \pi)$ respectively. The red triangle is the energy of reference [28]. The lines are linear fits based on $m = 2, 3, 4$ to allow a mean-field extrapolation. The empty symbols represent the mean-field energy of the k -simplex VCS state (purple) and the chiral wave function (blue). These results were obtained for a system of 324 sites and antiperiodic boundary conditions and the error bars are smaller than the symbols.

potential wave functions provide an unreliable way to study ordered ground states. This variational study completes the phase diagram for $m > 1$: the ground state consists of weakly coupled triangular plaquettes. Four different plaquette states are in competition but the $(\Delta\Delta, \phi)$ seems to be favoured for small m . The larger m is, the stronger the competition between the four plaquette states is because in the mean-field limit they are all equivalent. It is interesting to note again that the extrapolation to $m \rightarrow \infty$ of the VMC results recovers the energy of the mean-field solution for all wave functions.

General conclusions

In the course of this thesis, an extensive use of the VMC algorithm based on fermionic Gutzwiller projected wave functions allowed us to shed some light on the ground of the $SU(N)$ Heisenberg model in fully antisymmetric irreps on various lattices. The study of this Hamiltonian is essential to the understanding of the low energy physics of ultra-cold gas of fermionic atoms trapped in optical lattices in different Mott insulating phases with m particles per optical well corresponding to different irreps of the $SU(N)$ Lie algebra.

The first results presented in this work concerned the 1-dimensional chain for which the nature of the ground state was predicted by non-abelian bosonisation for most of the irreps of $SU(N)$. Using very simple variational wave functions, it was possible to confirm the gapped nature for two types of systems. The first type corresponds to $k \equiv N/m = 2$ and $N > 2$ for which an Umklapp term appears in the field theory. The second type concerns only $SU(6)$ with $m = 2$ for which a relevant operator exists. Additionally, all other cases were proved to be gapless even when a marginal operator is present.

The next system of interest was the ladder for which the ground state was studied as a function of the inter-leg coupling. When $k = 2$, the results obtained agree with the simple description of the weak and strong coupling limit. For $k = 3$, the physics is extremely dependent on m in the weak coupling limit and different ground states have been found by VMC. The $SU(9)$ case with $m = 3$ seems to be the most interesting one because two different gapped ground states were found by the PSO algorithm. The $k = 4$ cases were also studied for $m = 1, 2$ and the transition between a gapless state and a 4-site plaquette state appears for a finite value of the inter-leg coupling. This does not fully agree with recent numerical results for $SU(4)$ $m = 1$, which predicts the presence of the plaquette state as soon as the inter-leg coupling is switched on. More generally, the PSO algorithm found various relevant variational wave functions for each case and it is possible to study more precisely the transitions between the different ground states.

The square lattice was the first 2-dimensional lattice to be presented. The aim was to go beyond mean-field predictions and to study the nature of the ground state for different k as a function of m . As the mean-field solution predicts that the ground state breaks the lattice symmetry for $k < 5$ and breaks the time reversal symmetry for $k \geq 5$, we focused our effort on the $SU(3m)$ and $SU(6m)$ phase diagram. We were able to confirm the presence of the lattice

symmetry breaking state for $k = 3$ as soon as $m > 2$. The colour ordered ground state was already known for $m = 1$ and a very interesting situation appears for $m = 2$. Indeed, at the VMC level, the ground state seems to be chiral even if this state is in competition with a columnar trimer state. This leaves the door open to an experimentally realisable chiral state for the $SU(6)$ $m = 2$ Heisenberg model on the square lattice. The other situations, where a chiral phase was observed during this study, was for $k = 6$ and $m > 1$ which agrees with mean-field theory but is not experimentally realisable. Moreover, it was also attempted to recover colour ordered states present for $SU(3)$, $SU(4)$ and $SU(5)$ with $m = 1$. Despite using different types of variational wave functions built to create a given colour order, no variational optimal solution was found to agree with other predictions. This was not surprising because the wave functions used in this study have the tendency to “freeze” the particles. A better approach to study ordered states would be to use a generalisation to $SU(N)$ of Jastrow based variational wave functions.

The next chapter of this thesis concerned the honeycomb lattice. We attempted to make the connection between a plaquette state recently predicted for the $SU(6)$ $m = 1$ case, and the chiral ground state appearing in the mean-field limit. Using five different variational wave functions, the phase diagram of the $SU(6m)$ Heisenberg model was studied and it was possible to show that the chiral phase is stabilised for $m > 1$.

We have finally studied the phase diagram of the $SU(3m)$ Heisenberg model on the triangular lattice. It was already known that the ground state consists of an ordered state with diagonal stripe when $m = 1$. This state was reproduced in the VMC framework thanks to an on-site chemical potential. As soon as $m > 1$, a triangular plaquette state corresponding to the mean-field k -simplex VCS state is favoured.

Overall, this variational method is efficiently giving some insight on the nature of the ground states of $SU(N)$ Heisenberg models in various fully antisymmetric irreps. It can explore the phase diagram quite efficiently and gives interesting preliminary results. One should keep in mind however that, as all variational methods, it only provides an upper bound to the energy and needs complementary approaches to be exploited at its best. As there are currently few numerical results for non trivial irreps, the use of the PSO algorithm was crucial to measure as many variational wave functions as possible and to get meaningful results. This thesis contributes to the quest to find new exotic properties and ground states in cold atoms experiments.

Back Matter

A Coherent states

This section is largely inspired by Auerbach [81] and uses the same notation. By definition, a coherent state $|z\rangle$ is an eigenstate of the destruction \hat{c} operator with eigenvalue z :

$$\hat{c} |z\rangle = z |z\rangle \quad (\text{A.1})$$

For the fermionic case z and z^* are considered to be independent Grassmann variables, while for the bosonic case, they are complex conjugate numbers. Let us present briefly some properties for two Grassmann variables z_1, z_2 :

$$z_1 c = c z_1, \quad c \in \mathbb{R}, \mathbb{C} \quad (\text{A.2})$$

$$z_1 z_2 = -z_2 z_1 \quad (\text{A.3})$$

$$z_1 z_2^* = -z_2^* z_1 \quad (\text{A.4})$$

$$(z_1 z_2)^* = z_2^* z_1^* \Rightarrow z_1 z_1^* \in \mathbb{R} \quad (\text{A.5})$$

Following [81], in the fermionic case, due to the anti-commuting nature of the Grassmann variables, the integration behaves like a counting operation:

$$\int dz_1 \prod_{i=1,2,\dots} z_i^{n_i} \prod_{j=1,2,\dots} (z_j^*)^{m_j} = n_1 \prod_{j=2,3,\dots} z_j^{n_j} \prod_{j=1,2,\dots} (z_j^*)^{m_j} \quad (\text{A.6})$$

where $m_i, n_j = 0, 1$. Because Grassmann variables anticommute, the order is important for the definition of the integration over $d^2 z$:

$$\int d^2 z O(z^*, z) \equiv \int dz^* \left(\int dz O(z^*, z) \right) \quad (\text{A.7})$$

Combining those two definitions, the Grassmann Gaussian integral is given by:

$$\int d^2 z e^{-z^* z} z^m (z^*)^n = \delta_{mn} \quad (\text{A.8})$$

Appendix A. Coherent states

For the Bosonic case, the integration over $d^2 z$ is defined for a complex number $z = x + iy$ as:

$$\int d^2 z \equiv \frac{1}{\pi} \int dx dy \quad (\text{A.9})$$

This allows to compute complex Gaussian integral:

$$\frac{1}{n!} \int d^2 z e^{-z^* z} z^m (z^*)^n = \delta_{mn} \quad (\text{A.10})$$

We can build a non orthogonal basis $\{|z\rangle\}$ of coherent states that spans the Fock space:

$$|z\rangle = e^{\mathbf{z}\hat{\mathbf{c}}^\dagger} |0\rangle \quad (\text{A.11})$$

where $\hat{\mathbf{c}}^\dagger = (\hat{c}_1^\dagger, \dots, \hat{c}_L^\dagger)$ is a vector of fermionic (bosonic) construction operators and $\mathbf{z} = (z_1, \dots, z_L)$ is a vector of Grassmann variables (complex numbers). The scalar product and closure relation related to these coherent states are given by:

$$\langle \mathbf{z} | \mathbf{z}' \rangle = e^{\mathbf{z}^* \mathbf{z}'} \quad (\text{A.12})$$

$$\mathbb{1} = \int d^2 \mathbf{z} e^{-\mathbf{z}^* \mathbf{z}} |\mathbf{z}\rangle \langle \mathbf{z}| \quad (\text{A.13})$$

where $d^2 \mathbf{z}$ is the integration measure given by $d^2 \mathbf{z} \equiv d\mathbf{z}^* d\mathbf{z}$. These relations hold for both the fermionic and bosonic cases. Thanks to this basis, we can easily compute the trace of any operator \hat{O} if we provide a complete basis $\{|\phi_i\rangle\}$:

$$\text{Tr}(\hat{O}) = \sum_i \langle \phi_i | \hat{O} | \phi_i \rangle \quad (\text{A.14})$$

$$= \sum_n \int d^2 \mathbf{z} e^{-\mathbf{z}^* \mathbf{z}} \langle \phi_i | \mathbf{z} \rangle \langle \mathbf{z} | \hat{O} | \phi_i \rangle \quad (\text{A.15})$$

$$= \sum_n \int d^2 \mathbf{z} e^{-\mathbf{z}^* \mathbf{z}} \langle \eta \mathbf{z} | \hat{O} | \phi_i \rangle \langle \phi_i | \mathbf{z} \rangle \quad (\text{A.16})$$

$$= \int d^2 \mathbf{z} e^{-\mathbf{z}^* \mathbf{z}} \langle \eta \mathbf{z} | \hat{O} | \mathbf{z} \rangle \quad (\text{A.17})$$

The factor $\eta = -1$ ($\eta = 1$) comes from the permutation of Grassmann variables (complex numbers) because we are dealing with fermions (bosons). We can also express the matrix elements of a normal ordered operator \hat{O} between coherent states:

$$\langle \mathbf{z} | \hat{O} | \mathbf{z}' \rangle = \sum_{\{n_i, n'_i\}} O_{\{n_i, n'_i\}} \langle \mathbf{z} | \hat{c}_1^{\dagger n_1} \dots \hat{c}_L^{\dagger n_L} \hat{c}_1^{n'_1} \dots \hat{c}_L^{n'_L} | \mathbf{z}' \rangle \quad (\text{A.18})$$

$$= \sum_{\{n_i, n'_i\}} O_{\{n_i, n'_i\}} \mathbf{z}_1^{* n_1} \dots \mathbf{z}_L^{* n_L} \mathbf{z}'_1^{n'_1} \dots \mathbf{z}'_L^{n'_L} e^{\mathbf{z}^* \mathbf{z}'} = O(\mathbf{z}^*, \mathbf{z}') e^{\mathbf{z}^* \mathbf{z}'} \quad (\text{A.19})$$

with $n_i, n'_i = 0, 1$ for fermions and $n_i \in \mathbb{N}$ for bosons.

B Complements about the VMC

B.1 Variational wave function expressed with determinants

The easiest way to be convinced that writing the Gutzwiller state as a sum of configurations weighted by determinants as shown in (2.19), is to make an example. Let us therefore take a non-trivial situation with $N = 3$, $m = 2$ and $n = 6$. The full wave function is given by:

$$\begin{aligned}
 |\Psi\rangle &= \prod_{\alpha=1}^3 \prod_{i=1}^4 \sum_{j=1}^6 U_{ji}^{\alpha} \hat{c}_{j\alpha}^{\dagger} |0\rangle \\
 &= \left(U_{11}^A \hat{c}_{1A}^{\dagger} + U_{21}^A \hat{c}_{2A}^{\dagger} + U_{31}^A \hat{c}_{3A}^{\dagger} + U_{41}^A \hat{c}_{4A}^{\dagger} + U_{51}^A \hat{c}_{5A}^{\dagger} + U_{61}^A \hat{c}_{6A}^{\dagger} \right) \times \\
 &\quad \times \left(U_{12}^A \hat{c}_{1A}^{\dagger} + U_{22}^A \hat{c}_{2A}^{\dagger} + U_{32}^A \hat{c}_{3A}^{\dagger} + U_{42}^A \hat{c}_{4A}^{\dagger} + U_{52}^A \hat{c}_{5A}^{\dagger} + U_{62}^A \hat{c}_{6A}^{\dagger} \right) \times \\
 &\quad \times \left(U_{13}^A \hat{c}_{1A}^{\dagger} + U_{23}^A \hat{c}_{2A}^{\dagger} + U_{33}^A \hat{c}_{3A}^{\dagger} + U_{43}^A \hat{c}_{4A}^{\dagger} + U_{53}^A \hat{c}_{5A}^{\dagger} + U_{63}^A \hat{c}_{6A}^{\dagger} \right) \times \\
 &\quad \times \left(U_{14}^A \hat{c}_{1A}^{\dagger} + U_{24}^A \hat{c}_{2A}^{\dagger} + U_{34}^A \hat{c}_{3A}^{\dagger} + U_{44}^A \hat{c}_{4A}^{\dagger} + U_{54}^A \hat{c}_{5A}^{\dagger} + U_{64}^A \hat{c}_{6A}^{\dagger} \right) \times \\
 &\quad \times \left(U_{11}^B \hat{c}_{1B}^{\dagger} + U_{21}^B \hat{c}_{2B}^{\dagger} + U_{31}^B \hat{c}_{3B}^{\dagger} + U_{41}^B \hat{c}_{4B}^{\dagger} + U_{51}^B \hat{c}_{5B}^{\dagger} + U_{61}^B \hat{c}_{6B}^{\dagger} \right) \times \\
 &\quad \times \left(U_{12}^B \hat{c}_{1B}^{\dagger} + U_{22}^B \hat{c}_{2B}^{\dagger} + U_{32}^B \hat{c}_{3B}^{\dagger} + U_{42}^B \hat{c}_{4B}^{\dagger} + U_{52}^B \hat{c}_{5B}^{\dagger} + U_{62}^B \hat{c}_{6B}^{\dagger} \right) \times \\
 &\quad \times \left(U_{13}^B \hat{c}_{1B}^{\dagger} + U_{23}^B \hat{c}_{2B}^{\dagger} + U_{33}^B \hat{c}_{3B}^{\dagger} + U_{43}^B \hat{c}_{4B}^{\dagger} + U_{53}^B \hat{c}_{5B}^{\dagger} + U_{63}^B \hat{c}_{6B}^{\dagger} \right) \times \\
 &\quad \times \left(U_{14}^B \hat{c}_{1B}^{\dagger} + U_{24}^B \hat{c}_{2B}^{\dagger} + U_{34}^B \hat{c}_{3B}^{\dagger} + U_{44}^B \hat{c}_{4B}^{\dagger} + U_{54}^B \hat{c}_{5B}^{\dagger} + U_{64}^B \hat{c}_{6B}^{\dagger} \right) \times \\
 &\quad \times \left(U_{11}^C \hat{c}_{1C}^{\dagger} + U_{21}^C \hat{c}_{2C}^{\dagger} + U_{31}^C \hat{c}_{3C}^{\dagger} + U_{41}^C \hat{c}_{4C}^{\dagger} + U_{51}^C \hat{c}_{5C}^{\dagger} + U_{61}^C \hat{c}_{6C}^{\dagger} \right) \times \\
 &\quad \times \left(U_{12}^C \hat{c}_{1C}^{\dagger} + U_{22}^C \hat{c}_{2C}^{\dagger} + U_{32}^C \hat{c}_{3C}^{\dagger} + U_{42}^C \hat{c}_{4C}^{\dagger} + U_{52}^C \hat{c}_{5C}^{\dagger} + U_{62}^C \hat{c}_{6C}^{\dagger} \right) \times \\
 &\quad \times \left(U_{13}^C \hat{c}_{1C}^{\dagger} + U_{23}^C \hat{c}_{2C}^{\dagger} + U_{33}^C \hat{c}_{3C}^{\dagger} + U_{43}^C \hat{c}_{4C}^{\dagger} + U_{53}^C \hat{c}_{5C}^{\dagger} + U_{63}^C \hat{c}_{6C}^{\dagger} \right) \times \\
 &\quad \times \left(U_{14}^C \hat{c}_{1C}^{\dagger} + U_{24}^C \hat{c}_{2C}^{\dagger} + U_{34}^C \hat{c}_{3C}^{\dagger} + U_{44}^C \hat{c}_{4C}^{\dagger} + U_{54}^C \hat{c}_{5C}^{\dagger} + U_{64}^C \hat{c}_{6C}^{\dagger} \right) |0\rangle
 \end{aligned} \tag{B.2}$$

Appendix B. Complements about the VMC

The projector will only keep the configurations with $m = 2$ particles per site. A particular one is for instance:

$$|\mathcal{C}_0\rangle = \hat{c}_{2A}^\dagger \hat{c}_{5A}^\dagger \hat{c}_{1A}^\dagger \hat{c}_{4A}^\dagger \hat{c}_{1B}^\dagger \hat{c}_{6B}^\dagger \hat{c}_{2B}^\dagger \hat{c}_{3B}^\dagger \hat{c}_{4C}^\dagger \hat{c}_{3C}^\dagger \hat{c}_{5C}^\dagger \hat{c}_{6C}^\dagger |0\rangle \quad (\text{B.3})$$

It is straightforward to check that the weight of this state is $\langle \mathcal{C}_0 | \Psi_G \rangle = \det(\mathcal{C}_0)$ such that:

$$\det(\mathcal{C}_0) \equiv \begin{vmatrix} U_{21}^A & U_{22}^A & U_{23}^A & U_{24}^A \\ U_{51}^A & U_{52}^A & U_{53}^A & U_{54}^A \\ U_{11}^A & U_{12}^A & U_{13}^A & U_{14}^A \\ U_{41}^A & U_{42}^A & U_{43}^A & U_{44}^A \end{vmatrix} \begin{vmatrix} U_{11}^B & U_{12}^B & U_{13}^B & U_{14}^B \\ U_{61}^B & U_{62}^B & U_{63}^B & U_{64}^B \\ U_{21}^B & U_{22}^B & U_{23}^B & U_{24}^B \\ U_{31}^B & U_{32}^B & U_{33}^B & U_{34}^B \end{vmatrix} \begin{vmatrix} U_{41}^C & U_{42}^C & U_{43}^C & U_{44}^C \\ U_{31}^C & U_{32}^C & U_{33}^C & U_{34}^C \\ U_{51}^C & U_{52}^C & U_{53}^C & U_{54}^C \\ U_{61}^C & U_{62}^C & U_{63}^C & U_{64}^C \end{vmatrix} \quad (\text{B.4})$$

which is the product of three determinants $\det(\mathcal{C}_0) = \det(\mathcal{C}_A) \det(\mathcal{C}_B) \det(\mathcal{C}_C)$. The matrices used in the determinant have a particular form. Each matrix involves only one colour α and the first mn/N eigenvectors related to the lowest eigenvalues of \hat{T}_α . Its r -th row is related to the r -th creation operator of colour α indexed by $\hat{c}_{i\alpha}^\dagger$ which results in using the i -th entries of each selected eigenvector. As the states $|\mathcal{C}\rangle$ generate all possible colour configurations, the state $|\Psi_G\rangle$ can naturally be expressed as:

$$|\Psi_G\rangle = \bigotimes_{\alpha=1}^N \sum_{\mathcal{C}_\alpha} \det(\mathcal{C}_\alpha) |\mathcal{C}_\alpha\rangle = \sum_{\mathcal{C}} \det(\mathcal{C}) |\mathcal{C}\rangle \quad (\text{B.5})$$

Now imagine that one applies $\hat{S}_1^{CB} \hat{S}_4^{BC}$ on the state $|\mathcal{C}_0\rangle$, the result is:

$$\hat{S}_1^{CB} \hat{S}_4^{BC} |\mathcal{C}_0\rangle = \hat{c}_{1C}^\dagger \hat{c}_{1B}^\dagger \hat{c}_{4B}^\dagger \hat{c}_{4C}^\dagger \hat{c}_{2A}^\dagger \hat{c}_{5A}^\dagger \hat{c}_{1A}^\dagger \hat{c}_{4A}^\dagger \hat{c}_{1B}^\dagger \hat{c}_{6B}^\dagger \hat{c}_{2B}^\dagger \hat{c}_{3B}^\dagger \hat{c}_{4C}^\dagger \hat{c}_{3C}^\dagger \hat{c}_{5C}^\dagger \hat{c}_{6C}^\dagger |0\rangle \quad (\text{B.6})$$

$$= \hat{c}_{2A}^\dagger \hat{c}_{5A}^\dagger \hat{c}_{1A}^\dagger \hat{c}_{4A}^\dagger \hat{c}_{1C}^\dagger \hat{c}_{6B}^\dagger \hat{c}_{2B}^\dagger \hat{c}_{3B}^\dagger \hat{c}_{4B}^\dagger \hat{c}_{3C}^\dagger \hat{c}_{5C}^\dagger \hat{c}_{6C}^\dagger |0\rangle \quad (\text{B.7})$$

$$= -\hat{c}_{2A}^\dagger \hat{c}_{5A}^\dagger \hat{c}_{1A}^\dagger \hat{c}_{4A}^\dagger \hat{c}_{4B}^\dagger \hat{c}_{6B}^\dagger \hat{c}_{2B}^\dagger \hat{c}_{3B}^\dagger \hat{c}_{1C}^\dagger \hat{c}_{3C}^\dagger \hat{c}_{5C}^\dagger \hat{c}_{6C}^\dagger |0\rangle \quad (\text{B.8})$$

$$= -|\mathcal{C}_1\rangle \quad (\text{B.9})$$

Thanks to the last permutation of \hat{c}_{4B}^\dagger and \hat{c}_{1C}^\dagger , the configuration $|\mathcal{C}_1\rangle$ is consistently defined with creation operator sorted by colours. This choice of convention is motivated by the fact that the determinants related to $|\mathcal{C}_1\rangle$ are identical to the ones of $|\mathcal{C}_0\rangle$ up to a change of only two rows. More precisely, $\hat{S}_1^{CB} \hat{S}_4^{BC}$ only modifies the first rows of the second and third matrices:

$$\det(\mathcal{C}_1) = \begin{vmatrix} U_{21}^A & U_{22}^A & U_{23}^A & U_{24}^A \\ U_{51}^A & U_{52}^A & U_{53}^A & U_{54}^A \\ U_{11}^A & U_{12}^A & U_{13}^A & U_{14}^A \\ U_{41}^A & U_{42}^A & U_{43}^A & U_{44}^A \end{vmatrix} \begin{vmatrix} U_{41}^B & U_{42}^B & U_{43}^B & U_{44}^B \\ U_{61}^B & U_{62}^B & U_{63}^B & U_{64}^B \\ U_{21}^B & U_{22}^B & U_{23}^B & U_{24}^B \\ U_{31}^B & U_{32}^B & U_{33}^B & U_{34}^B \end{vmatrix} \begin{vmatrix} U_{11}^C & U_{12}^C & U_{13}^C & U_{14}^C \\ U_{31}^C & U_{32}^C & U_{33}^C & U_{34}^C \\ U_{51}^C & U_{52}^C & U_{53}^C & U_{54}^C \\ U_{61}^C & U_{62}^C & U_{63}^C & U_{64}^C \end{vmatrix} \quad (\text{B.10})$$

B.2 Useful matrix formula

In the VMC algorithm ALG. 2 the computation of determinants appears many times, for instance the number of time that it is computed in ALG. 2₅ scales with the system size n . Likewise, the size of matrices scales like n and therefore the number of operations required to compute a determinant is of the order n^3 . This means that the number of operations required at each of the Monte-Carlo step scales like n^4 . From this simple observation, it is clear that the computation of determinant is the time consuming part of the algorithm. Some effort should be spent to improve its efficiency.

Suppose one has a $n \times n$ matrix A and knows its inverse A^{-1} . The following discussion gives a clever way to compute the determinant and inverse of a new matrix \tilde{A} when it is expressed as:

$$\tilde{A} = A + UV \quad (\text{B.11})$$

where V and U are respectively $m \times n$ and $n \times m$ matrices.

B.2.1 General Formula

B.2.1.1 Determinant lemma

The general formula to compute the determinant of a $n \times n$ matrix \tilde{A} is given by:

$$\det(\tilde{A}) = \det(A + UV) = \det(\mathbb{1} + VA^{-1}U) \det(A) = \det(W) \det(A) \quad (\text{B.12})$$

for $W \equiv \mathbb{1} + VA^{-1}U$.

B.2.1.2 Woodbury matrix identity

The Woodbury matrix identity states that the inverse of \tilde{A} can be expressed as:

$$\tilde{A}^{-1} = (A + UV)^{-1} = A^{-1} - A^{-1}UW^{-1}VA^{-1} \quad (\text{B.13})$$

where W is already known by the determinant lemma,

B.2.2 Formula in practice

The particular situation in which we would like to apply the determinant lemma formula is when a new matrix \tilde{A} is such that only the k -th row differs from the original matrix. If the k -th row of A is modified, the matrices U and V are simple vectors noted u and v and are given by:

$$v^T = u^T (\tilde{A} - A) \quad u = \hat{e}_k \quad (\text{B.14})$$

Appendix B. Complements about the VMC

Notice that $(uu^T)_{ij} = \delta_{ik}\delta_{jk}$, $u^T u = 1$ and:

$$uv^T = uu^T(\tilde{A} - A) = (\tilde{A} - A) \quad (\text{B.15})$$

W is now a scalar and the determinant lemma reduces to:

$$\det(A + uv^T) = (1 + v^T A^{-1} u) \det(A) = W \det(A) \quad (\text{B.16})$$

One can easily compute W :

$$W = 1 + v^T A^{-1} u \quad (\text{B.17})$$

$$= 1 + u^T (\tilde{A} - A) A^{-1} u \quad (\text{B.18})$$

$$= (u^T \tilde{A})(A^{-1} u) \quad (\text{B.19})$$

The last operation is simply the multiplication of the k -th row of \tilde{A} with the k -th column of A^{-1} . This can be efficiently done with the BLAS library.

If only one row of the \tilde{A} is different from A , then the Woodbury formula simplifies and is called the Sherman-Morrisson formula:

$$(A + uv^T)^{-1} = A^{-1} - \frac{A^{-1} uv^T A^{-1}}{1 + v^T A^{-1} u} \quad (\text{B.20})$$

The denominator is already known from the determinant lemma and is W . The numerator of this formula is:

$$A^{-1} uv^T A^{-1} = A^{-1} uu^T (\tilde{A} - A) A^{-1} \quad (\text{B.21})$$

$$= A^{-1} (uu^T \tilde{A} A^{-1} - uu^T) \quad (\text{B.22})$$

$$= A^{-1} B \quad (\text{B.23})$$

It is computationally more efficient to first compute B , the term in parenthesis, because this can be done in n^2 operations. Indeed, one can notice that $uu^T \tilde{A}$ returns a matrix where the k -th line is the k -th line of \tilde{A} and all other entries are 0. The term in parenthesis finally takes the form:

$$B_{ij} = \delta_{ik} (\tilde{A}_{il} A_{lj}^{-1} - \delta_{jk}) \quad (\text{B.24})$$

The computation of this matrix can be done with a BLAS routine because it can be put in a

matrix-vector product form:

$$uu^T \tilde{A} A^{-1} = \left((A^{-1})^T \tilde{A}^T uu^T \right)^T \quad (\text{B.25})$$

$$= \left((A^{-1})^T \begin{pmatrix} 0 & \cdots & 0 & \tilde{a}_{k1} & 0 & \cdots & 0 \\ \vdots & & \vdots & \vdots & \vdots & & \vdots \\ 0 & \cdots & 0 & \tilde{a}_{kn} & 0 & \cdots & 0 \end{pmatrix} \right)^T \quad (\text{B.26})$$

The BLAS routine will take the transpose of A^{-1} and multiply it by the k -th row of \tilde{A} .

The next operation consists of the multiplication of $A^{-1}B$. But this time, it is not possible to use BLAS because it is not possible to transform this product into a convenient form even if it requires n^2 operations:

$$A^{-1}B = A^{-1} \begin{pmatrix} 0 & \cdots & 0 \\ \vdots & & \vdots \\ 0 & \cdots & 0 \\ b_{k1} & \cdots & b_{kn} \\ 0 & \cdots & 0 \\ \vdots & & \vdots \\ 0 & \cdots & 0 \end{pmatrix} \quad (\text{B.27})$$

The use of BLAS routine was not as efficient as expected even if this numerical library is optimised to do perform common linear algebra operations. This is certainly due to the fact that the sizes of the matrices is not so large. Indeed, if one was to study a system with 10^6 sites, the matrices would be of that order and BLAS would be more efficient than a naive loops. But for systems with 100 sites, the overhead required to call the library is not compensated by its gain. Therefore in most cases, it is not required to use BLAS.

B.3 Issue with initialisation

In the initialisation phase, even before the thermalisation phase, an initial colour configuration has to be selected. As we saw, the weight in the variational wave function of this colour configuration is related to the determinant of given matrices that are named A in this appendix. If this determinant is very small, it physically means that this colour configuration is not relevant to the wave function. This also implies that the numerical inversion of A is subject to large errors. As the value of A^{-1} is essential to the correct execution of the algorithm, it should not be computed with potential numerical errors. Therefore, in the initialisation phase, the algorithm searches for a colour configuration with a significant weight. If such a state is found, then the matrix A^{-1} can safely be computed and the algorithm can use the matrix formula introduced in this appendix.

Appendix B. Complements about the VMC

Unfortunately, there are cases where the number of relevant colour configuration is so small that the algorithm cannot initialise. This typically happens when a strong on-site chemical potential is used to define the variational wave function because only the colour configuration respecting the chemical potential pattern will have a relevant weight. Another situation where this problem arises is when the variational wave function consists of decoupled plaquette because two identical colours cannot be present in the same plaquette.

We could solve this problem by manually giving a relevant initial colour configuration but as this problem does not arise often, it should not affect a VMC study.

C VMC and fully symmetric irreps

We will discuss here the possibility to study the $SU(N)$ Heisenberg model for fully symmetric irreps. In the framework of the VMC with the type of variational wave functions presented earlier, it is impossible to directly work in these irreps. It is therefore required to create a system which reproduces the interaction of fully symmetric states. One way to achieve this using fermionic operators, is to simulate a Hamiltonian for which the low energy sector is described by the fully symmetric irrep. The idea is to build a lattice of decoupled clusters and to force the ground state to be in the fully symmetric representation on each cluster. Then, by weakly connecting the clusters together, the low energy physics should be identical to the one given by $SU(N)$ Heisenberg model in the fully symmetric irrep because on each cluster the ground state is expected to remain in this irrep.

In the following, we will show how to construct the effective model and then apply it to a toy model exactly solvable. We will finally compare the exact results to VMC simulations and show that this numerical method does not work for this type of irrep.

C.1 Effective model

Consider a system with n sites where each site is in the fundamental irrep $m = 1$. The goal is to mimic a system of $\tilde{n} = n/\tilde{m}$ clusters in the fully (anti)symmetric representation labelled by a Young tableau with \tilde{m} boxes one row (column). To achieve that, let us first split the bonds into two families \mathcal{A} and \mathcal{B} . The family \mathcal{A} consists of bonds connecting \tilde{m} sites together with a coupling constant J . The bonds of the \mathcal{B} family connect those clusters together with a coupling constant J' . We then define the following Hamiltonians:

$$\hat{H} = \hat{H}_0 + \hat{H}_1 \tag{C.1}$$

$$\hat{H}_0 = J \sum_{\langle i,j \rangle \in \mathcal{A}} \hat{P}_{ij} \tag{C.2}$$

$$\hat{H}_1 = J' \sum_{\langle i,j \rangle \in \mathcal{B}} \hat{P}_{ij} \tag{C.3}$$

With this definition, \hat{H}_0 is such that if $J > 0$, then there is a unique singlet ground state composed of \tilde{m} sites and if $J < 0$, then the ground state is fully symmetric and degenerate. To be more explicit, in the SU(2) case when $J > 0$ ($J < 0$), each clusters consist of $\tilde{m} = 2$ and is in a singlet (triplet) state with energy: $E_0 = -|J|\tilde{n}$. The clusters are then connected together with links belonging to the set \mathcal{B} when $J' \neq 0$. When $J < 0$ ($J > 0$) and $|J'/J| \ll 1$, \hat{H}_1 can be seen as a perturbation and the representation is (anti)symmetric. In the following, we will focus on the case, where $J < 0$ and $0 < J' \ll |J|$ which is expected to capture the physic of fully symmetric states interacting with antiferromagnetic bonds.

C.2 Toy model

This part is dedicated to show why the VMC method is ill-suited to simulate models with a symmetric irrep of SU(N) on each site.

As we already discussed, the solution to do simulations in the antisymmetric irreps is to modify the Heisenberg Hamiltonian by introducing different couplings between different sites. Let us consider the simplest case of a 4-site SU(2) Heisenberg chain with periodic boundary condition:

$$\hat{H}_0 = J(\hat{P}_{12} + \hat{P}_{34}) \quad (\text{C.4})$$

$$\hat{H}_1 = J'(\hat{P}_{23} + \hat{P}_{41}) \quad (\text{C.5})$$

By setting $J = -1$ and $J' = 0.1$, we are in the limit, where $|J'/J| \ll 1$. Therefore, \hat{H} behaves as a 2-site antiferromagnet SU(2) Heisenberg chain with two particles per site in the symmetric representation.

In the following two parts, we will first apply perturbation theory to that example and then show that the VMC method is unable to reproduce the theoretical results.

C.2.1 Applying perturbation theory

For our toy model, the ground state of \hat{H}_0 is degenerate and consists of the 9 possible combinations of triplets:

$$|\phi_1\rangle = |1\rangle_{12} |1\rangle_{34} = |\uparrow\uparrow\uparrow\uparrow\rangle \quad (\text{C.6})$$

$$|\phi_2\rangle = |1\rangle_{12} |0\rangle_{34} = \frac{1}{\sqrt{2}}(|\uparrow\uparrow\uparrow\downarrow\rangle + |\uparrow\uparrow\downarrow\uparrow\rangle) \quad (\text{C.7})$$

$$|\phi_3\rangle = |1\rangle_{12} |\bar{1}\rangle_{34} = |\uparrow\uparrow\downarrow\downarrow\rangle \quad (\text{C.8})$$

$$|\phi_4\rangle = |0\rangle_{12} |1\rangle_{34} = \frac{1}{\sqrt{2}}(|\uparrow\downarrow\uparrow\uparrow\rangle + |\downarrow\uparrow\uparrow\uparrow\rangle) \quad (\text{C.9})$$

$$|\phi_5\rangle = |0\rangle_{12} |0\rangle_{34} = \frac{1}{2}(|\uparrow\downarrow\uparrow\downarrow\rangle + |\uparrow\downarrow\downarrow\uparrow\rangle + |\downarrow\uparrow\uparrow\downarrow\rangle + |\downarrow\uparrow\downarrow\uparrow\rangle) \quad (\text{C.10})$$

$$|\phi_6\rangle = |0\rangle_{12} |\bar{1}\rangle_{34} = \frac{1}{\sqrt{2}} (|\uparrow\downarrow\downarrow\downarrow\rangle + |\downarrow\uparrow\downarrow\downarrow\rangle) \quad (\text{C.11})$$

$$|\phi_7\rangle = |\bar{1}\rangle_{12} |1\rangle_{34} = |\downarrow\downarrow\uparrow\uparrow\rangle \quad (\text{C.12})$$

$$|\phi_8\rangle = |\bar{1}\rangle_{12} |0\rangle_{34} = \frac{1}{\sqrt{2}} (|\downarrow\downarrow\uparrow\downarrow\rangle + |\downarrow\downarrow\downarrow\uparrow\rangle) \quad (\text{C.13})$$

$$|\phi_9\rangle = |\bar{1}\rangle_{12} |\bar{1}\rangle_{34} = |\downarrow\downarrow\downarrow\downarrow\rangle \quad (\text{C.14})$$

Therefore, the ground state energy of \hat{H}_0 is $E_0 = 2J = -2$. When J' is turned on, the degenerate perturbation theory needs to be applied. This requires the computation of the matrix $V_{ij} = \langle \phi_i | \hat{H}_1 | \phi_j \rangle$ whose expression is given by:

$$V = J' \begin{pmatrix} 2 & 0 & 0 & 0 & 0 & 0 & 0 & 0 & 0 \\ 0 & 1 & 0 & 1 & 0 & 0 & 0 & 0 & 0 \\ 0 & 0 & 0 & 0 & 1 & 0 & 0 & 0 & 0 \\ 0 & 1 & 0 & 1 & 0 & 0 & 0 & 0 & 0 \\ 0 & 0 & 1 & 0 & 1 & 0 & 1 & 0 & 0 \\ 0 & 0 & 0 & 0 & 0 & 1 & 0 & 1 & 0 \\ 0 & 0 & 0 & 0 & 1 & 0 & 0 & 0 & 0 \\ 0 & 0 & 0 & 0 & 0 & 1 & 0 & 1 & 0 \\ 0 & 0 & 0 & 0 & 0 & 0 & 0 & 0 & 2 \end{pmatrix} \quad (\text{C.15})$$

with lowest eigenvalue being equal to $-J' = -0.1$. The energy of \hat{H} in first order in J' of the degenerate perturbation theory is then equal to:

$$E = 2J - J' = -2.1 \quad (\text{C.16})$$

C.2.2 VMC fails

As for the perturbation theory, the starting point of the procedure consist of studying \hat{H}_0 only. More precisely, we want to find a wave function that, after projection, gives an energy equal to $2J$. In order to achieve this for a chain with four sites and periodic boundary conditions, it is possible to use a very simple variational wave function:

$$\hat{T}^\alpha = t \left(\hat{c}_{1\alpha}^\dagger \hat{c}_{2\alpha} + \hat{c}_{3\alpha}^\dagger \hat{c}_{4\alpha} \right) + t' \left(\hat{c}_{2\alpha}^\dagger \hat{c}_{3\alpha} + \hat{c}_{4\alpha}^\dagger \hat{c}_{1\alpha} \right) \quad (\text{C.17})$$

Nevertheless, to be able to find an energy of $2J$, one has to use different variational Hamiltonians for the spin up and down according to the sign of J . More precisely, if $\hat{T}^\uparrow = -\hat{T}^\downarrow$, then the variational energy is equal to $2J$, when $|t| < |t'|$ for $J < 0$. When $J > 0$, using $\hat{T}^\uparrow = \hat{T}^\downarrow$ gives the correct energy.

Now that we have found a variational wave function that recovers the correct energy when the two singlets or triplets are decoupled, we can switch J' on. The figure FIG. C.1 shows the variational energy as a function of the ratio t'/t for the $J = -1$ and $J' = 0.1$. We can see that the

Appendix C. VMC and fully symmetric irreps

minimum occurs for $|t| < |t'|$, but its value of $E = 2J + J' = -1.9$ is not in agreement with (C.16).

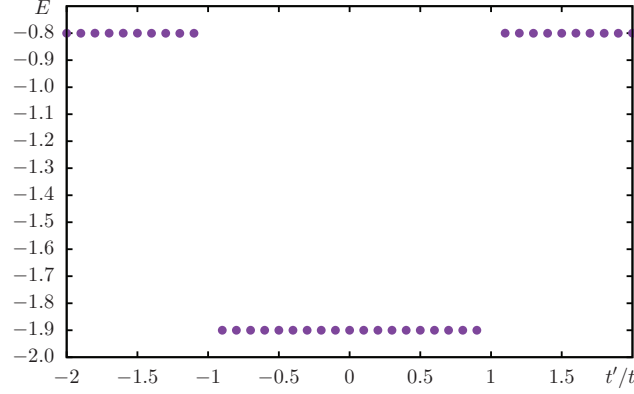


Figure C.1 – Variational energy for the SU(2) $m = 2$ case in the fully symmetric irrep on a system with four sites and periodic boundary conditions.

Let us understand this issue better. For the optimal value of the variational parameters, the eigenvectors of \hat{T}^\uparrow and \hat{T}^\downarrow are given by:

$$U^\uparrow = \frac{1}{2} \begin{pmatrix} -1 & -1 & -1 & 1 \\ 1 & 1 & -1 & 1 \\ -1 & 1 & 1 & 1 \\ 1 & -1 & 1 & 1 \end{pmatrix} \quad U^\downarrow = \frac{1}{2} \begin{pmatrix} -1 & -1 & -1 & 1 \\ -1 & -1 & 1 & -1 \\ 1 & -1 & -1 & -1 \\ 1 & -1 & 1 & 1 \end{pmatrix} \quad (\text{C.18})$$

Only the two first columns are relevant because they correspond to the two lowest eigenvalues. The normalised Gutzwiller projected variational state is given by:

$$|\Psi\rangle = \sum_{s=1}^4 \frac{(-1)^s}{2} |\psi_s\rangle \quad (\text{C.19})$$

with

$$|\psi_1\rangle = \hat{c}_{1\uparrow}^\dagger \hat{c}_{3\uparrow}^\dagger \hat{c}_{2\downarrow}^\dagger \hat{c}_{4\downarrow}^\dagger |0\rangle = |\uparrow\uparrow\downarrow\downarrow\rangle \quad |\psi_2\rangle = \hat{c}_{1\uparrow}^\dagger \hat{c}_{4\uparrow}^\dagger \hat{c}_{2\downarrow}^\dagger \hat{c}_{3\downarrow}^\dagger |0\rangle = |\uparrow\downarrow\downarrow\uparrow\rangle \quad (\text{C.20})$$

$$|\psi_3\rangle = \hat{c}_{2\uparrow}^\dagger \hat{c}_{4\uparrow}^\dagger \hat{c}_{1\downarrow}^\dagger \hat{c}_{3\downarrow}^\dagger |0\rangle = |\downarrow\downarrow\uparrow\uparrow\rangle \quad |\psi_4\rangle = \hat{c}_{2\uparrow}^\dagger \hat{c}_{3\uparrow}^\dagger \hat{c}_{1\downarrow}^\dagger \hat{c}_{4\downarrow}^\dagger |0\rangle = |\downarrow\uparrow\uparrow\downarrow\rangle \quad (\text{C.21})$$

To compute this state, one has computed the weight of all possible spin configurations given by $\det(U_{ij}^\uparrow) \det(U_{kl}^\downarrow)$ for a state $\hat{c}_{i\uparrow}^\dagger \hat{c}_{j\uparrow}^\dagger \hat{c}_{k\downarrow}^\dagger \hat{c}_{l\downarrow}^\dagger |0\rangle$ and matrices:

$$U_{mn}^\sigma = \begin{pmatrix} U_{m1}^\sigma & U_{m2}^\sigma \\ U_{n1}^\sigma & U_{n2}^\sigma \end{pmatrix} \quad (\text{C.22})$$

One can for instance check that the weight of $|\psi_1\rangle$ is given by:

$$\det \begin{pmatrix} U_{11}^\dagger & U_{12}^\dagger \\ U_{31}^\dagger & U_{32}^\dagger \end{pmatrix} \det \begin{pmatrix} U_{21}^\dagger & U_{22}^\dagger \\ U_{41}^\dagger & U_{42}^\dagger \end{pmatrix} = -1 \quad (\text{C.23})$$

The states:

$$|\psi_5\rangle = \hat{c}_{1\uparrow}^\dagger \hat{c}_{2\uparrow}^\dagger \hat{c}_{3\downarrow}^\dagger \hat{c}_{4\downarrow}^\dagger |0\rangle = |\uparrow\uparrow\downarrow\downarrow\rangle \quad |\psi_6\rangle = \hat{c}_{3\uparrow}^\dagger \hat{c}_{4\uparrow}^\dagger \hat{c}_{1\downarrow}^\dagger \hat{c}_{2\downarrow}^\dagger |0\rangle = |\downarrow\downarrow\uparrow\uparrow\rangle \quad (\text{C.24})$$

have a weight of zero because one of the determinants is zero. Now that we have explicitly computed the wave function, we can see how the permutation operator \hat{P}_{ij} acts on the states. When applied on the link 1 – 2 or 3 – 4, the result for each $|\psi_i\rangle$ is:

$$\hat{P}_{12}|\psi_1\rangle = -|\psi_4\rangle \quad \hat{P}_{34}|\psi_1\rangle = -|\psi_2\rangle \quad (\text{C.25})$$

$$\hat{P}_{12}|\psi_2\rangle = -|\psi_3\rangle \quad \hat{P}_{34}|\psi_2\rangle = -|\psi_1\rangle \quad (\text{C.26})$$

$$\hat{P}_{12}|\psi_3\rangle = -|\psi_2\rangle \quad \hat{P}_{34}|\psi_3\rangle = -|\psi_4\rangle \quad (\text{C.27})$$

$$\hat{P}_{12}|\psi_4\rangle = -|\psi_1\rangle \quad \hat{P}_{34}|\psi_4\rangle = -|\psi_3\rangle \quad (\text{C.28})$$

On a link 2 – 3 or 4 – 1:

$$\hat{P}_{23}|\psi_1\rangle = |\psi_5\rangle \rightarrow 0 \quad \hat{P}_{41}|\psi_1\rangle = |\psi_6\rangle \rightarrow 0 \quad (\text{C.29})$$

$$\hat{P}_{23}|\psi_2\rangle = |\psi_2\rangle \quad \hat{P}_{41}|\psi_2\rangle = |\psi_2\rangle \quad (\text{C.30})$$

$$\hat{P}_{23}|\psi_3\rangle = |\psi_6\rangle \rightarrow 0 \quad \hat{P}_{41}|\psi_3\rangle = |\psi_5\rangle \rightarrow 0 \quad (\text{C.31})$$

$$\hat{P}_{23}|\psi_4\rangle = |\psi_4\rangle \quad \hat{P}_{41}|\psi_4\rangle = |\psi_4\rangle \quad (\text{C.32})$$

the permutation operator transforms $|\psi_1\rangle$ and $|\psi_3\rangle$ into states which have zero weight in the variational wave function. As the total energy is given by $E = \langle \Psi | J(P_{12} + P_{34}) + J'(P_{23} + P_{41}) | \Psi \rangle$ one needs to compute $\langle \Psi | P_{ij} | \Psi \rangle$

For P_{12} and P_{34} we have:

$$P_{12}|\Psi\rangle = \frac{1}{2}P_{12}(-|\psi_1\rangle + |\psi_2\rangle - |\psi_3\rangle + |\psi_4\rangle) = \frac{1}{2}(+|\psi_4\rangle - |\psi_3\rangle + |\psi_2\rangle - |\psi_1\rangle) \quad (\text{C.33})$$

$$P_{34}|\Psi\rangle = \frac{1}{2}P_{32}(-|\psi_1\rangle + |\psi_2\rangle - |\psi_3\rangle + |\psi_4\rangle) = \frac{1}{2}(+|\psi_2\rangle - |\psi_1\rangle + |\psi_4\rangle - |\psi_3\rangle) \quad (\text{C.34})$$

and it can be concluded that $\langle \Psi | P_{12} | \Psi \rangle = \langle \Psi | P_{34} | \Psi \rangle = 1$ as it should for a triplet state. For P_{23} and P_{41} , one gets $\langle \Psi | P_{23} | \Psi \rangle = \langle \Psi | P_{41} | \Psi \rangle = \frac{1}{2}$. Therefore, we see that the VMC energy is given by: $E = 2J + J'$ which is in disagreement with the degenerate perturbation theory that predicts $E = 2J - J'$.

C.3 Additional comments

Thanks to the toy model introduced above, we showed that using VMC for irreps which are not fully antisymmetric is very problematic. Of course we have used a very simple variational wave function, but we do not expect to see the problem disappear for more complicated ones. We have also checked that the same problem arises for systems with more sites. Therefore, it seems difficult to implement spin-1 Heisenberg model by choosing different bond energies J .

Moreover, in order to recover the correct energy when $J' = 0$, it was required to use different variational Hamiltonian for the spin up and down, more precisely $\hat{T}^\uparrow = -\hat{T}^\downarrow$. Hence the generalisation to $SU(N)$ with $N > 2$ is definitely not straightforward.

This idea to use different J and J' bonds to reproduce a given irrep has been successfully used with QMC for fully antisymmetric irreps.

Bibliography

- [1] Richard P. Feynman. “Simulating physics with computers”. In: *International Journal of Theoretical Physics* 21.6-7 (June 1982), pp. 467–488. ISSN: 0020-7748. DOI: 10.1007/BF02650179.
- [2] Dieter Jaksch and P. Zoller. “The cold atom Hubbard toolbox”. In: *Annals of Physics* 315.1 (Jan. 2005), pp. 52–79. ISSN: 00034916. DOI: 10.1016/j.aop.2004.09.010.
- [3] M. Lewenstein et al. “Ultracold atomic gases in optical lattices: mimicking condensed matter physics and beyond”. In: *Advances in Physics* 56.2 (Mar. 2007), pp. 243–379. ISSN: 0001-8732. DOI: 10.1080/00018730701223200.
- [4] Miguel A. Cazalilla and Ana Maria Rey. “Ultracold Fermi gases with emergent $SU(N)$ symmetry”. In: *Reports on Progress in Physics* 77.12 (2014), p. 124401. ISSN: 0034-4885. DOI: 10.1088/0034-4885/77/12/124401.
- [5] Immanuel Bloch, Jean Dalibard, and Wilhelm Zwerger. “Many-body physics with ultracold gases”. In: *Reviews of Modern Physics* 80.3 (July 2008), pp. 885–964. ISSN: 0034-6861. DOI: 10.1103/RevModPhys.80.885.
- [6] Congjun Wu, Jiang-ping Hu, and Shou-cheng Zhang. “Exact $SO(5)$ symmetry in the spin-3/2 fermionic system.” In: *Physical Review Letters* 91.18 (Oct. 2003), p. 186402. ISSN: 0031-9007. DOI: 10.1103/PhysRevLett.91.186402.
- [7] Carsten Honerkamp and Walter Hofstetter. “Ultracold fermions and the $SU(N)$ hubbard model”. In: *Physical Review Letters* 92.17 (Apr. 2004), pp. 170403–1. ISSN: 00319007. DOI: 10.1103/PhysRevLett.92.170403.
- [8] Miguel A. Cazalilla, A. F. Ho, and M. Ueda. “Ultracold gases of ytterbium: ferromagnetism and Mott states in an $SU(6)$ Fermi system”. In: *New Journal of Physics* 11.10 (Oct. 2009), p. 103033. ISSN: 1367-2630. DOI: 10.1088/1367-2630/11/10/103033.
- [9] A. V. Gorshkov et al. “Two-orbital $SU(N)$ magnetism with ultracold alkaline-earth atoms”. In: *Nature Physics* 6.4 (Apr. 2010), pp. 289–295. ISSN: 1745-2473. DOI: 10.1038/nphys1535.
- [10] Roland Assaraf et al. “Metal-insulator transition in the one-dimensional $SU(N)$ Hubbard model”. In: *Physical Review B* 60.4 (July 1999), pp. 2299–2318. ISSN: 0163-1829. DOI: 10.1103/PhysRevB.60.2299.

Bibliography

- [11] Francesco Scazza et al. “Observation of two-orbital spin-exchange interactions with ultracold $SU(N)$ -symmetric fermions”. In: *Nature Physics* 10.10 (Aug. 2014), pp. 779–784. DOI: 10.1038/nphys3061.
- [12] X. Zhang et al. “Spectroscopic observation of $SU(N)$ -symmetric interactions in Sr orbital magnetism”. In: *Science* 345.6203 (Sept. 2014), pp. 1467–1473. ISSN: 0036-8075. DOI: 10.1126/science.1254978.
- [13] Guido Pagano et al. “A one-dimensional liquid of fermions with tunable spin”. In: *Nature Physics* 10.3 (Feb. 2014), pp. 198–201. ISSN: 1745-2473. DOI: 10.1038/nphys2878.
- [14] Christian Hofrichter et al. “Direct Probing of the Mott Crossover in the $SU(N)$ Fermi-Hubbard Model”. In: *Physical Review X* 6.2 (June 2016), p. 021030. ISSN: 2160-3308. DOI: 10.1103/PhysRevX.6.021030.
- [15] Bill Sutherland. “Model for a multicomponent quantum system”. In: *Physical Review B* 12.9 (Nov. 1975), pp. 3795–3805. ISSN: 0556-2805. DOI: 10.1103/PhysRevB.12.3795.
- [16] Beat Frischmuth, Frédéric Mila, and Matthias Troyer. “Thermodynamics of the One-Dimensional $SU(4)$ Symmetric Spin-Orbital Model”. In: *Physical Review Letters* 82.4 (Jan. 1999), pp. 835–838. ISSN: 0031-9007. DOI: 10.1103/PhysRevLett.82.835.
- [17] Laura Messio and Frédéric Mila. “Entropy dependence of correlations in one-dimensional $SU(N)$ antiferromagnets”. In: *Physical Review Letters* 109.20 (July 2012), p. 205306. ISSN: 00319007. DOI: 10.1103/PhysRevLett.109.205306.
- [18] Mathias van den Bossche et al. “Spontaneous plaquette formation in the $SU(4)$ spin-orbital ladder”. In: *Physical Review Letters* 86.18 (Apr. 2001), pp. 4124–4127. ISSN: 00319007. DOI: 10.1103/PhysRevLett.86.4124.
- [19] Philippe Lecheminant and A. M. Tsvelik. “Two-leg $SU(2n)$ spin ladder: A low-energy effective field theory approach”. In: *Physical Review B* 91.17 (May 2015), p. 174407. ISSN: 1098-0121. DOI: 10.1103/PhysRevB.91.174407.
- [20] Y. Q. Li et al. “ $SU(4)$ Theory for Spin Systems with Orbital Degeneracy”. In: *Physical Review Letters* 81.16 (Oct. 1998), pp. 3527–3530. ISSN: 0031-9007. DOI: 10.1103/PhysRevLett.81.3527.
- [21] Karlo Penc et al. “Quantum phase transition in the $SU(4)$ spin-orbital model on the triangular lattice”. In: *Physical Review B* 68.1 (July 2003), p. 012408. ISSN: 0163-1829. DOI: 10.1103/PhysRevB.68.012408.
- [22] Daniel P. Arovas. “Simplex solid states of $SU(N)$ quantum antiferromagnets”. In: *Physical Review B* 77.10 (Mar. 2008), p. 104404. ISSN: 1098-0121. DOI: 10.1103/PhysRevB.77.104404.
- [23] Fa Wang and Ashvin Vishwanath. “ Z_2 spin-orbital liquid state in the square lattice Kugel-Khomskii model”. In: *Physical Review B* 80.6 (Aug. 2009), p. 064413. ISSN: 1098-0121. DOI: 10.1103/PhysRevB.80.064413.

-
- [24] Hsiang-Hsuan Hung, Yupeng Wang, and Congjun Wu. “Quantum magnetism in ultra-cold alkali and alkaline-earth fermion systems with symplectic symmetry”. In: *Physical Review B* 84.5 (Aug. 2011), p. 054406. ISSN: 1098-0121. DOI: 10.1103/PhysRevB.84.054406.
 - [25] Philippe Corboz et al. “Competing states in the SU(3) Heisenberg model on the honeycomb lattice: Plaquette valence-bond crystal versus dimerized color-ordered state”. In: *Physical Review B* 87.19 (May 2013), p. 195113. ISSN: 1098-0121. DOI: 10.1103/PhysRevB.87.195113.
 - [26] Pierre Nataf et al. “Plaquette order in the SU(6) Heisenberg model on the honeycomb lattice”. In: *Physical Review B* 93.20 (May 2016), p. 201113. ISSN: 2469-9950. DOI: 10.1103/PhysRevB.93.201113.
 - [27] Philippe Corboz et al. “Spin-Orbital Quantum Liquid on the Honeycomb Lattice”. In: *Physical Review X* 2.4 (Nov. 2012), p. 041013. ISSN: 2160-3308. DOI: 10.1103/PhysRevX.2.041013.
 - [28] Bela Bauer et al. “Three-sublattice order in the SU(3) Heisenberg model on the square and triangular lattice”. In: *Physical Review B* 85.12 (Mar. 2012), p. 125116. ISSN: 1098-0121. DOI: 10.1103/PhysRevB.85.125116.
 - [29] Samuel Bieri et al. “Paired chiral spin liquid with a Fermi surface in S=1 model on the triangular lattice”. In: *Physical Review B* 86.22 (Dec. 2012), p. 224409. ISSN: 1098-0121. DOI: 10.1103/PhysRevB.86.224409.
 - [30] Tamás A. Tóth et al. “Three-sublattice ordering of the SU(3) Heisenberg model of three-flavor fermions on the square and cubic lattices”. In: *Physical Review Letters* 105.26 (Dec. 2010), p. 265301. ISSN: 00319007. DOI: 10.1103/PhysRevLett.105.265301.
 - [31] Philippe Corboz et al. “Simultaneous dimerization and SU(4) symmetry breaking of 4-color fermions on the square lattice”. In: *Physical Review Letters* 107.21 (Nov. 2011), p. 215301. ISSN: 00319007. DOI: 10.1103/PhysRevLett.107.215301.
 - [32] Pierre Nataf and Frédéric Mila. “Exact Diagonalization of Heisenberg SU(N) Models”. In: *Physical Review Letters* 113.12 (Sept. 2014), p. 127204. ISSN: 0031-9007. DOI: 10.1103/PhysRevLett.113.127204.
 - [33] Ian Affleck. “Exact critical exponents for quantum spin chains, non-linear σ -models at $\theta = \pi$ and the quantum hall effect”. In: *Nuclear Physics B* 265 (1986), pp. 409–447. ISSN: 05503213. DOI: 10.1016/0550-3213(86)90167-7.
 - [34] Ian Affleck. “Critical behaviour of SU(n) quantum chains and topological non-linear σ -models”. In: *Nuclear Physics B* 305.4 (Dec. 1988), pp. 582–596. ISSN: 05503213. DOI: 10.1016/0550-3213(88)90117-4.
 - [35] Fakher F. Assaad. “Phase diagram of the half-filled two-dimensional SU(N) Hubbard-Heisenberg model: A quantum Monte Carlo study”. In: *Physical Review B* 71.7 (Feb. 2005), p. 075103. ISSN: 1098-0121. DOI: 10.1103/PhysRevB.71.075103.

Bibliography

- [36] Zi Cai et al. “Quantum magnetic properties of the $SU(2N)$ Hubbard model in the square lattice: A quantum Monte Carlo study”. In: *Physical Review B* 88.12 (Sept. 2013), p. 125108. ISSN: 1098-0121. DOI: 10.1103/PhysRevB.88.125108.
- [37] Thomas C. Lang et al. “Dimerized Solids and Resonating Plaquette Order in $SU(N)$ -Dirac Fermions”. In: *Physical Review Letters* 111.6 (Aug. 2013), p. 066401. ISSN: 0031-9007. DOI: 10.1103/PhysRevLett.111.066401.
- [38] Zhichao Zhou et al. “Quantum Monte Carlo simulations of thermodynamic properties of $SU(2N)$ ultracold fermions in optical lattices”. In: *Physical Review B* 90.23 (Dec. 2014), p. 235139. ISSN: 1098-0121. DOI: 10.1103/PhysRevB.90.235139.
- [39] Da Wang et al. “Competing Orders in the 2D Half-Filled $SU(2N)$ Hubbard Model through the Pinning-Field Quantum Monte Carlo Simulations”. In: *Physical Review Letters* 112.15 (Apr. 2014), p. 156403. ISSN: 0031-9007. DOI: 10.1103/PhysRevLett.112.156403.
- [40] Arun Paramekanti and J. Brad Marston. “ $SU(N)$ quantum spin models: a variational wavefunction study”. In: *Journal of Physics: Condensed Matter* 19.12 (Mar. 2007), p. 125215. ISSN: 0953-8984. DOI: 10.1088/0953-8984/19/12/125215.
- [41] Ian Affleck and J. Brad Marston. “Large- n limit of the Heisenberg-Hubbard model: Implications for high- T_c superconductors”. In: *Physical Review B* 37.7 (1988), pp. 3774–3777. ISSN: 01631829. DOI: 10.1103/PhysRevB.37.3774.
- [42] Daniel S. Rokhsar. “Quadratic quantum antiferromagnets in the fermionic large- N limit”. In: *Physical Review B* 42.4 (Aug. 1990), pp. 2526–2531. ISSN: 0163-1829. DOI: 10.1103/PhysRevB.42.2526.
- [43] Michael Hermele, Victor Gurarie, and Ana Maria Rey. “Mott Insulators of Ultracold Fermionic Alkaline Earth Atoms: Underconstrained Magnetism and Chiral Spin Liquid”. In: *Physical Review Letters* 103.13 (Sept. 2009), p. 135301. ISSN: 0031-9007. DOI: 10.1103/PhysRevLett.103.135301.
- [44] Michael Hermele and Victor Gurarie. “Topological liquids and valence cluster states in two-dimensional $SU(N)$ magnets”. In: *Physical Review B* 84.17 (Nov. 2011), p. 174441. ISSN: 1098-0121. DOI: 10.1103/PhysRevB.84.174441.
- [45] Howard Georgi. *Lie Algebras in Particle Physics: From Isospin to Unified Theories*. Westview Press, 1999, p. 344. ISBN: 0738202339.
- [46] J. F. Cornwell. *Group theory in physics*. Vol. 2. Techniques of physics. Academic Press, 1985.
- [47] M Hamermesh. *Group Theory and Its Application to Physical Problems*. Addison Wesley Series in Physics. Dover Publications, 1962.
- [48] Alfred Young. “On Quantitative Substitutional Analysis”. In: *Proceedings of the London Mathematical Society* s2-34.1 (Jan. 1932), pp. 196–230. ISSN: 0024-6115. DOI: 10.1112/plms/s2-34.1.196.

-
- [49] Alfred Young. "On Quantitative Substitutional Analysis". In: *Proceedings of the London Mathematical Society* s2-36.1 (Jan. 1934), pp. 304–368. ISSN: 0024-6115. DOI: 10.1112/plms/s2-36.1.304.
- [50] Pierre Nataf and Frédéric Mila. "Exact diagonalization of Heisenberg $SU(N)$ chains in the fully symmetric and antisymmetric representations". In: *Physical Review B* 93.15 (Apr. 2016), p. 155134. ISSN: 2469-9950. DOI: 10.1103/PhysRevB.93.155134.
- [51] Miklós Lajkó and Karlo Penc. "Tetramerization in a $SU(4)$ Heisenberg model on the honeycomb lattice". In: *Physical Review B* 87.22 (June 2013), p. 224428. ISSN: 1098-0121. DOI: 10.1103/PhysRevB.87.224428.
- [52] Vinay Ambegaokar and Matthias Troyer. "Estimating errors reliably in Monte Carlo simulations of the Ehrenfest model". In: *American Journal of Physics* 78.2 (2010), p. 150. ISSN: 00029505. DOI: 10.1119/1.3247985.
- [53] James Kennedy and Russell C. Eberhart. "Particle swarm optimization". In: *Proceedings of ICNN'95 - International Conference on Neural Networks*. Vol. 4. IEEE, 1995, pp. 1942–1948. ISBN: 0-7803-2768-3. DOI: 10.1109/ICNN.1995.488968.
- [54] Yuhui Shi and Russell C. Eberhart. "A modified particle swarm optimizer". In: *1998 IEEE International Conference on Evolutionary Computation Proceedings. IEEE World Congress on Computational Intelligence (Cat. No.98TH8360)*. IEEE, 1998, pp. 69–73. ISBN: 0-7803-4869-9. DOI: 10.1109/ICEC.1998.699146.
- [55] James Kennedy. "The particle swarm: social adaptation of knowledge". In: *Proceedings of 1997 IEEE International Conference on Evolutionary Computation (ICEC '97)*. IEEE, 1997, pp. 303–308. ISBN: 0-7803-3949-5. DOI: 10.1109/ICEC.1997.592326.
- [56] Russell C. Eberhart and Yuhui Shi. "Comparing inertia weights and constriction factors in particle swarm optimization". In: *Proceedings of the 2000 Congress on Evolutionary Computation. CEC00 (Cat. No.00TH8512)*. Vol. 1. 2. IEEE, May 2000, pp. 84–88. ISBN: 0-7803-6375-2. DOI: 10.1109/CEC.2000.870279.
- [57] Maurice Clerc and James Kennedy. "The particle swarm - explosion, stability, and convergence in a multidimensional complex space". In: *IEEE Transactions on Evolutionary Computation* 6.1 (2002), pp. 58–73. ISSN: 1089778X. DOI: 10.1109/4235.985692.
- [58] Nikhil Padhye, Kalyanmoy Deb, and Pulkit Mittal. "Boundary Handling Approaches in Particle Swarm Optimization". In: *Advances in Intelligent Systems and Computing*. Vol. 201 AISC. VOL. 1. 2013, pp. 287–298. ISBN: 9788132210375. DOI: 10.1007/978-81-322-1038-2_25.
- [59] Natan Andrei and Henrik Johannesson. "Higher dimensional representations of the $SU(N)$ Heisenberg model". In: *Physics Letters A* 104.6-7 (Sept. 1984). Ed. by Intergovernmental Panel on Climate Change, pp. 370–374. ISSN: 03759601. DOI: 10.1016/0375-9601(84)90819-3.

Bibliography

- [60] Henrik Johannesson. “The structure of low-lying excitations in a new integrable quantum chain model”. In: *Nuclear Physics B* 270.C (Jan. 1986), pp. 235–272. ISSN: 05503213. DOI: 10.1016/0550-3213(86)90554-7.
- [61] Philippe Corboz et al. “Spontaneous trimerization in a bilinear-biquadratic $S=1$ zigzag chain”. In: *Physical Review B* 76.22 (Dec. 2007), p. 220404. ISSN: 1098-0121. DOI: 10.1103/PhysRevB.76.220404.
- [62] Max Führinger. “Spinon confinement and the Haldane gap in $SU(n)$ spin chains”. PhD thesis. Universität Karlsruhe, 2008.
- [63] Stephan Rachel et al. “Spinon confinement and the Haldane gap in $SU(n)$ spin chains”. In: *Physical Review B* 80.18 (Apr. 2009), p. 4. ISSN: 10980121. DOI: 10.1103/PhysRevB.80.180420.
- [64] H. Nonne et al. “Competing orders in one-dimensional half-filled multicomponent fermionic cold atoms: The Haldane-charge conjecture”. In: *Physical Review B* 84.12 (Sept. 2011), p. 125123. ISSN: 1098-0121. DOI: 10.1103/PhysRevB.84.125123.
- [65] H. Nonne et al. “Symmetry-protected topological phases of alkaline-earth cold fermionic atoms in one dimension”. In: *EPL (Europhysics Letters)* 102.3 (May 2013), p. 37008. ISSN: 0295-5075. DOI: 10.1209/0295-5075/102/37008.
- [66] Takahiro Morimoto et al. “ Z_3 symmetry-protected topological phases in the $SU(3)$ AKLT model”. In: *Physical Review B* 90.23 (Dec. 2014), p. 235111. ISSN: 1098-0121. DOI: 10.1103/PhysRevB.90.235111.
- [67] Kasper Duivenvoorden and Thomas Quella. “Discriminating string order parameter for topological phases of gapped $SU(N)$ spin chains”. In: *Physical Review B* 86.23 (Dec. 2012), p. 235142. ISSN: 1098-0121. DOI: 10.1103/PhysRevB.86.235142.
- [68] V. G. Knizhnik and A. B. Zamolodchikov. “Current algebra and Wess-Zumino model in two dimensions”. In: *Nuclear Physics B* 247.1 (1984), pp. 83–103. ISSN: 05503213. DOI: 10.1016/0550-3213(84)90374-2.
- [69] Seiji Yunoki and Sandro Sorella. “Two spin liquid phases in the spatially anisotropic triangular Heisenberg model”. In: *Physical Review B* 74.1 (July 2006), p. 014408. ISSN: 1098-0121. DOI: 10.1103/PhysRevB.74.014408.
- [70] Ian Affleck et al. “ $SU(2n)$ quantum antiferromagnets with exact C-breaking ground states”. In: *Nuclear Physics B* 366.3 (1991), pp. 467–506. ISSN: 05503213. DOI: 10.1016/0550-3213(91)90027-U.
- [71] Sylvain Capponi. These conclusions agree with unpublished DMRG results (private communication).
- [72] Ian Affleck and Elliott H. Lieb. “A proof of part of Haldane’s conjecture on spin chains”. In: *Letters in Mathematical Physics* 12.1 (1986), pp. 57–69. ISSN: 03779017. DOI: 10.1007/BF00400304.

-
- [73] Ian Affleck. “Spin gap and symmetry breaking in CuO₂ layers and other antiferromagnets”. In: *Physical Review B* 37.10 (1988), pp. 5186–5192. ISSN: 01631829. DOI: 10.1103/PhysRevB.37.5186.
- [74] Tao Li and Fan Yang. “Variational study of the neutron resonance mode in the cuprate superconductors”. In: *Physical Review B* 81.21 (June 2010), p. 214509. ISSN: 1098-0121. DOI: 10.1103/PhysRevB.81.214509.
- [75] Jia-Wei Mei and Xiao-Gang Wen. “Design local spin models for Gutzwiller-projected parton wave functions”. In: (July 2014), p. 9.
- [76] X. G. Wen, Frank Wilczek, and A. Zee. “Chiral spin states and superconductivity”. In: *Physical Review B* 39.16 (June 1989), pp. 11413–11423. ISSN: 0163-1829. DOI: 10.1103/PhysRevB.39.11413.
- [77] Philippe Corboz et al. “Simplex solids in SU(N) Heisenberg models on the kagome and checkerboard lattices”. In: *Physical Review B* 86.4 (July 2012), p. 041106. ISSN: 1098-0121. DOI: 10.1103/PhysRevB.86.041106.
- [78] Mathias van den Bossche, F.-C. Zhang, and Frédéric Mila. “Plaquette ground state in the two-dimensional SU(4) spin-orbital model”. In: *The European Physical Journal B* 17.3 (Oct. 2000), pp. 367–370. ISSN: 1434-6028. DOI: 10.1007/PL00011085.
- [79] G. Szirmai et al. “Gauge fields emerging from time-reversal symmetry breaking for spin-5/2 fermions in a honeycomb lattice”. In: *Physical Review A* 84.1 (July 2011), p. 011611. ISSN: 1050-2947. DOI: 10.1103/PhysRevA.84.011611.
- [80] P. Sinkovicz et al. “Spin liquid phases of alkaline-earth-metal atoms at finite temperature”. In: *Physical Review A* 88.4 (Oct. 2013), p. 043619. ISSN: 1050-2947. DOI: 10.1103/PhysRevA.88.043619.
- [81] Assa Auerbach. *Interacting Electrons and Quantum Magnetism*. Graduate Texts in Contemporary Physics. New York, NY: Springer New York, 1994. ISBN: 978-1-4612-6928-1. DOI: 10.1007/978-1-4612-0869-3.



Jérôme Dufour

PhD in Physics

Birth

23rd November 1987
in Le Locle
(28 years old)

Address

EPFL
Faculté des Sciences de Base
1015 Lausanne
Vaud / Switzerland

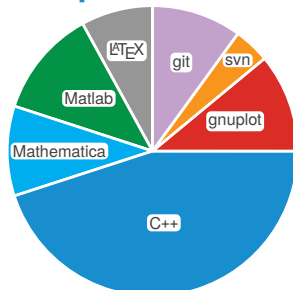
Mail

jerome.dufour@epfl.ch

Languages

French	★★★★★
English	★★★★☆
German	★★★☆☆
Italian	★★☆☆☆

Computer Skills



Linux	★★★★★
IOS	★★★★☆
Windows	★★★☆☆

Education

- | | |
|------|---|
| 2016 | PhD in Physics in the Chair of Condensed Matter Theory EPFL <ul style="list-style-type: none">• <i>Title of the thesis:</i> Variational investigation of the $SU(N)$ Heisenberg model in antisymmetric irreducible representations• <i>Theoretical work:</i> Studied group theory, mean-field solutions and ground state properties of the relevant model on various lattices• <i>Numerical work:</i> Developed a numerical method optimizing the variational energies for multiple parameters (available on: github.com/jduf)• <i>Courses attended:</i> Complex Networks, Bosonization, Frustrated Magnetism, Conformal and Quantum Field Theories, Renormalization Group• <i>Teaching:</i> Supervised students during their master projects and exercise sessions (Statistical Physics, Quantum Physics and Analytical Mechanics) |
| 2012 | Master of Science in Physics EPFL <ul style="list-style-type: none">• <i>Courses attended:</i> Statistical Physics, Quantum Physics, Quantum Field Theory, Relativity and Cosmology, Molecular Quantum Dynamics, Neural Networks and Biological Modelling• <i>Master Project:</i> Study of hard-core bosons on a square lattice via diagrammatic perturbation theory |
| 2010 | Bachelor of Science in Physics EPFL |
| 2007 | Swiss Federal Maturity Collège des Creusets in Sion / VS <ul style="list-style-type: none">• Advanced mathematics, Physics and Applied Mathematics, Bilingual French-German section |

Professional experience

- | | |
|-------------|---|
| 2009 - 2016 | Assistant for various physics classes EPFL <ul style="list-style-type: none">• Provide individualised support to students during their exercise sessions |
| 2003 - 2015 | Karate teacher KC Valais <ul style="list-style-type: none">• Provide two training sessions per week for children from 5 to 18 years old |
| 2010 | Divemaster PADI Sainte-Maxime / France <ul style="list-style-type: none">• Guide and ensure the safety of divers during summer |
| 2008 | Volunteer Research center CRILOBE / French Polynesia <ul style="list-style-type: none">• Help several teams of researchers in their study on the marine ecosystem during one month |
| 2006 - 2008 | Lifeguard Bains de Saillon / Valais <ul style="list-style-type: none">• Ensure the safety of bathers during three summers |